

Studies of Air Shower Observables for the Search for Ultra High Energy Photons

Masterarbeit
zur Erlangung des akademischen Grades
Master of Science
(M.Sc.)

der Universität Siegen



Department Physik

vorgelegt von

Philip Rühl

Juli 2016

Abstract

This thesis concerns the search for photon primaries in the cosmic ray spectrum in the ultra high energy regime above 1 EeV. Due to the very low particle flux at those energies – less than one particle per km² per year – one of the main problems is the lack of statistics. Hence, a maximum amount of information has to be extracted out of each detected event to be able to separate photons from other primary particles. The Pierre Auger Observatory provides a unique possibility for this task thanks to its great exposure to cosmic rays and its hybrid measurement technique which contains the simultaneous use of air fluorescence detectors to monitor the sky and water Cherenkov tanks to measure air shower footprints on the ground. It is the task of data analysis to merge the information from both detector types in the most advantageous way. Therefore, the observables used for the analysis have to be precisely understood and their systematic must be well known before applying them to the actual data. In this thesis, the air shower observables F_γ and S_b are studied in detail with respect to their systematic uncertainties using Monte Carlo simulations of air showers. Their limits of applicability and their robustness against changes in the detector and calibrations are analyzed. In the end, possible cuts are discussed which shall avoid systematical biases to the analysis and an optimum value for a quality cut on F_γ is presented.

Table of Contents

1	Introduction	2
1.1	History of Astroparticle Physics	2
1.2	Cosmic Rays	4
1.3	Extensive Air Showers	7
1.4	The Pierre Auger Observatory	11
1.5	The Surface Detector (SD)	13
1.6	The Fluorescence Detector (FD)	15
1.7	Photons as Primary Particles	19
1.8	Technical Utilities for the Analysis	23
1.8.1	Tools Used for Calculations and Plotting	24
1.8.2	Simulation Samples Used for the Analysis	24
2	Studies of the Observable F_γ	27
2.1	Definition of F_γ	27
2.2	Changes in the F_γ Analysis	33
2.2.1	Including High-Gain Saturated Stations in the LDF Fit	33
2.2.2	Including Non-Triggering Station up to 5000 m from the Core	35
2.2.3	Change in the Energy Calibration of the SD Array	35
2.2.4	Including New Triggers in the LDF Function	39
2.2.5	Event Selection	43
2.3	Robustness Checks	45
2.3.1	Events With Few Triggered Stations	45
2.3.2	Application of the β Parameterization Above 10 EeV	49
2.4	Quality Cut Analysis	52
3	Studies of the Observable S_b	57
3.1	Definition of S_b	57
3.2	Impact of Holes in the SD Array on the Analysis with S_b	59
3.3	Alternative Definition of the S_b -Cut	69

<i>Table of Contents</i>	1
<hr/>	
4 Conclusions	73
4.1 Summary of Results	73
4.2 Prospects	74
5 Appendix	76

1 Introduction

1.1 History of Astroparticle Physics

The oldest form of natural science is the observational one. Closely observing natural phenomena and trying to discover and understand the fundamental laws behind them has always been a major task in the history of mankind. While many phenomena can be artificially created in laboratories for closer investigation, the physical conditions for others can not be reproduced by man. To investigate and understand such phenomena, one has to rely on the information provided by nature. One well known example is the discovery of the true form of the classical gravitational law by Isaac Newton (1684) based on Tycho Brahe's and Johannes Kepler's observations of the movement of extraterrestrial objects around their mutual center of mass. Although people have been watching the night sky ever since the beginning of historiography trying to make sense out of their observations, there are still countless questions related to space which are still unsettled. Reaching from the first recorded observation of a super nova explosion passed on by the Chinese of the 11th century, whose physics is still not entirely understood, to the origin of the, just lately measured, gravitational waves or the question about extraterrestrial life, the variety of open questions covers a wide range of scientific disciplines. Concerning this field of research, a major discovery was made by Victor Franz Hess in the second decade of the 20th century. In the time after the discovery of radioactivity by Henri Becquerel in 1896, the abundance of natural ionizing radiation in the atmosphere was commonly believed to originate solely from radioactive ores in the ground. This concept has even been confirmed by Theodor Wulf (1910) who measured the decreasing density of ionization as a function of altitude on top of the Eiffel Tower. When the year after, Hess extended those measurements to even higher altitudes using hydrogen filled balloons (see Fig. 1(a)), he realized that the decreasing intensity of ionizing radiation started to increase again at higher altitude (see Fig. 1(b)). As a consequence he concluded that, in addition to the terrestrial component of ionizing radiation, there must be an extraterrestrial component, too. This component, which was later on confirmed by Werner Kohlhörster, was named "cosmic rays" due to its origin. Further measurements in the following 20 years during the night and also during a partial solar eclipse implied, that the sun was not the main source of the cosmic rays. While in the beginning those rays were believed to be photons from outer space, the lateral dependence of the cosmic ray flux indicated a large component of charged particles [BV08]. The awareness that there was a constant presence of radiation reaching the

earth from outer space gave rise to a completely new chapter of physics, namely astroparticle physics [GC05].

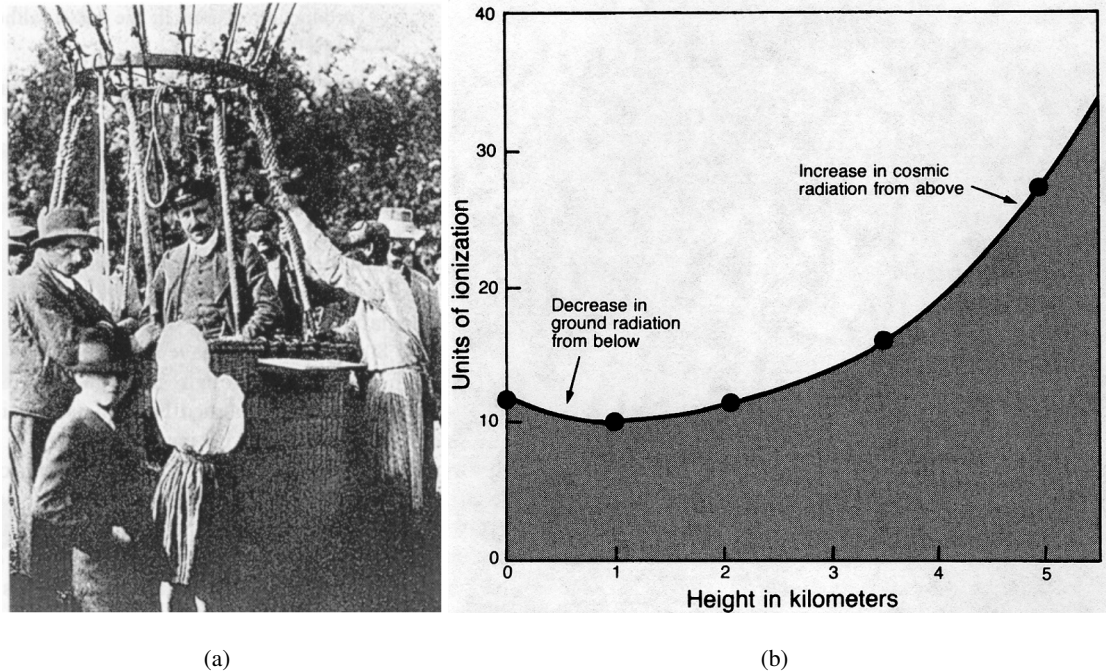


Figure 1.1.1: (a) Victor Hess shortly after landing from one of his balloon ascents in 1912; (b) the ionization density of the atmosphere as a function of altitude as measured by Hess during his balloon ascents 1911–1914 (Pictures adapted from [KJ80]).

In 1938, Pierre Victor Auger and his group proved, that the particles measured in the atmosphere do not directly originate from space, but are produced at high altitudes in collisions of the primary cosmic rays with the atmospheric constituents. He achieved this by measuring coincident signals separated by open ground and found that bunches of numerous particles arrived at almost the same time. This was only possible if there was a causal connection between them, that is, a common production point in space-time [BV08]. The fact, that a large number of secondary particles on the ground had a common origin, a single extraterrestrial particle, led to the conclusion, that the most energetic cosmic rays are many orders of magnitude more energetic as previously assumed. Since those secondary particles could not be produced in laboratories at that time, the studies of cosmic rays lead to various new discoveries in the field of nuclear and elementary particle physics with beginning of the 1930s. The first major discoveries were the observation of the positron in a cloud chamber in 1932 by Carl Anderson and the neutron in the same year by James Chadwick, which were the first particles to be discovered besides the

photon, the electron and the proton. In the following decades the spectrum of known particles increased rapidly with the discoveries of the muon (1937), which seemed to be a heavier version of the electron, the light charged mesons π^+ and π^- (1947) which were identified as the Yukawa-particles, Yukawa used to explain the stability of the atomic nucleus, the tau (1975) as the first member of the third lepton family, the charged and neutral kaons as well as a variety of other mesons and baryons which were to follow. The integration of all those particles within a small set of fundamental particles and their interactions, today known as the standard model of particle physics, is probably the greatest achievement in elementary particle theory in the 20th century. With the technological progress, physicists were able to build accelerators and reproduce the effects observed from the cosmic radiation starting in the 1950s. This development changed the goals of astroparticle physics researches slightly away from particle physics and more towards cosmological questions like the sources, acceleration mechanisms and the elementary composition of cosmic rays.

1.2 Cosmic Rays

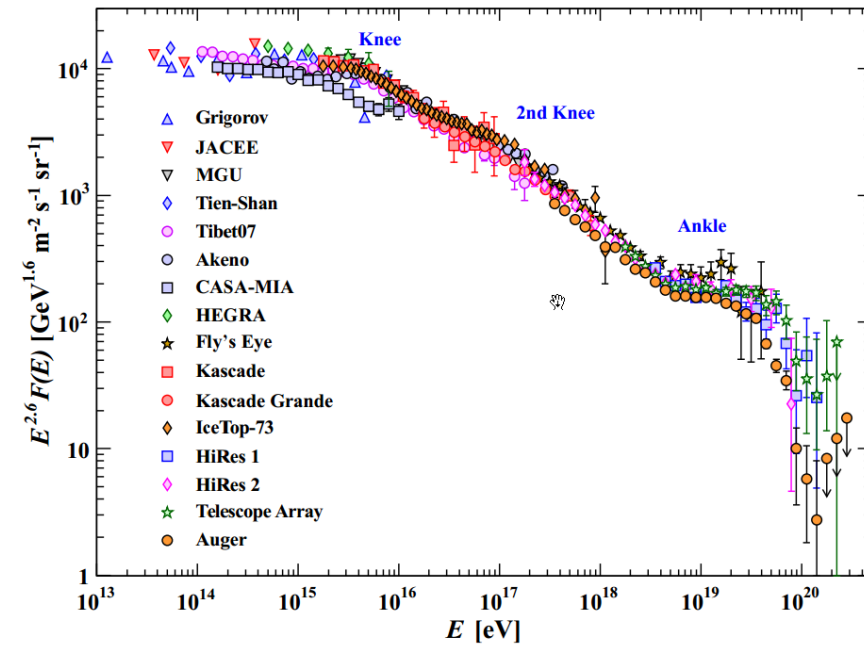
The first measured cosmic rays were charged particles like electrons, protons and heavier atomic nuclei. Thus, the term “cosmic rays” historically refers only to the charged component of the cosmic particle flux. But there are many other, uncharged particles which hit the earth continuously like photons and neutrinos. The neutrino flux from the sun which penetrates the earth is in the order of 10^{11} particles/(cm² s) in the energy range from ~ 100 keV to ~ 20 MeV. Of those, on average only two interact with matter on their way through the earth [GC05].

The flux of the charged cosmic rays at those energies is strongly suppressed by the geomagnetic field and the solar wind. A charged particle below the GeV range is typically deflected by the magnetic field before it can reach the atmosphere [PD03]. The spectrum of cosmic rays starting from 10 TeV is shown in Fig. 1.2.1. Considering the ordinate being multiplied by $E^{2.6}$, one can see that the spectrum follows a power law which changes its spectral index three times before it reaches a cutoff at around 500 EeV. The first change in the steepness is referred to as the “knee” at about 3 PeV. At this point the spectral index changes from -2.7 to -3.0 . At the “2nd knee” at around 300 PeV the slope changes again from -3.0 to -3.2 . The knee and the 2nd knee are believed to be caused by the acceleration mechanisms within our galaxy which at some point are not able to produce any higher energies. The fast propagating shock fronts

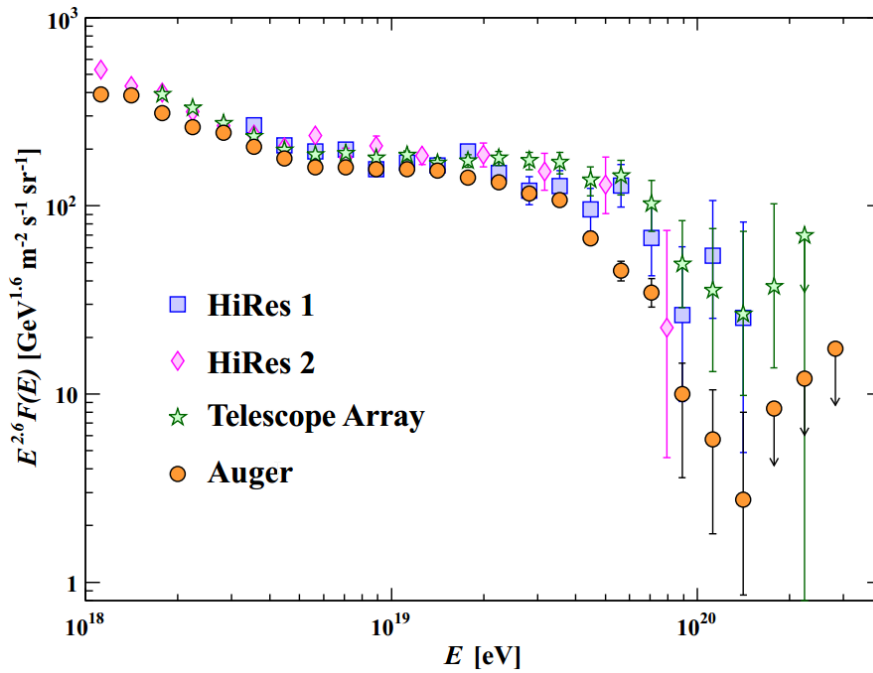
of supernova remnants (SNR) are favored candidates for sources due to first and second order Fermi acceleration. Other possible candidates for sources are the rapidly changing high magnetic fields in the vicinity of neutron stars and the galactic center of the milky way. However, it is not completely clear what the sources are and many theories claim new physics like Supersymmetry or Technicolor [KD01] as the origin of the those features in the energy spectrum. Above the “ankle” at around 3 EeV, where the spectral index increases again from -3.2 to -2.7 , the origin of the ultra high energy cosmic rays (UHECR) – cosmic rays above 1 EeV – is assumed to be extragalactic [BJ12, MK08]. It is still unclear which violent conditions in the universe can accelerate particles to such enormous energies. The lately observed merger of two massive black holes GW150914 by the LIGO collaboration is one example for a currently discussed candidate for the production of UHECR [KK16]. At the top end of the spectrum at around 50 EeV the flux seems to be strongly suppressed as indicated by data. If the origin of those UHECR lies not within our own galaxy, a cutoff at this energy is predicted by the Greisen-Zatsepin-Kuz’min (GZK) effect. The GZK effect describes the scattering of cosmic ray protons with photons from the cosmic microwave background (CMB) via a Delta resonance like

$$p + \gamma_{CMB} \rightarrow \Delta(1232)^+ \rightarrow \begin{cases} p + \pi^0 \\ n + \pi^+ \end{cases}, \quad (1.1)$$

while the pions again decay into photons and leptons. The initial energy of the proton is then usually distributed among the products more symmetrically which leaves them with lower energy on average. The mean free path due to this process for energies above 50 EeV is 6 Mpc [RR15]. This means that particles above this energy have to originate from within our own or at least a very close neighboring galaxy. Otherwise they would not be able to reach the earth. For heavier nuclei, the GZK threshold is higher than for protons, but for them, the process of photo-disintegration with the CMB and the extragalactic background light reduces the flux significantly. Considering these circumstances it is all the more extraordinary, that particles have been measured with energies up to some 100 EeV. The most energetic particle has been measured by the High Resolution Fly’s Eye Cosmic Ray Detector in October, 1991 in Utah with an energy of $(3.0 \pm_{0.54}^{0.36}) \times 10^{20}$ eV [HF94], named the “Fly’s Eye particle”. A detailed analysis about the particle type of the Fly’s Eye particle can be found in [RM04].



(a)



(b)

Figure 1.2.1: (a) The energy spectrum of cosmic rays. The ordinate is multiplied by $E^{2.6}$ to make the changes of the spectral index, known as the “knee”, the “2nd knee” and the “ankle” more visible. The cutoff of the spectrum which can be seen around 50 EeV is in agreement with the GZK predictions. The data shown here is compiled from various experiments which seem to agree quite well on the overall shape of the spectrum. In (b) the spectrum is zoomed into the ultra high energy (UHE) region. The cutoff is observed by all three experiments shown here. (Picture adapted from [BJ12]).

1.3 Extensive Air Showers

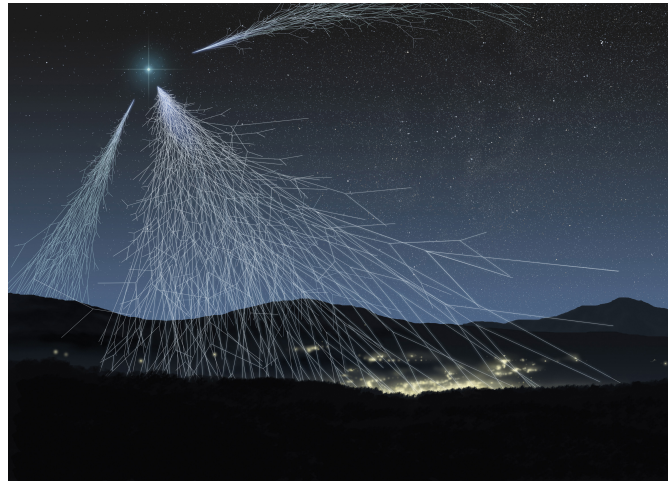


Figure 1.3.1: Artistic view of Extensive Air Showers (EAS). [Credit: ASPERA/Novapix/L.Bret]

When a high energetic cosmic ray particle reaches the earth's atmosphere it will eventually interact with the atmospheric constituents, i.e. mainly N_2 , O_2 and Ar. By deep inelastic scattering with those nuclei, multiple secondary particles may be produced. If the energy of the primary is very high ($E \gtrsim 10 \text{ TeV}$), the secondary particles carry again enough energy to undergo inelastic scattering and so on. By this mechanism, a large number of secondaries is produced in subsequent collisions. Since each particle at the final state of a scattering process has a certain chance of carrying away a statistically distributed amount of transverse momentum, the particle cascade is not focused on its axis – the direction of motion of the primary – but starts to spread out while diving deeper into the atmosphere. Since all particles are approaching earth at approximately the speed of light, the particle cascades forms a flat disc during its propagation which can reach a diameter up to several kilometers. Referring to their size, those cascades are called extensive air showers (EAS).

Such an air shower can basically be divided into a hadronic (hard) component, an electromagnetic (soft) component, made up of electrons and photons and a myonic component. Photons are typically produced in the decay of neutral pions out of the hadronic component while electrons can be produced from pairproduction or the decay of myons which themselves are products of the decays of charged pions. As consequences of the shower constituents interacting with the atmosphere, also fluorescence light and air Cherenkov radiation can be observed from an air shower.

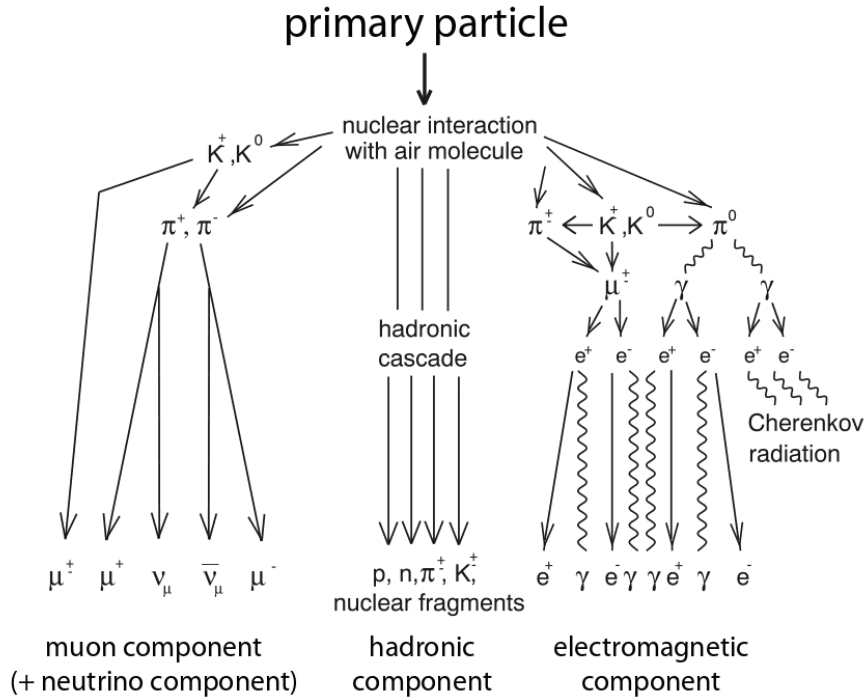


Figure 1.3.2: Schematic visualization of an air shower in the atmosphere. The air shower is commonly divided into its hadronic, electromagnetic and muonic component. (Picture adapted from [KB04]).

With more and more subsequent collisions, the single particles lose constantly energy until the cross section for atmospheric absorption exceeds the one for scattering processes. When this limit is reached, the shower starts to die out. The slant depth, where the shower is at its maximum size (size measured by the number of particles N contained in the shower), is called X_{max} . The average longitudinal profile of an air shower can be seen in Fig. 1.3.3 and can be described by a Gaisser-Hillas function [GT77]:

$$N(X) = N_{max} \left(\frac{X - X_0}{X_{max} - X_0} \right)^{\frac{X_{max} - X_0}{\lambda}} \exp\left(\frac{X_{max} - X}{\lambda} \right), \quad (1.2)$$

which parameterizes the shower size as a function of atmospheric depth X , where N_{max} is the maximum size of the shower reached at X_{max} and X_0 and λ are parameters which depend on the primary mass and energy.

Although the shower front covers a large area, most of its energy is contained in the region close to the axis. About this axis, the lateral distribution is to a large extent symmetric on average. A small perturbation of this symmetry is caused by the deflection of low energy particles by the geomagnetic field. This azimuthal asymmetry is mostly emphasized in very inclined

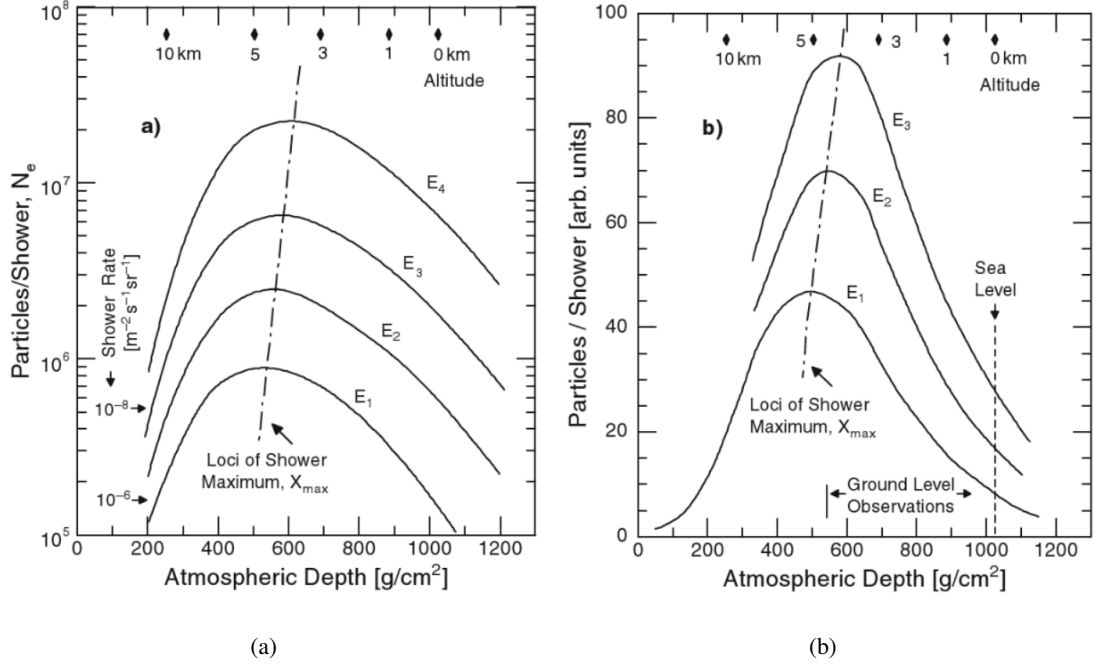


Figure 1.3.3: The Gaisser-Hillas function to describe the longitudinal development of an air shower in (a) logarithmic and (b) linear scale. Considering $E_1 < E_2 < E_3 < E_4$, one can see, that the depth of the shower maximum, X_{max} , increases with increasing primary energy. (Picture adapted from [GP10]).

showers, where the angle between momentum direction and geomagnetic field varies the most within 2π azimuth. Assuming an approximately symmetric density for vertical showers, the electron density as function of perpendicular distance r from the axis of such a shower follows a functional form of the Nishimura Kamata Greisen (NKG) type [KK58]:

$$\rho_e(r) = \frac{N_e}{2\pi r_M^2} \frac{\Gamma(4.5 - s)}{\Gamma(s)\Gamma(4.5 - 2s)} \left(\frac{r}{r_M}\right)^{s-2} \left(1 + \frac{r}{r_M}\right)^{s-4.5} \quad (1.3)$$

where N_e is the number of electrons in the shower at a specific instant, r_M is the Molière Radius [GC96] and $s = 3\left(1 + 2\frac{X_{max}}{X}\right)^{-1}$ [UM08] is a parameter called the "shower age" which parameterizes the lifetime of the shower like $s = 0$ at the time of the first interaction of the primary particle and $s = 1$ when the shower reaches its maximum ($X = X_{max}$). Γ is the Gamma function which satisfies the relation $\Gamma(x + 1) = (x)\Gamma(x)$.

The electromagnetic component of an air shower is mainly determined by Coulomb scattering, pair production and bremsstrahlung. The more complicated hadronic interactions lead to a flatter lateral distribution of the hadronic component making the shower front more spread out compared to the electromagnetic shower. Moreover, the lateral shape of a shower front is sensitive to

the type of the primary particle. A primary proton for example would induce a shower with a far steeper lateral distribution than a heavier nucleus would do due to the larger hadronic component of the subsequent shower. In contrast, primary photons induce almost purely electromagnetic showers which have even steeper lateral profiles than proton showers. These characteristics offer a possibility to distinguish between primary particle types by measuring the lateral profile of a shower on the ground. The lateral shape of an air shower is commonly described by using a lateral distribution function (LDF) in the form of a modified NKG function:

$$f_{LDF}(r) = \left(\frac{r}{1000 \text{ m}}\right)^\beta \left(\frac{r + 700 \text{ m}}{1700 \text{ m}}\right)^\gamma. \quad (1.4)$$

Here, r denotes the distance from the shower axis and β and γ are free parameters which determine the shape of the LDF and depend on the properties of the primary particle. The expected signal $S(r)$ which can be measured on ground is proportional to the particle density at a certain distance r from the axis and can be obtained from the LDF like

$$S(r) = S_{1000} \times f_{LDF}. \quad (1.5)$$

Where S_{1000} is the average signal expected at a distance of 1000 m from the axis.

Besides the steepness of the lateral shower profile, another characteristic observable which is sensitive to the primary mass is the value of X_{max} . Considering the extremely high energies of the primary particles, the constituents of heavy nuclei can be considered to behave like almost independent particles in the center of mass frame of the collision due to asymptotic freedom. Therefore, a heavy nucleus with a mass number A and a certain energy E induces an air shower which can approximately be described by A superimposed proton showers with a total energy of E . While X_{max} increases with primary energy, a nucleus with higher mass has on average a lower value of X_{max} . Photon showers develop even deeper in the atmosphere than proton showers and have typical X_{max} values which are much higher than the average X_{max} of proton showers (see Fig. 1.3.4). Nevertheless, identification of the primary type by observing its air shower is not that easy since both, the lateral and the longitudinal shape of a shower strongly depend on the depth and the momentum distribution of the first interactions in the atmosphere. Those can heavily fluctuate since the atmosphere is very thin in the region where the first interactions take place. Therefore, only statistical statements about the composition of primary UHECRs can be made based on many air shower events.

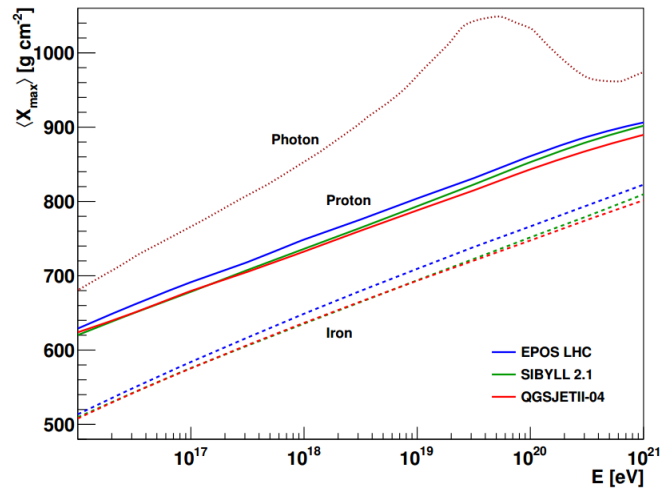


Figure 1.3.4: The theoretical prediction of the average X_{max} for proton, iron and photon showers. The increase of the slope of the curve (elongation rate) for photon showers at $\sim 10^{19}$ eV is caused by the LPM effect. The decrease at $\sim 10^{19.5}$ eV is an effect of photon preshowering. Those effects are described in Sec. 1.7. For the calculations, the three different hadronic interaction models EPOS LHC, SIBYLL 2.1 and QGSJETII-04 have been used independently. Since the primary photons induce almost purely electromagnetic showers, they are barely influenced by a change of the interaction model. (Picture adapted from [SM13]).

1.4 The Pierre Auger Observatory

The Pierre Auger Observatory is currently the worlds largest experiment in the field of astroparticle physics and measures extensive air showers. It is located near the town Malargue in Argentina in the Pampa Amarilla on an elevated plane at 1400 m asl. east to the Andes. The observatory consists of 1660 water Cherenkov tanks distributed over an area of about 3000 km², referred to as the surface detector (SD) and 27 fluorescence telescopes, the fluorescence detector (FD). Additionally, there are the Auger Engineering Radio Array (AERA) to measure the radio emissions from EAS the Auger Myons and Infill for the Ground Array (AMIGA) to measure the myonic shower component. Also installed are different laser facilities, balloon launching stations and cloud cameras to keep track of the weather conditions and the aerosol density in the atmosphere. The FD telescopes are located at four positions on the border of the SD array observing the sky above the plane. The benefit of the concept using completely different measuring techniques is on the one hand an independent crosscheck of the data taken by the detector. On the other hand, a considerable amount of additional information from each air shower event can be extracted by those complementary detectors. Each detector type can measure properties of an

air shower which can not or at least only very hard be extracted from the data measured by the other one. While in principle the SD as well as the FD can be run as standalone detectors, the merger of both provides the possibility of "hybrid measurements" where a shower is simultaneously observed by the SD and the FD. Those events utilize the full potential of the Pierre Auger Observatory and are commonly especially well measured. The subset of events which can be fully reconstructed by both SD and FD is called "golden hybrids". Since the initial energy as well as the arrival direction of such events is measured by both detectors, those events are used to calibrate the detectors against each other. In the following sections, the operating modes of the SD (Sec. 1.5) and the FD (Sec. 1.6) shall be illustrated in more detail.

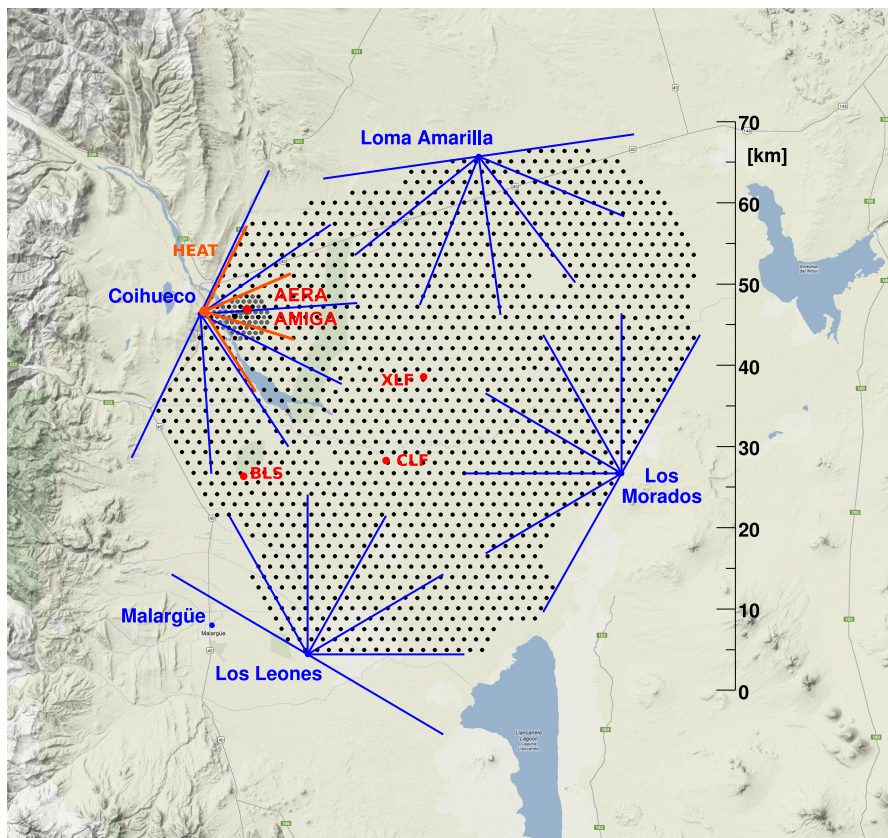


Figure 1.4.1: A Google Earth picture of the Pierre Auger Observatory. The dots mark the positions of the SD stations. The viewing angle of each telescope at the four FD sites is shown by the blue lines radiating from the stations. Also shown are the positions of the High Elevation Auger Telescopes (HEAT) (red lines), the Auger Engineering Radio Array (AERA) and the Auger Muons and Infill for the Ground Array (AMIGA) as well as Central Laser Facility (CLF), the eXtreme Laser Facility (XLF), and the Balloon Launch Station (BLS). [Credit: D. Veberič]

1.5 The Surface Detector (SD)

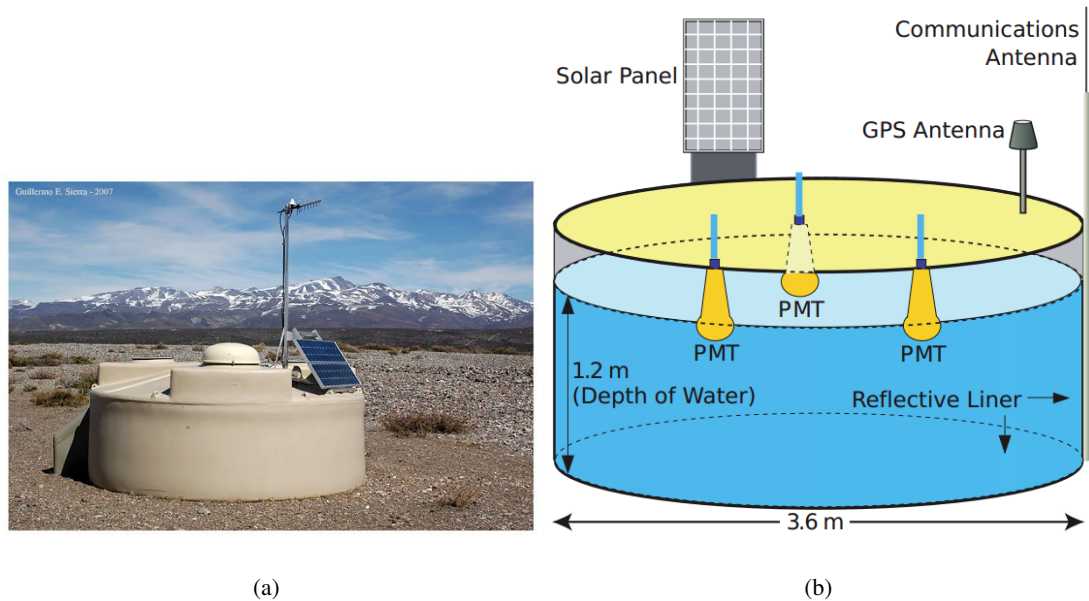


Figure 1.5.1: (a) A picture of an SD station of the Pierre Auger Observatory in the Pampa Amarilla [Credit:Guillermo Sierra 2007]. (b) A schematic view of the installation of an SD station. (Picture adapted from [KB04]).

The 1660 stations which build the SD are arranged in a hexagonal pattern with a spacing of 1500 m, where the average displacement of a single station is in the order of just a few meters. In Fig. 1.5.1 a picture of an SD station as well as a schematic sketch of its structure can be seen. Each station works as an independent particle detector and is completely autonomous. This is achieved by equipping each station with its own battery and electronics package. The electronics are powered by a solar power system on top of each station which provides an average of 10 W. The stations contain a water tank with a diameter of 3.6 m containing 12000 litres of pure water [AI08]. The water serves as a medium for the water Cherenkov effect that occurs, when charged particles travel beyond the speed of light in the respective medium. The inner surface of the water tanks is built to reflect Cherenkov light. This light can be detected by three photomultiplier tubes (PMTs) which are integrated in the top of the tank looking downwards. The PMTs have to cover a wide range of signal since the number of particles in the tank can reach from a total of many 1000 close to the center of the shower down to single particles at larger distances [AJ10a]. To accomplish this, each PMT is connected to a local data acquisition system by a high-gain channel (HG) which is connected to the anode of the PMT and transmits the full amplification and a low-gain channel (LG), which is connected to the dynode and thus provides

a less amplified version of the signal [SH01]. The amplifications of the HG and the LG differ by a nominal factor of 32. The measured signal is by default reconstructed from the HG. When the signal is high enough to saturate the HG, it cannot directly be recovered from there. Therefore the LG provides a less amplified measurement of the signal which makes it possible to recover it from the LG instead in such cases. After an analog signal has been amplified by a PMT, it is digitized with a flash analog-to-digital converter (FADC) which divides the signal into 120 time bins corresponding to a total time window of $3\ \mu\text{s}$. When a signal is coincidentally recorded by all three PMTs, it undergoes the first two steps of the SD trigger logic, the T1 and T2 trigger, which test the signal for certain thresholds in the intensity and time structure as is shown in Fig. 1.5.2. To pass the T1 trigger level for instance, the FADC signal traces of all three PMTs have to exceed either a certain threshold in at least one bin (TH-T1) or a lower threshold over a time period of 13 bins corresponding to 325 ns. The latter is called a time-over-threshold (ToT) trigger. The T1 is an event preselection for the T2 level, which tests the signal for stricter thresholds e.g. in Fig. 1.5.2. After passing both, the T1 and T2 triggers, the signal information from the three PMTs is sent via a wireless transmitter to the central data acquisition system (CDAS) [AJ10a] which makes further checks for coincident signals at SD stations and in a later step also tests against recorded data from the FD in the corresponding time window. A schematic plot of the trigger logic is shown in Fig. 1.5.2. The details can be looked up in [AJ10a].

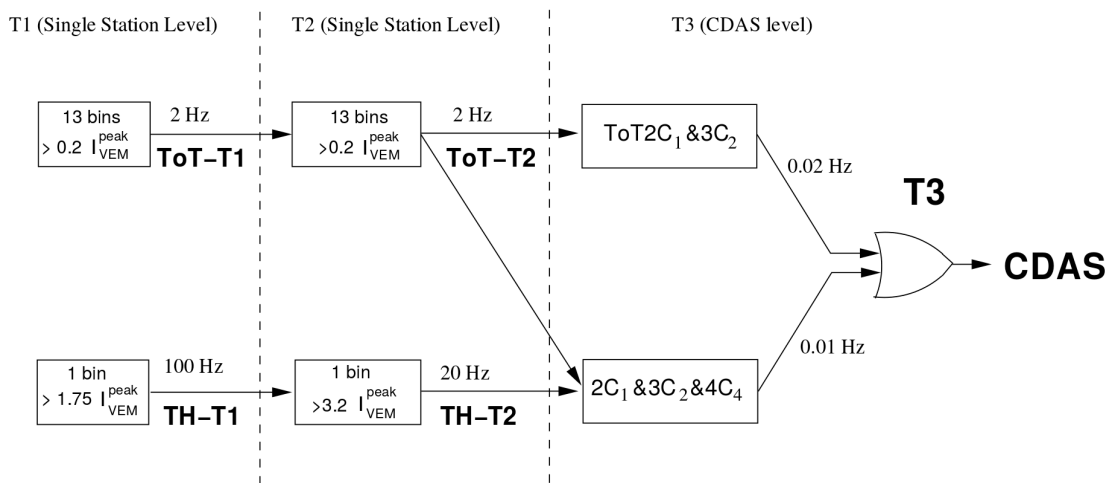


Figure 1.5.2: The different trigger levels of the surface detector. A recorded event has to pass each trigger level subsequently before being processed further by the CDAS. (picture adapted from [AJ10a]).

The signal measured by an SD station is proportional to the energy, which a particle deposits

inside the water while passing through. To express the signal in terms of numbers, the signal is usually normalized to the amount of signal measured from an average muon which passes the tank vertically. This amount of signal is referred to as 1 VEM (vertical equivalent muon). Every signal recorded by the SD is quantified in units of VEM. Since the signal is proportional to the number of particles in the tank and therefore to the particle density of an air shower event, the SD can be used to measure the LDF of an air shower in the SD plane. The duty cycle of data taking for the SD is almost 100% because the measurement is not influenced by weather or differences between day and night [AI08]. Since the location of the Pierre Auger Observatory never experiences long periods with temperatures below zero, there is also no problem with freezing water in the tank. When single components of a station fail, the outage is detected and stored in a database to be considered in later data analysis. Such stations are commonly referred to as "black stations".

1.6 The Fluorescence Detector (FD)



Figure 1.6.1: A photograph of the FD site Los Morados on the east side of the Pierre Auger Observatory. [*Credit: Steven Saffi*]

The FD consists of 27 air fluorescence telescopes monitoring the sky above the SD array. 24 telescopes are located in groups of six at the stations Los Leones, Loma Amarilla, Los Morados and Coihueco (see Fig. 1.4.1). Three additional telescopes build the High Elevation Auger Telescopes (HEAT) near Coihueco (for more information about the HEAT see [MH11]). The FD is used to measure the nitrogen fluorescence emission and the air Cherenkov radiation in the

UV range ($\sim 300 - 430$ nm) (Fig. 1.6.2) induced by extensive air showers [AJ10b].

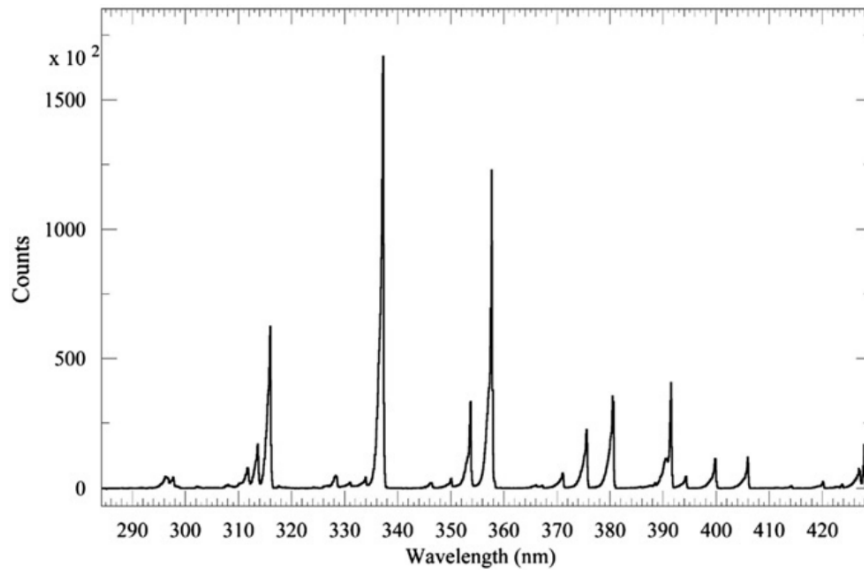


Figure 1.6.2: An example for a measurement of a fluorescence spectrum of an air shower in dry air at a temperature of 293 K and an atmospheric pressure of 800 hPa. (Picture adapted from [AM07]).

When observing an air shower, the rate of fluorescence emission from a certain altitude is proportional to the energy deposit at the corresponding atmospheric depth. Taking into account the influences of air pressure, temperature, humidity and the average particle energy, which depends on the shower age, the fluorescence yield can be used to directly measure the longitudinal shower profile. For example, the average yield from the 337 nm waveband at 293 K and 1013 hPa has been measured by the AIRFLY Collaboration as $5.61 \pm 0.06_{stat} \pm 0.21_{sys}$ photons/MeV (see [AM12]).

Each of the telescopes covers a solid angle of $30^\circ \times 30^\circ$ adding up to a combined azimuth angle of 180° . Their arrangement inside an FD station is shown in Fig. 1.6.3(a). The four FD sites point towards the inside of the Pierre Auger Observatory and have been placed such that a shower above 10 EeV should have a 100% triggering efficiency [AJ10b]. The installation of a single fluorescence telescope is shown in Fig. 1.6.3 (b). The light entering the aperture passes an optical filter which only transmits the UV part. The light is then reflected by a segmented mirror and thrown back onto a camera, build of 440 pixels which are realized as photomultiplier tubes (PMT) installed in the focal plane of the mirror [AJ10b, AM02].

An air shower event is then seen by the telescope as a sequence of triggered pixels. Since every

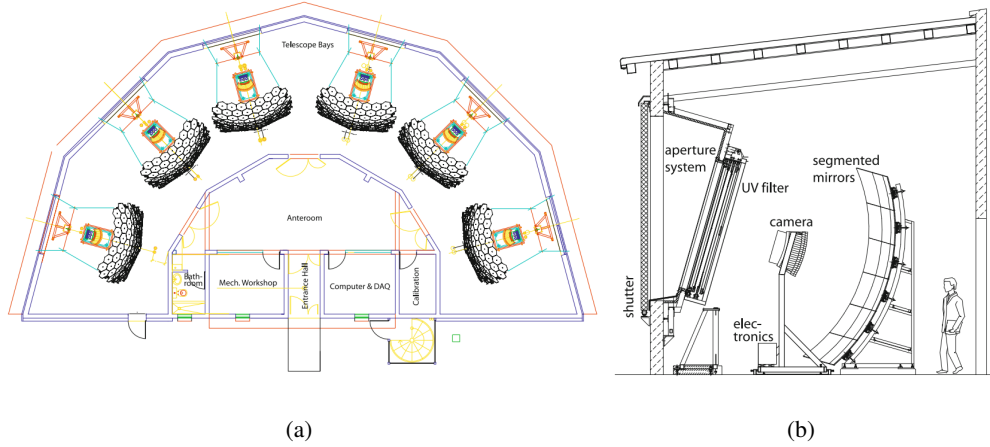


Figure 1.6.3: (a) The arrangement of six fluorescence telescopes within one of the four FD sites. Each one covers a solid angle of $30^\circ \times 30^\circ$. (b) The installation of a fluorescence telescope of the FD of the Pierre Auger Observatory.

100 ns a picture is digitized by the camera, the pixels triggered by an air shower event show a clear time ordering (Fig. 1.6.5). This can be used to reconstruct the shower axis and therefore the arrival direction of the original primary particle. First, the shower detector plane (SDP) – the plane which contains the shower axis and the FD site – is obtained by fitting a straight line to the triggered pixels of the camera. This fixes the position of the axis in two dimensions. To obtain the incidence within this plane, the triggering time of the pixels is used. The expected correlation between viewing angle and arrival time at the detector of the fluorescence light, is given by

$$t_i = t_0 + \frac{R_p}{c_{vac}} \tan\left(\frac{\chi_0 - \chi_i}{2}\right) \quad (1.6)$$

where t_i denotes the arrival time of a photon at pixel i of the camera, t_0 is the time corresponding to the point on the axis which is closest to the detector, in a distance R_p , c_{vac} is the speed of light in the vacuum, χ_0 is the incidence of the shower axis in the SDP and χ_i is the viewing angle of the pixel i within the SDP [KD07]. The reconstruction of the SDP and the determination of the axis is visualized in Fig. 1.6.4. The calorimetric energy of an air shower can also be reconstructed with the FD. This is achieved by deriving the energy deposit of a shower as a function of slant depth using the flux of fluorescence light at the aperture. Then, a Gaisser-Hillas function is fitted to the energy deposit and the calorimetric energy is obtained by integrating over the whole longitudinal profile. Hereby, the attenuation of the fluorescence light in the atmosphere has to be taken into account. Because this attenuation strongly depends on the abundance of aerosols

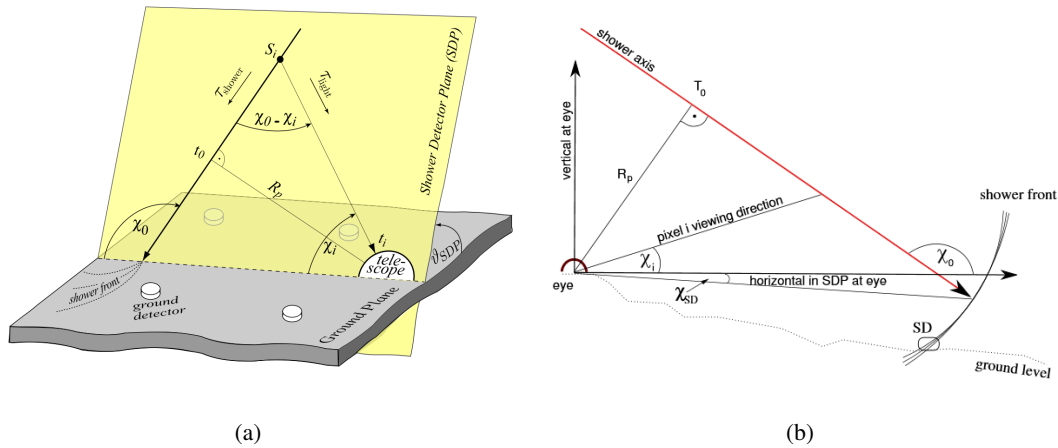


Figure 1.6.4: (a) Visualization of the SPD of an artificial shower axis. The SDP contains the shower axis and the FD telescope by which the shower has been observed and is therefore completely determined. (b) The geometry inside the SPD considered to derive Eq. (1.6). The arrival time information of the fluorescence light at the aperture fixes the remaining free parameter of the shower axis in the SDP. Thus, direction of the shower axis can be reconstructed in three dimensions with the FD. (Picture adapted from [AA15a]).

in the atmosphere, those are constantly measured using the Central Laser Facility (CLF) and the eXtreme Laser Facility (XLF). For detailed information on the reconstruction of an air shower event using the FD see [KD07].

If an event is very high energetic, there is a chance that it can be detected by more than one FD telescope. Those "stereo events" can especially well be reconstructed in terms of energy and arrival direction since the SDP as well as the calorimetric energy can be reconstructed by two sites independently. In the optimal case, both SDPs draw an angle of 90° . Then, both measurements complement each other most advantageous.

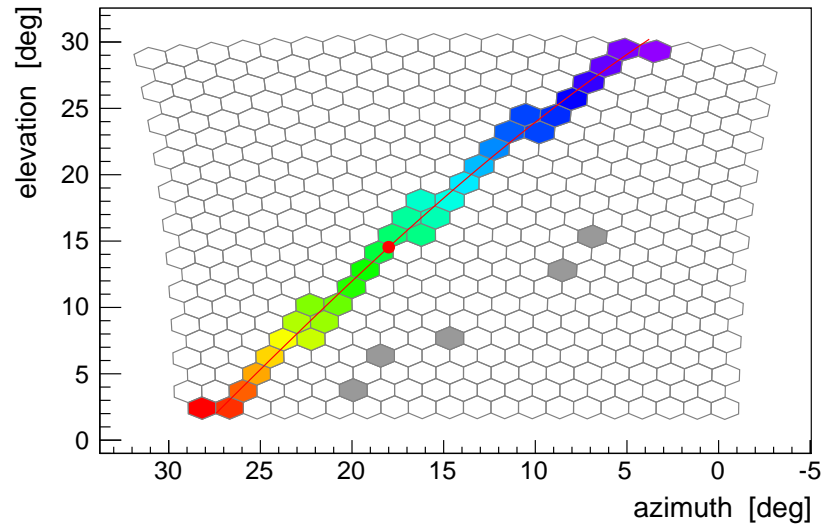


Figure 1.6.5: A trace of triggered pixels at the fluorescence telescope at Los Morados, mirror 2. The time ordering of the pixels goes from blue (early) to red (late). The gray pixels were also triggered but classified as randomly triggered by the background and rejected from the shower reconstruction. (FD Event 3/3508/2232, measured on 1st of July 2016, 01:13:35 at Loma Amarilla)

1.7 Photons as Primary Particles

Photons are one of the most abundant particles in universe. At almost any energy scale one can imagine, there are cosmological objects which can be observed in the respective wavelength, reaching from MHz radio waves emitted from the lobes of radio galaxies and the cosmic microwave background over the full spectrum of infra red (IR), visible and ultra violet light (UV) to X-rays and even gamma rays up to 100 TeV radiated by objects like active galactic nuclei or gamma ray bursts (see Fig. 1.7.2). Many objects can be observed in many different wavelengths simultaneously as shown in Fig. 1.7.1 for the example of the radio galaxy Centaurus A.

The energy spectrum of high energy gamma rays seems to follow approximately a decreasing power law as can be seen in Fig. 1.7.2. Above 100 TeV the cosmic ray flux is far larger than the anticipated photon flux which makes it extremely difficult to identify photons, hence only upper limits on the photon flux could be placed by now.

When looking at cosmic rays at the highest energies, one of the main problems is the lack of statistics due to the low particle flux. At energies above 1 EeV there are only a few particles per km^2 per year. At 10 EeV the flux is more than a hundred times lower and eventually even the Pierre Auger Observatory needs years of data taking to gather a sufficient amount of events

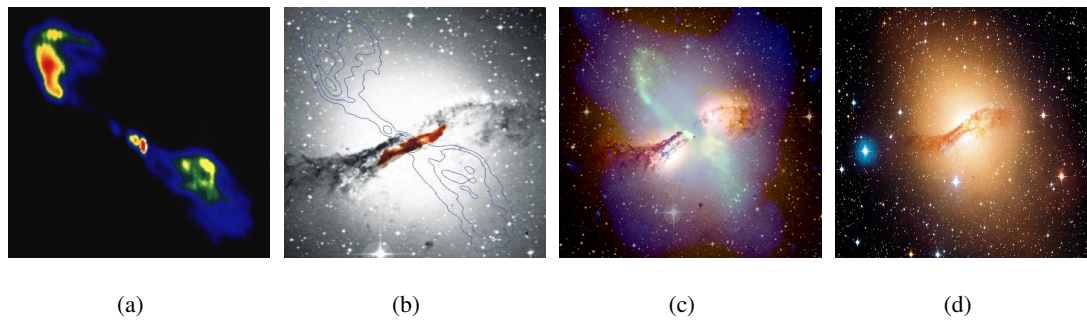


Figure 1.7.1: Centaurus A in the light of (a) radio emission [NRAO], (b) radio and IR [MI98], (c) radio, IR, visible light and X-ray [NASA] and (d) visible light [CJ06].

for statistical data analysis. This lack of statistics is even more substantial when searching for photons in this energy range which, if existing, make up only a tiny fraction of the overall flux. For this reason it is of prime importance to extract a maximum of information from the data collected by the experiment. So far, no statistically significant signal from photons above 1 EeV could be found in the data. The current upper limits on the integral photon flux above this energy were last published on the ICRC 2015 and can be seen in Fig. 1.7.3 together with upper limits from other experiments.

Many theories exist which predict a certain flux of UHE photons. Those theories can basically be divided in to two categories. On the one hand there are the so called "top-down models" or "non-acceleration models". Those models describe the direct production of UHE photons in processes of new physics like the decay of yet unobserved super massive particles which could be produced in the collapse of topological defects (e.g. cosmic strings or magnetic monopoles). Other theories claim such particles to be metastable relics which were produced in the early universe. Many of these top-down models predict a very large fraction of photons in the UHECR flux. Since a high flux of photons can not be found in the data, many models can already be restricted. The other category are the so called "bottom-up models" or "acceleration models". In these models, UHE photons are produced in the interaction of extremely high energy cosmic rays (EHECR) – particles with energies above 100 EeV – with the CMB via the GZK effect. These theories are considered a more conservative approach since in the production process no new physics is required. Nevertheless, it is still unclear which mechanisms can accelerate charged particles to energies beyond 100 EeV and many theories also postulate physics beyond the standart model to explain these initial accelerations. For a detailed review of the top-down

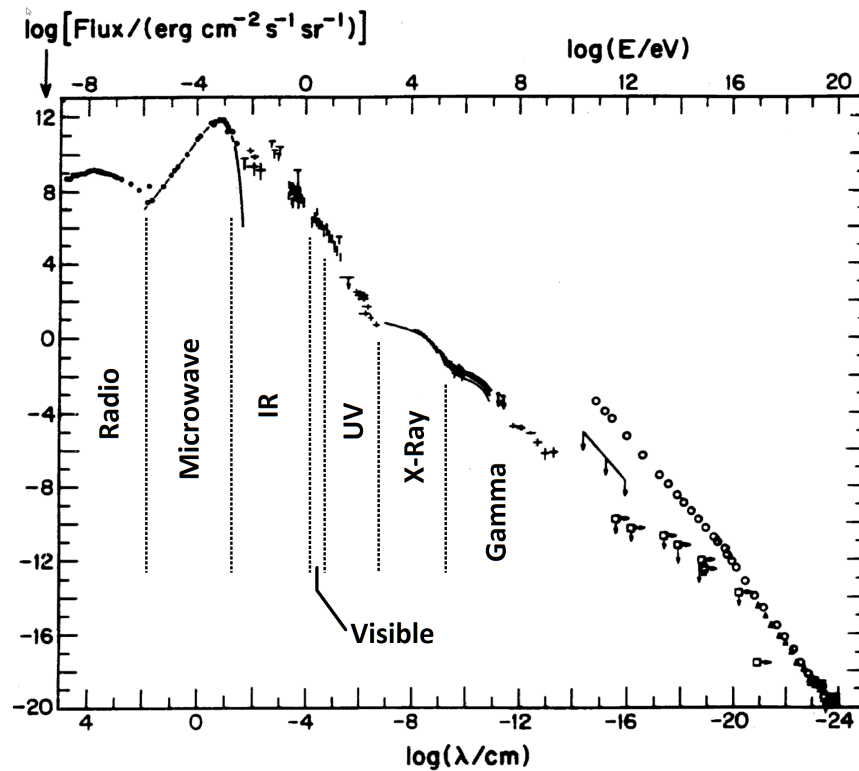


Figure 1.7.2: The flux of extraterrestrial photons observed on earth as function of wavelength covering many orders of magnitude from the MHz radio regime up to high energy gamma rays (black markers). The anticipated upper limits for the photon flux above 10^{-15} cm in comparison to the overall cosmic ray flux (black circles) is also shown. (Picture adapted from [HF98]).

and bottom-up models see [BP00]. The determination of the flux of UHE photons could play a key role in the search for new physics. Since photons carry no electric charge, they are not deflected by magnetic fields and therefore point almost directly back to their sources. This makes them not only messenger particles for the acceleration mechanisms but also for their sources. Depending on the actual flux and arrival direction, many theories about new physics in particle physics as well as in cosmology could be favored or ruled out.

To separate photon events from the hadronic background, an observable or a set of observables is needed which gives a high separation power between photons and hadrons and is applicable on a large number of events to keep the statistics as high as possible. One discriminating observable for this task is the depth of the shower maximum X_{max} . As mentioned earlier, a photon generates an almost purely electromagnetic air shower which develops even deeper in the atmosphere than an average proton shower. In the EeV range, the Landau-Pomeranchuk-

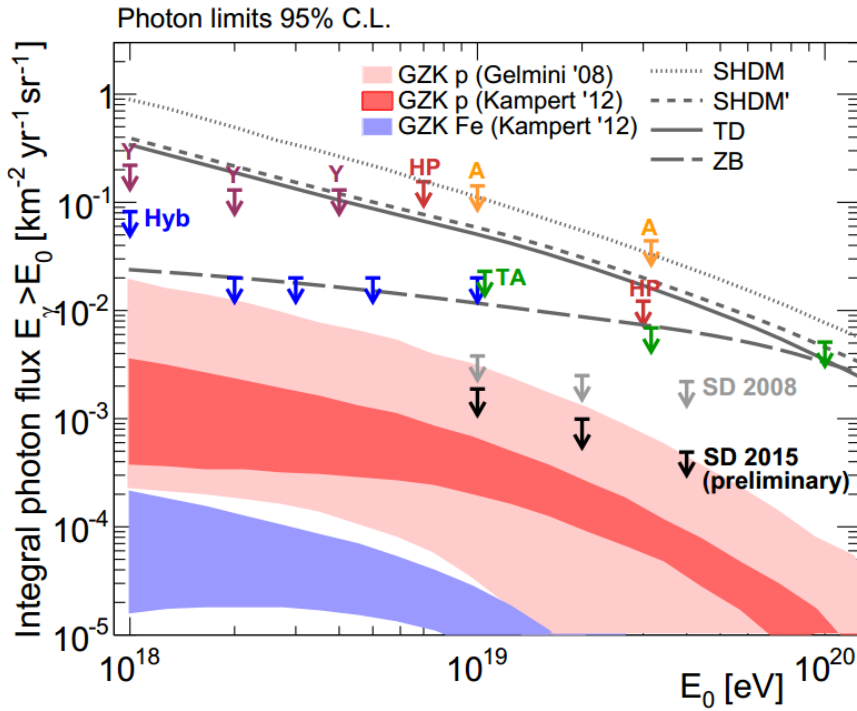


Figure 1.7.3: The current upper limits on the integral photon flux for energies from 1 EeV to 100 EeV from different experiments: the Pierre Auger Observatory with hybrid (Hyb) and SD data, the Telescope Array (TA), Yakutsk (Y), Haverah Park (HP) and AGASA (A). The red and blue regions show the theoretical predictions of the photon flux due to GZK effect. The lines which refer to the flux of UHE photons as predicted by two different models of super heavy dark matter (SHDM), topological defects (TD) and the Z-burst scenario (ZB). (Picture adapted from [BC15]).

Migdal (LPM) effect – the reduction of the cross section between photons and the atmosphere due to coherent scattering with the atmospheric particles – increases the average depth of the first interaction leading to even larger values of X_{max} for photon air showers. At $\sim 10^{19.5}$ eV the preshower effect becomes relevant [RM04]. A preshower is initiated, when a UHE photon interacts with the magnetic field of the earth producing an electron-positron pair. Since the initial photon energy is then divided between the two electrons and subsequent photons produced by bremsstrahlung, the air shower has the shape of a shower induced by many particles with lower energy. The preshower effect works contrarily to the LPM effect and reduces the average X_{max} making photon showers more proton like. The impact of both effects on the average X_{max} of photon showers can be seen in Fig. 1.3.4. Another characteristic of photon showers is the steepness of the LDF. Since photons produce almost pure electromagnetic showers, the particle density

of the showers is strongly confined to the shower axis and the particles have a low transverse momentum compared to hadronic showers. Examples of LDFs for simulated photon and proton showers are displayed in Fig. 1.7.4. The red square marker at a distance of $r = 1000$ m marks the value of S_{1000} , which is the average signal obtained from the shower at a distance of 1000 m from the axis. One observable which takes advantage of the characteristic differences in the LDFs and has been used in previous analysis is S_b (see [SM13]). S_b will be discussed in more detail in Sec. 3. Since the existence of UHE photons could not be confirmed until now and there are still models like the GZK effect (see Sec. 1.2), which predict a certain photon flux below the current upper limits, there is a high interest in finding additional observables to improve the discrimination power between primary photons and hadrons and eventually probe those models.

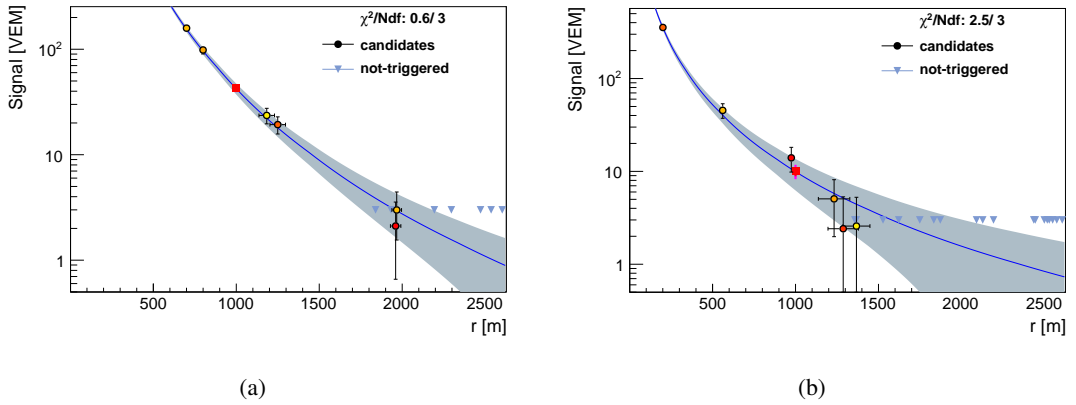


Figure 1.7.4: The lateral shower profile of (a) a simulated proton shower and (b) a simulated photon shower with a Monte Carlo (MC) energy of 10 EeV. The colored dots show the signal measured at different SD stations, while the color coding gives information of the triggering time (yellow $\hat{=}$ early, red $\hat{=}$ late), the triangles show the distances of non-triggered stations in the respective range and the value of S_{1000} is highlighted by the square marker at $r = 1000$ m.

The events are taken from the simulation sample IdSimQII04 (see Sec. 1.8.2).

1.8 Technical Utilities for the Analysis

To keep the procedure of the analysis performed for this thesis as transparent as possible, the technical utilities which were used for calculations, simulations and plotting of the results shall be briefly introduced in this section.

1.8.1 Tools Used for Calculations and Plotting

All analysis code has been written in the programming language C++ and compiled with the GNU Compiler Collection (GCC) v4.7. The air shower simulations have been performed using CORSIKA. CORSIKA is a tool for simulating the development of high energy air showers in the earth's atmosphere and has been developed and is maintained by the group of the Karlsruhe Institut für Technologie (KIT). The detector response of the Pierre Auger Observatory has been simulated with the Auger Offline Software Framework [AS07, AJ08], a framework which is continuously developed by the Auger Collaboration for detector simulation and data analysis and is required to be adaptable to the continuous change and upgrade of the observatory. Therefore, Offline is written in C++ and takes strong advantage of its object oriented structure which allows Offline to be set up of many independent modules which can be controlled and implemented by the user using XML files or Python scripts. The output in the form of Advanced Data Summary Trees (ADSTs) has been analyzed and plotted within the ROOT data analysis framework developed at CERN [AI15], which provides a huge collection of classes and structures for processing and visualization of large data samples.

1.8.2 Simulation Samples Used for the Analysis

In the procedure of the analysis, different simulation sets have been used. In the majority of tasks, the simulations (IdSimQII04) performed by Marcus Niechciol for the studies during his Ph.D. thesis [NM15] have been used. In these simulations, the detector is assumed to be ideal i.e. to work perfectly at every moment and the sky is free of aerosols and clouds. The air shower simulations of IdSimQII04 have been done with CORSIKA version 7.4000. Here, the interaction model QGSJETII-04 [OS11] has been used to describe hadronic interactions at high energies. For hadronic interactions below 80 GeV, the FLUKA 2011.2b.6 model [FA05] was used. To describe the electromagnetic part of an air shower, CORSIKA uses a modified version of the EGS4 model [NW85] developed at the Stanford Linear Accelerator Center (SLAC). As primary particles, photons and protons were simulated in the energy range between 1 EeV and 10 EeV. The energy range has been divided into 10 bins with a width of 0.1 in $\log_{10}(E/\text{eV})$. The energy spectrum in each bin follows a power law with a spectral index of -1 . The LPM effect for UHE photons is taken into account automatically with EGS4. Since the energy only goes up to 10 EeV the Preshower effect was not included in the CORSIKA simulations. To simulate the

detector response of the CORSIKA showers, they were given as input files to `Offline` v3p0r1 and placed in eye-centric mode where the maximum distance of a shower core to the FD telescope is a function of the shower energy. Further details on the simulation samples IdSimQII04 can be looked up in [NM15]. To check the effects of time dependency and realistic detector aging on the analysis, two sets of time dependent simulations (TdSimQII03 and TdSimQII04) performed by Mariangela Settimo were used. Both samples use CORSIKA version 6.390 as MC generator for air showers with FLUKA to simulate low energy hadronic interactions and the shower cores are randomly distributed over the whole detector array in the `Offline` part of the simulations. The difference between both samples is the high energy hadronic interaction model, where TdSimQII03 has been produced with QGSJETII-03 as IdSimQII04 has been produced with QGSJETII-04. Additionally, both samples were produced with a slightly modified versions of `Offline` v3p0r1 (TdSimQ04) and v2r9p5 (TdSimQ03), which include additional information about the SD trigger types. Usually the only trigger information which is stored in the output ADST file is the one from the trigger which initially triggered the event. Here, also the information about all trigger types which would have triggered the event are stored additionally. The simulated energy range is between 0.1 EeV and 100 EeV divided into energy bins of 0.5 in $\log_{10}(E/\text{eV})$ with a spectral index of -1 . Closer information on the CORSIKA data steering cards used for TdSimQII03 can be obtained from [SM10].

2 Studies of the Observable F_γ

2.1 Definition of F_γ

In [NM15] the new observable F_γ has been introduced which allows for separation between EAS induced by primary photons and hadronic particles. F_γ is defined as

$$F_\gamma := \frac{S_{1000|\gamma}}{S_{1000|Hybrid}} \quad (2.1)$$

with the two S_{1000} -like values $S_{1000|\gamma}$ and $S_{1000|Hybrid}$.

$S_{1000|Hybrid}$ is the S_{1000} value obtained by using the reconstructed energy and zenith angle from the FD measurement and inverting the standard SD calibration which is usually used to obtain the primary energy from the measured S_{1000} value. To obtain $S_{1000|Hybrid}$, one first has to calculate the quantity $S_{38|Hybrid}$ which is independent of the zenith angle:

$$S_{38|Hybrid}[VEM] = \sqrt[B]{\frac{E_{Hybrid}}{A}}, \quad (2.2)$$

with the empirical calibration parameters $A = (1.90 \pm 0.05) \times 10^{17}$ eV and $B = 1.025 \pm 0.007$ which are obtained using well measured hybrid events from the data [AA15a]. $S_{38|Hybrid}$ is the average S_{1000} value one would expect from an air shower with an energy of E_{Hybrid} observed under a zenith angle of 38° . The calibration curve which was used in [AA15a] to obtain the parameters A and B can be seen in Fig. 2.1.1.

Next, to introduce the dependence on the reconstructed zenith angle θ the constant intensity cut function $CIC(\theta)$ is used

$$S_{1000|Hybrid} = CIC(\theta) \times S_{38|Hybrid}, \quad (2.3)$$

where $CIC(\theta)$ is a 3rd order polynomial in $x = \cos^2(\theta) - \cos^2(38^\circ)$:

$$CIC(\theta) = 1 + Cx + Dx^2 + Ex^3, \quad (2.4)$$

with $C = 0.980 \pm 0.004$, $D = -1.68 \pm 0.01$ and $E = -1.30 \pm 0.45$ [AA15a]. The corresponding CIC curve can be seen in Fig. 2.1.2.

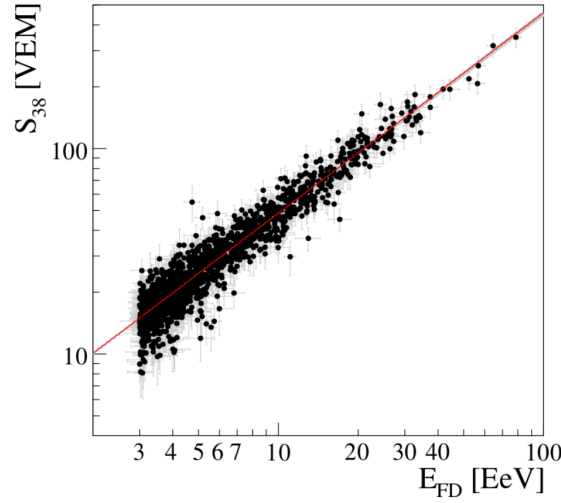


Figure 2.1.1: The correlation between S_{38} and the reconstructed FD energy for a set of well measured hybrid events.

A single power-law function has been fitted to the data points to obtain the parameters A and B in Eq. (2.2). (Picture adapted from [AA15a]).

$S_{1000|\gamma}$ takes advantage of the differently shaped lateral profiles of photon and hadron showers. While hadron induced air showers have a flatter lateral distribution function (LDF) due to their larger hadronic component, photon showers are mostly driven by electromagnetic interaction. Such electromagnetic showers are typically confined closer to the shower axis resulting in a steeper LDF than hadronic showers. To make use of those characteristics, simulated photon showers can be used to parametrize the typical shape of a photon like LDF. Assuming that the type of the primary particle determines the shape of the LDF completely, the only remaining free parameter of the LDF is a normalization factor which depends on the primary photon energy. The normalization factor $S_{1000|\gamma}$ is the value of the LDF at a distance of 1000 m from the shower core. By dividing $S_{1000|\gamma}$ by $S_{1000|Hybrid}$, the dependence on the primary energy and zenith angle is largely canceled out. Since $S_{1000|\gamma}$ is obtained by fitting a photon-like LDF, $S_{1000|\gamma}$ is still sensitive to the shape of the LDF and therefore to the type of the primary particle.

In this analysis $S_{1000|\gamma}$ is obtained by applying a constrained LDF fit with a modified NKG function of the form

$$S(r) = S_{1000|\gamma} \left(\frac{r}{1000m} \right)^{\beta(E,\theta)} \left(\frac{r + 1700m}{1000m} \right)^{\beta(E,\theta)} \quad (2.5)$$

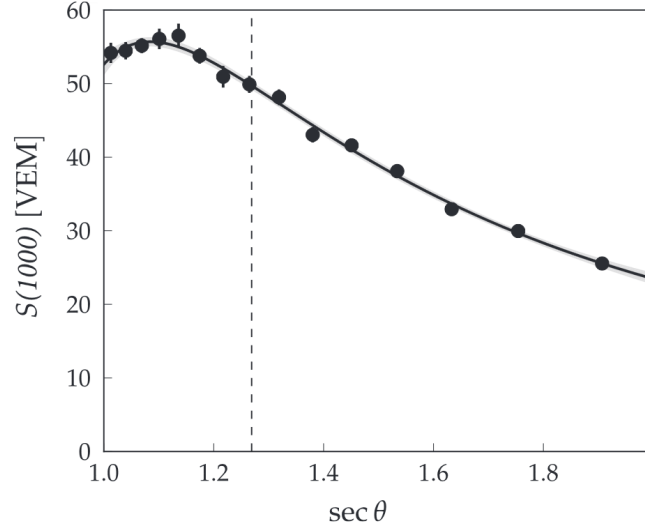


Figure 2.1.2: The correlation between S_{1000} and the secant of the zenith angle θ . In [AA15a], the data has been fitted by $CIC(\theta)$, a third order polynomial in $x = \cos^2(\theta) - \cos^2(\bar{\theta})$ with $\bar{\theta} = 38^\circ$. The dashed line marks the point $\theta = \bar{\theta}$.

to the signals measured by the SD stations, where the exponent β is no free parameter but a function of energy E and zenith angle θ . The parametrization of β has been done in [NM15] by using simulations of EAS initiated by primary photons at energies between 1 EeV and 10 EeV and fitting the function

$$\beta(E, \theta) = a_0(E) + a_1(E)(\sec(\theta) - 1)^3 \quad (2.6)$$

with

$$a_0(E) = b_0 + b_1 \log_{10}(E[eV]),$$

$$a_1(E) = c_0 + c_1 \log_{10}(E[eV]) + c_2 \log_{10}(E[eV])^2$$

to the values of the free β obtained from an unconstrained fit of Eq. (2.5). The results of the fit are

$$b_0 = -0.695 \pm 0.098$$

$$b_1 = -0.107 \pm 0.005$$

$$c_0 = 506.72 \pm 0.11$$

$$c_1 = -53.159 \pm 0.006$$

$$c_2 = 1.3972 \pm 0.0003.$$

For detailed information on the parametrization of the LDF see [NM15]. By taking the ratio of $S_{1000|\gamma}$ and $S_{1000|Hybrid}$ the energy dependence of those S_{1000} related parameters is canceled out to a large extent and the remaining observable F_γ is mainly sensitive to differences in the lateral shower profile. Hence, the separation power of F_γ between primary photons and hadrons is produced by the steeper profile of photon induced EAS. In order to analyze the separation power of F_γ between these different kinds of air showers a conservative approach has been chosen by only looking at the separation power between photons and protons instead of heavier nuclei or even a mixed hadronic composition to avoid the need of knowledge about the mass composition. Because proton induced EAS would have the most photon like lateral profile compared to heavier hadrons, the separation power of F_γ would be underestimated in the worst case by assuming a pure proton background. In Fig. 2.1.3 the distributions of F_γ and the corresponding statistical uncertainties are displayed for simulated photon and proton events in the energy range between $10^{18.0}$ eV and $10^{18.5}$ eV.

To get a quantitative impression of the separation power of the two distributions, the merit factor η as given by

$$\eta := \frac{|\mu_\gamma - \mu_p|}{\sqrt{\sigma_\gamma^2 + \sigma_p^2}} \quad (2.7)$$

has been calculated where $\mu_{\gamma(p)}$ denotes the mean value and $\sigma_{\gamma(p)}$ denotes the standard deviation of the photon (proton) distribution. Using the merit factor in this definition, η does not account for a possible asymmetry of the distributions. Hence η can only be used as a rough estimator of the separation power when comparing similarly shaped distributions. Since the purpose of this analysis is the identification of a tiny fraction of photons among a huge hadronic background the worrying part of the background distribution is the outer left tail i.e. the proton events which have by chance a photon-like F_γ value. To measure the extent of this part of the background, the background rejection ρ_{50} at the 50% signal efficiency mark has been calculated in addition to η . ρ_{50} is derived by counting the number of proton events which have a higher F_γ value than the median of the photon distribution and dividing by the total number of proton events. In Tab. 1 the separation power of F_γ in terms of η and ρ_{50} for ten different energy bins is compiled. The corresponding plots of the F_γ distributions can be found in the appendix (Fig. 5.0.1). The distributions of the uncertainty ΔF_γ in the 10 different energy bins is also shown in the appendix (Fig. 5.0.2).

Energy Bin	η	ρ_{50}
$18.0 \leq \log_{10}(E [\text{eV}]) < 18.1$	1.46	98.80%
$18.1 \leq \log_{10}(E [\text{eV}]) < 18.2$	1.56	99.22%
$18.2 \leq \log_{10}(E [\text{eV}]) < 18.3$	1.77	99.67%
$18.3 \leq \log_{10}(E [\text{eV}]) < 18.4$	1.88	99.45%
$18.4 \leq \log_{10}(E [\text{eV}]) < 18.5$	1.90	99.66%
$18.5 \leq \log_{10}(E [\text{eV}]) < 18.6$	2.13	99.73%
$18.6 \leq \log_{10}(E [\text{eV}]) < 18.7$	1.95	99.85%
$18.7 \leq \log_{10}(E [\text{eV}]) < 18.8$	2.26	99.85%
$18.8 \leq \log_{10}(E [\text{eV}]) < 18.9$	2.35	99.83%
$18.9 \leq \log_{10}(E [\text{eV}]) < 19.0$	2.42	99.94%

Table 1: The separation power of F_γ in terms of the merit factor η as defined in Eq. (2.7) and the background reduction ρ_{50} at a signal efficiency of 50% for 10 energy bins between 1 EeV and 10 EeV.

Simulations: IdSimQII04.

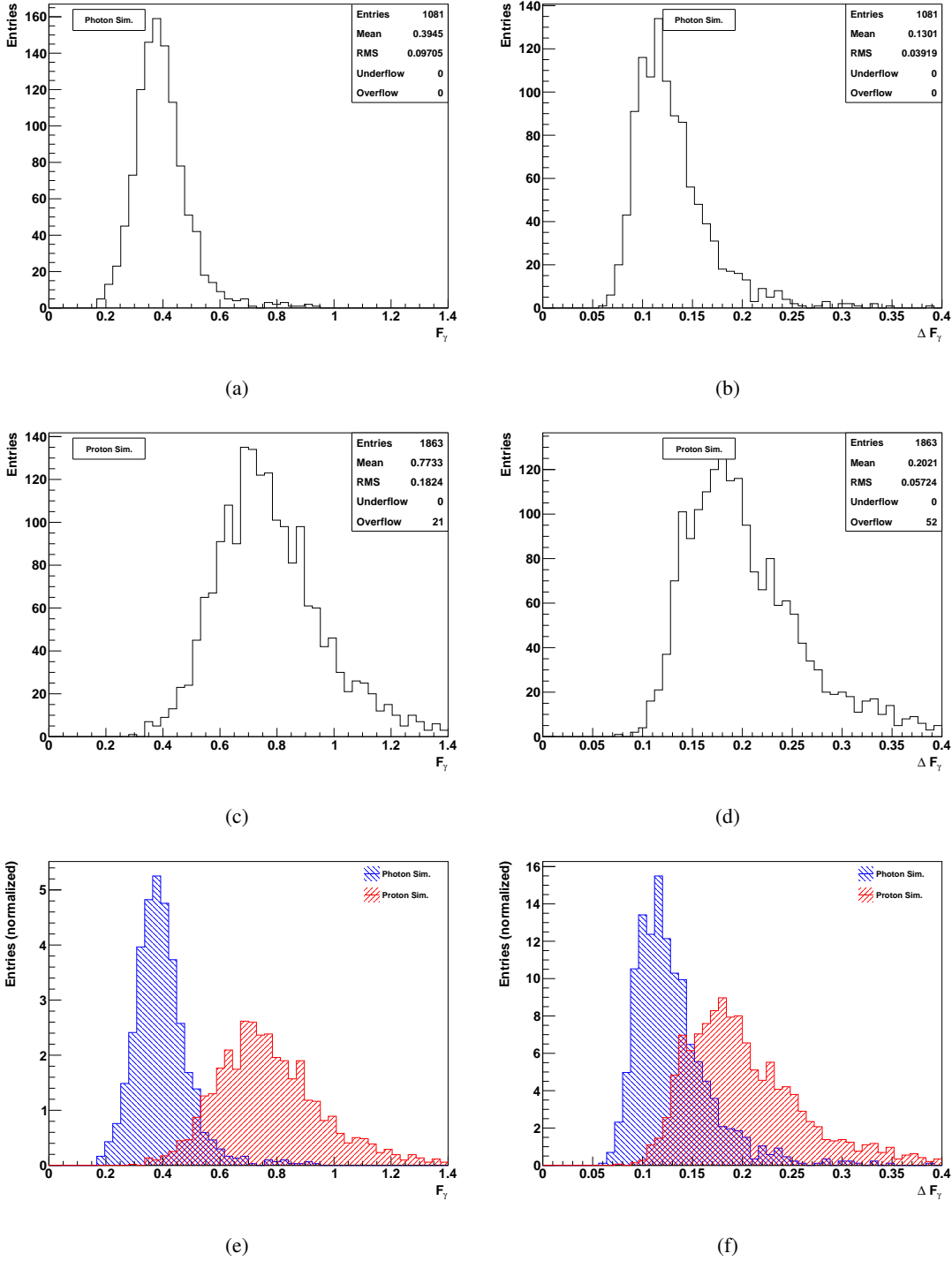


Figure 2.1.3: The separation power of F_γ between photon and proton induced air showers; left: the F_γ -distribution of (a) simulated photon showers, (c) simulated proton showers and (e) the overlay of the latter; right: the corresponding distributions of the individual uncertainties of F_γ derived using Gaussian error propagation. The F_γ shown here follows the latest definition after application of all cuts and selection criteria discussed in this thesis.

Simulations: idg4, $18.0 \leq \log_{10}(E [\text{eV}]) < 18.5$.

2.2 Changes in the F_γ Analysis

In [NM15] the F_γ analysis was introduced together with a set of event selection criteria on the preselection, geometry and profile level as well as some cuts on the F_γ level. In order to further improve the performance of the analysis some of these selection criteria have been revised. In the following those changes and their effects shall be introduced.

2.2.1 Including High-Gain Saturated Stations in the LDF Fit

When an SD station records a signal large enough to saturate the HG, the signal can in principle still be recovered from the LG. Nevertheless, in the previous analysis such events which had a saturated HG, were excluded from the data. This has been done as a measure of caution due to avoid signal reconstruction in the range where the HG was already saturated but the signal was still at the lower bound of sensitivity of the LG. Since it has been stated in [VD13] that the signal can now also be reconstructed from the LG sufficiently, there is no need to exclude those stations anymore when reconstructing F_γ . Crosschecks have been made to show the influence of the HG-saturated stations on F_γ in simulated photon and proton events. In Fig. 2.2.1 the F_γ distributions with and without the HG-saturated stations are shown. The main impact of including the HG-saturated stations is a gain in statistics mostly in the photon part of the simulations. This is due to the steeper lateral profile of an average photon shower which contains usually less triggered stations than a comparable proton shower. Particularly at lower energies there is a higher probability for a photon shower to have only one or two triggered stations. If those are very close to the shower axis the signal can still be high enough to saturate the HG. If the HG-saturated stations are rejected, these events would be removed completely from the data set. The overall shapes of the distributions do not change when including these stations as far as one can see by eye when looking at Fig. 2.2.1. This is confirmed by the merit factor which also does not significantly change (1.77 vs. 1.79) as well as ρ_{50} which goes from 98.5% to 99.0%. The slight increases in η and ρ_{50} can be explained by the fact, that the additional stations reduce the statistical uncertainty of the LDF fit in some cases, making the distributions slightly narrower. As a result, the recovery of the signal from the LG has shown to not introduce any bias or suspicious features to the analysis and seems to be consistent with the signal values obtained from the HG.

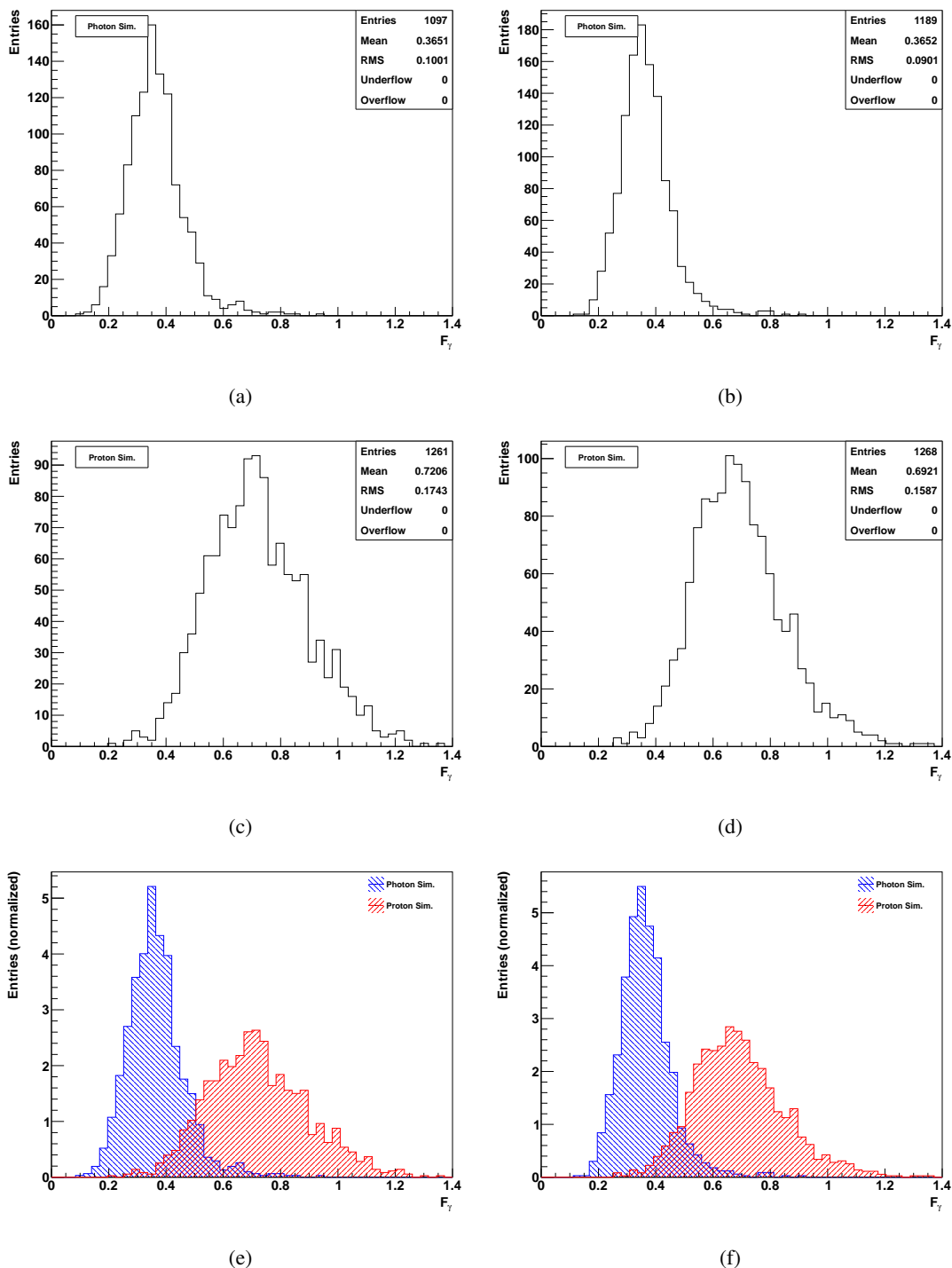


Figure 2.2.1: On the left (Figs. (a), (c) and (e)) the definition of F_γ as used in [NM15] is applied, on the right (Figs. (b), (d) and (f)) the High Gain saturated stations are included in the calculation of F_γ . The Low Gain saturated stations are excluded in both cases.

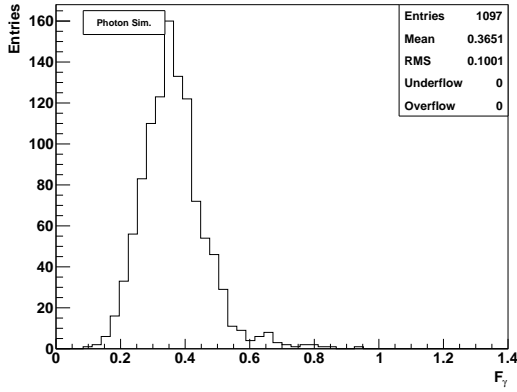
Simulations: IdSimQII04, $18.0 \leq \log_{10}(E [\text{eV}]) < 18.5$.

2.2.2 Including Non-Trigging Station up to 5000 m from the Core

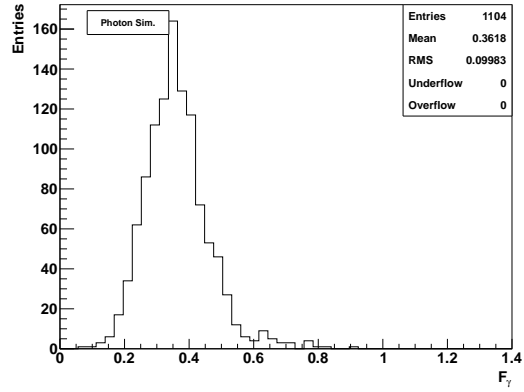
As a further constraint in the previous analysis, the range of non-triggering stations taken into account in the LDF-fit was limited to a distance of 800 m to 1500 m from the shower core while all triggered stations up to a distance of 3000 m were used. To check whether this constraint can be relaxed, the F_γ observable, calculated using all active stations up to 5000 m from the shower core has been compared to the analysis in [NM15] (see Fig. 2.2.2). By including all active stations in the respected range neither the merit factor (1.77 vs. 1.76) nor ρ_{50} (98.5% vs. 98.6%) do change significantly in the case of the simulation samples shown in Fig. 2.2.2. The increase of plotted events is due to the smaller uncertainty on F_γ caused by a larger number of stations entering the LDF fit. Since the cut sequence used in [NM15] includes two quality cuts on the uncertainty of F_γ (see Sec. 2.4) there are now more events which pass those cuts when taking non-triggering stations in a wider range into account.

2.2.3 Change in the Energy Calibration of the SD Array

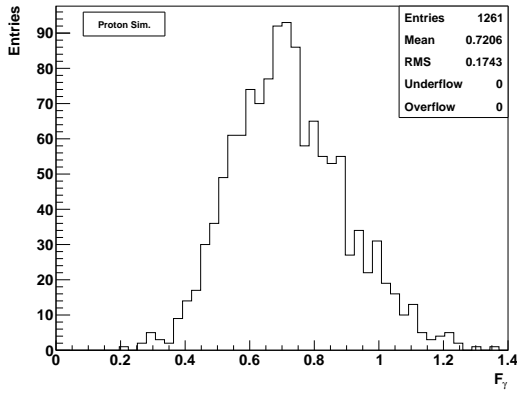
The common procedure used to derive the energy of the primary particle from the S_{1000} value has been modified for the ICRC 2015 [VI15] compared to the last publication in the ICRC 2011 [PR11]. In particular the shape of the CIC function has been changed from a quadratic shape $1 + ax + bx^2$, $a = 0.87$, $b = -1.49$ as it was also used in [NM15] to a cubic shape as described in Sec. 2.1. Some crosschecks (see Fig. 2.2.3) have been made to study the impact of this new calibration on the F_γ analysis. The change leads to a mean shift of $S_{1000|Hybrid}$ – the denominator of F_γ – of about -8% independent of the primary type. Since $S_{1000|\gamma}$ is not affected by the change of the CIC function, the change of F_γ is only caused by $S_{1000|Hybrid}$. Also at this point, the merit factor does not change significantly (1.77 vs. 1.76) as the value of ρ_{50} changes from 98.5% to 98.8%. The corresponding F_γ distributions are shown in Fig. 2.2.4. The small decrease in the number of plotted events is caused by the quality cuts on F_γ (see Sec. 2.4) which were introduced in the analysis of [NM15]. The new definition of the CIC function caused some of the events to have larger uncertainties so they did not pass those cuts anymore.



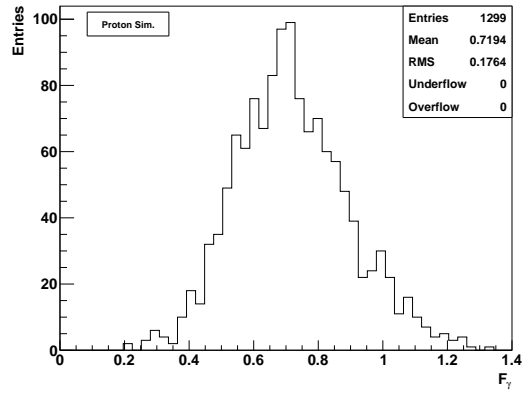
(a)



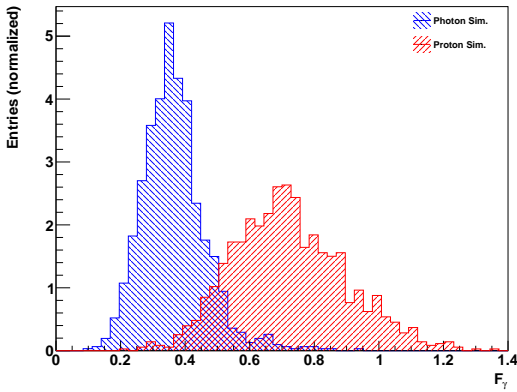
(b)



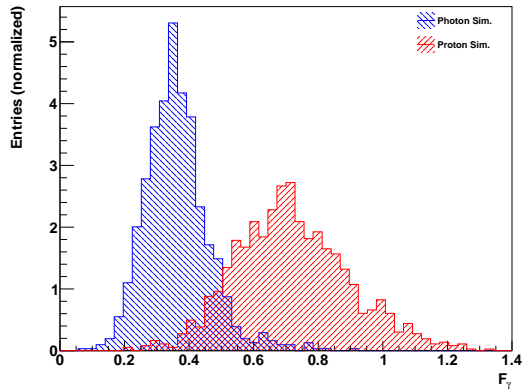
(c)



(d)



(e)



(f)

Figure 2.2.2: On the left (Figs. (a), (c) and (e)) the definition of F_γ as used in [NM15] is applied. The range of active non-triggered station taken into account for the determination of F_γ is from 800 m up to 1500 m from the shower core whereas all triggered stations from 0 m up to 3000 m are taken into account. In the plots on the right (Figs. (b), (d) and (f)) also all non-triggered stations up to 3000 m from the core are used.

Simulations: IdSimQII04, $18.0 \leq \log_{10}(E [\text{eV}]) < 18.5$.

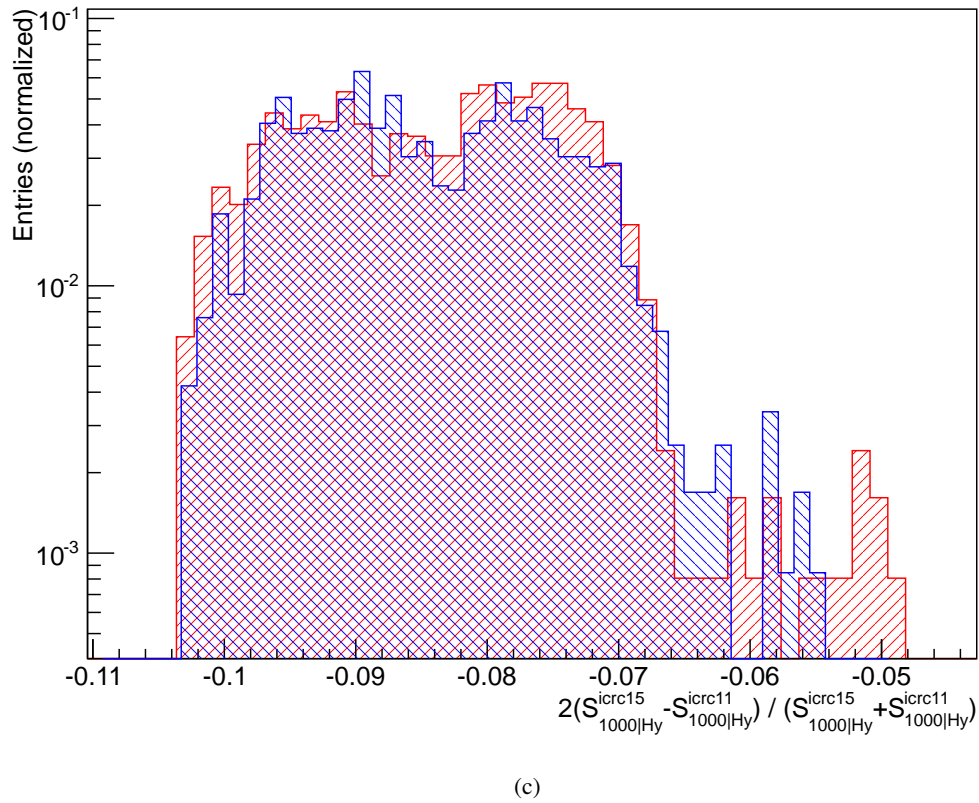
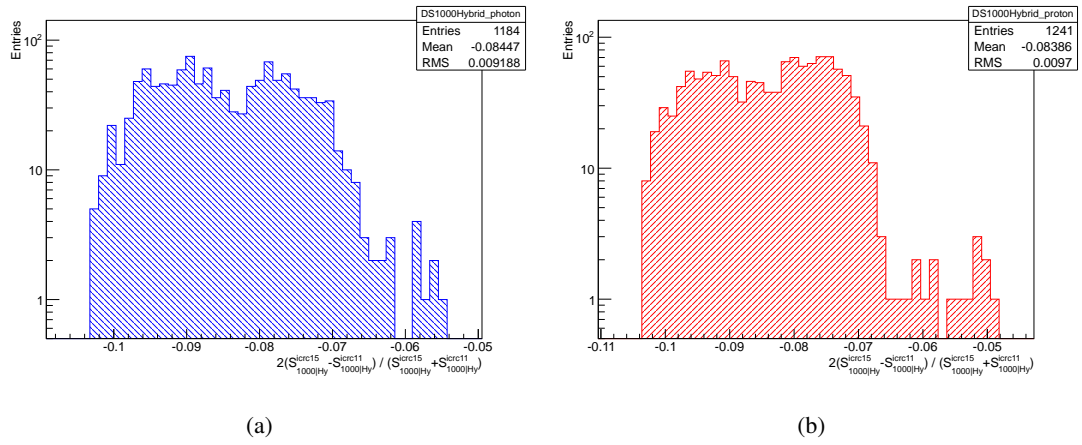


Figure 2.2.3: The change in the energy calibration of the SD array only affects the denominator of F_γ i.e. the $S_{1000|Hybrid}$. Therefore the relative difference between the old (ICRC 2011) and the new energy calibration (ICRC 2015) are displayed for (a) photon and (b) proton induced EAS. In in Fig. (c) the overlay of both distributions can be seen.

Simulations: IdSimQII04, $18.0 \leq \log_{10}(E [\text{eV}]) < 18.5$.

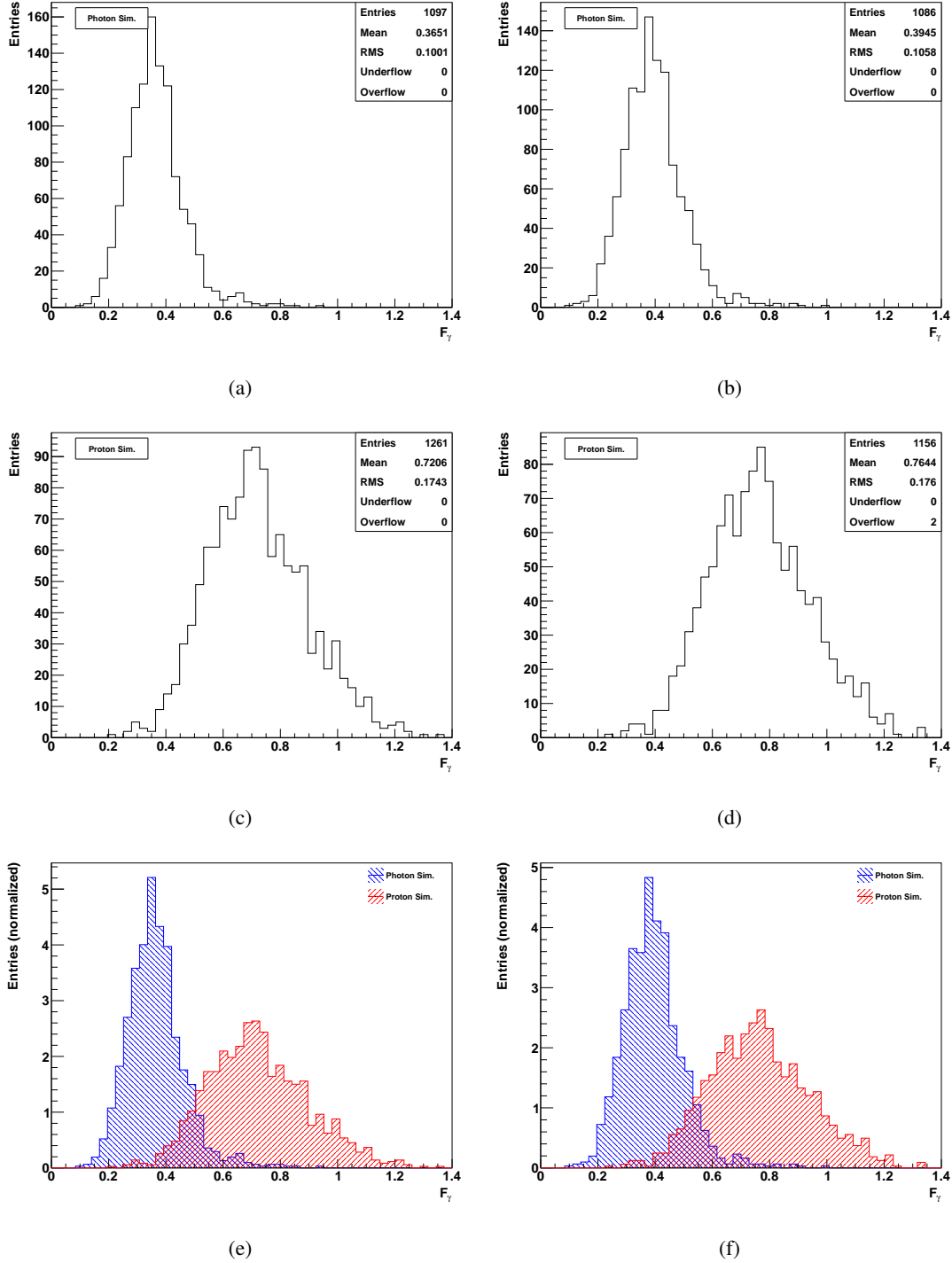


Figure 2.2.4: On the left (Figs. (a), (c) and (e)) the definition of F_γ as used in [NM15] is applied. The CIC function used to determine $S_{1000|Hybrid}$ is given by a 2nd order polynomial as described in Sec. 2.2.3. In the plots on the right (Figs. (b), (d) and (f)), a third order polynomial (see Eq. 2.4) is used as the CIC function. Simulations: IdSimQII04, $18.0 \leq \log_{10}(E [\text{eV}]) < 18.5$.

2.2.4 Including New Triggers in the LDF Function

In June 2013, two new trigger algorithms have been applied to the SD T1 trigger upon the ToT trigger. Those are the time-over-threshold-deconvolved (ToTd) trigger and the multiplicity-of-positive-steps (MoPS) trigger. Those new systems introduce a more sophisticated triggering logic to the digitized signals from the PMTs which effectively lower the triggering threshold allowing to measure lower signals than before. This modification has been done to improve the reconstruction of events and in particular the discrimination between photon and hadron events [AA15a, AA15b].

To analyze the impact of the new trigger algorithms MoPS and ToTd on F_γ , the time dependent simulation samples TdSimQII03 introduced in Sec. 1.8.2 were used because the additional triggering information for all trigger types (see Sec. 1.8.2) was needed for this analysis. The following plots (Fig. 2.2.5 to 2.2.7) show the impact of the new triggers on the observable. In Figs. 2.2.5 and 2.2.6, some specially selected events are shown which are chosen such, that the impact of the new triggers on F_γ should be maximal i.e. events with a large number of stations which are triggered by one of the new trigger types but would not have been triggered by the old ones. This approach has been chosen because there were no purely new trigger events which passed the quality cut on F_γ (see Sec. 2.4). So, in each event shown in Figs. 2.2.5 and 2.2.6 at least one station would also have been triggering with the old algorithms. While the new triggers do not affect the F_γ value for most of the events, some photon events appear to have a significantly smaller value. The changes at the proton events are more symmetric around zero. This behaviour is caused by the procedure used to derive F_γ . Non-triggering stations enter the maximum likelihood fit of the LDF with a Poissonian probability distribution. The expected value of this Poissonian distribution depends on the trigger probability at a certain signal and therefore on the triggering threshold. Since MoPS and ToTd lower the threshold, the uncertainty of the signal in non-triggering stations is overestimated by the way, the LDF fit is currently performed. In return, if a station would be triggered with MoPS and ToTd but not by the old algorithms, the LDF at this point is most likely shifted to lower values if the station is close to the axis and to higher values if it is farther away. Since the LDF of photon showers is on average steeper, it is more likely to measure a low signal close to the shower axis and this effect contributes mainly in one direction for photon events i.e. towards smaller values of the fit parameter $S_{1000|\gamma}$ – the counter of F_γ . For proton events, which have a higher probability for triggering also stations

farther away from the axis, the deviations of F_γ caused by this effect are distributed more symmetrically in both directions. The mean uncertainty of F_γ (Figs. 2.2.5 (b) and 2.2.6 (b)) goes down in almost all cases. This is expected since the new trigger algorithms can detect lower signals and therefore, if now stations with signal enter the LDF fit which were previously treated as non-triggering stations, the LDF is better determined and therefore has lower uncertainty. In Fig. 2.2.7 a comparison of the overall distributions of F_γ can be seen. The fact that there are significantly more events in the samples after including the new triggers is caused by the reduction of the F_γ uncertainties which makes the events more likely to pass the quality cuts introduced in [NM15] (see Sec. 2.4). By including the new triggers, the merit factor changes from 1.33 to 1.52¹. while the background reduction ρ_{50} changes from 93.6% to 95.7%. This change is also expected since the mean uncertainty of F_γ goes down by including the new trigger algorithms which leads to narrower distributions and therefore to a higher merit factor. In conclusion, using the new trigger algorithms does not degrade the separation power of F_γ . Nevertheless, the likelihood function for the constrained LDF fit should be modified to take into account the higher trigger probability at lower signals due to MoPS and ToTd. This modification is expected to increase the separation power of F_γ even further since the non-triggering stations close to the shower axis in photon events will have smaller uncertainty and therefore higher weight resulting in a lower F_γ value for photons.

¹Notice: Since the simulation sample TdSimQII03 is used here, the absolute value of the merit factors given here can not be compared to the ones given in Tab. 1 which belong to IdSimQII04. Only the change of the merit factor within the same simulation sample contains information. The difference between the two simulation samples in terms of the merit factor can have multiple reasons like the different hadronic interaction model, the distribution of the events over the SD array and also the borders and edges of the array which are not relevant in non-time depending simulations in the center of the field of view of an FD.

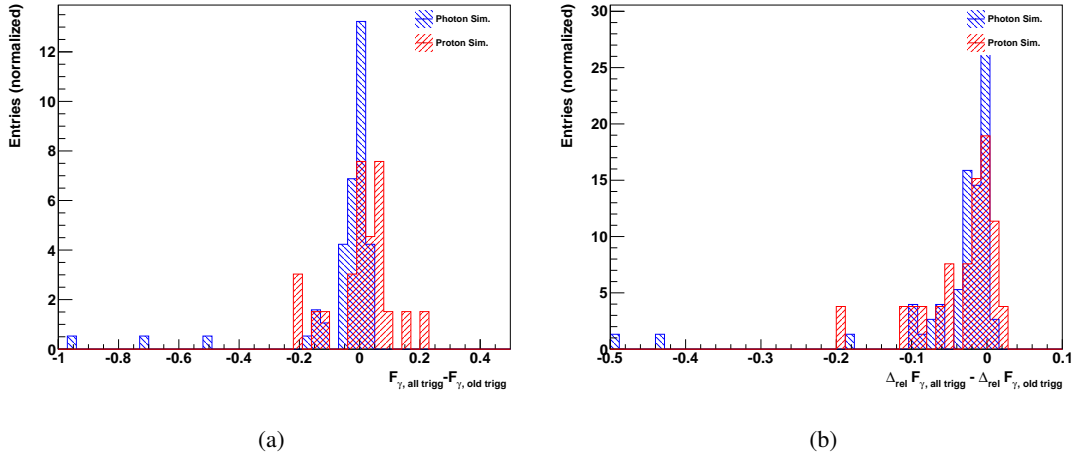


Figure 2.2.5: To quantify the impact of the new trigger algorithms on F_γ some specially selected events are shown: the SD event consists of exactly one station which was triggered by a new trigger and one station triggered by one of the old triggers. Fig. (a) shows the difference of the F_γ calculated using all available triggers to the F_γ calculated using only old triggers on exactly the same events. Fig. (b) shows the behavior of the error of F_γ .

Simulations: TdSimQII03, $18.0 \leq \log_{10}(E [\text{eV}]) < 18.5$.

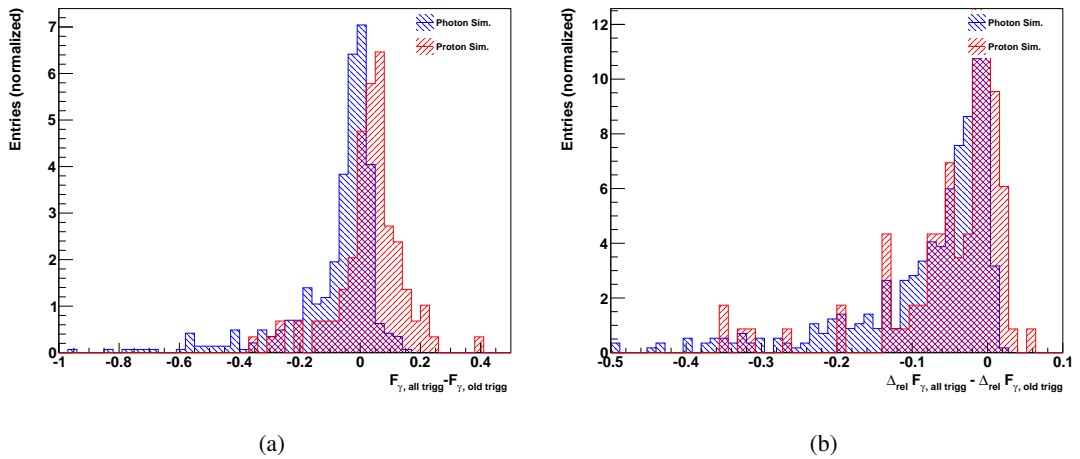


Figure 2.2.6: The impact of the new triggers on F_γ is shown for events in which one SD station was triggered by an old trigger and at least one station was triggered by a new trigger. Remark: It was not possible to look at events which were only triggered by new triggers because those events did either not pass the cut on the F_γ error (see Sec. 2.4) or had no triggered station at all without the new triggers such that a direct comparison was not possible.

Simulations: TdSimQII03, $18.0 \leq \log_{10}(E [\text{eV}]) < 18.5$.

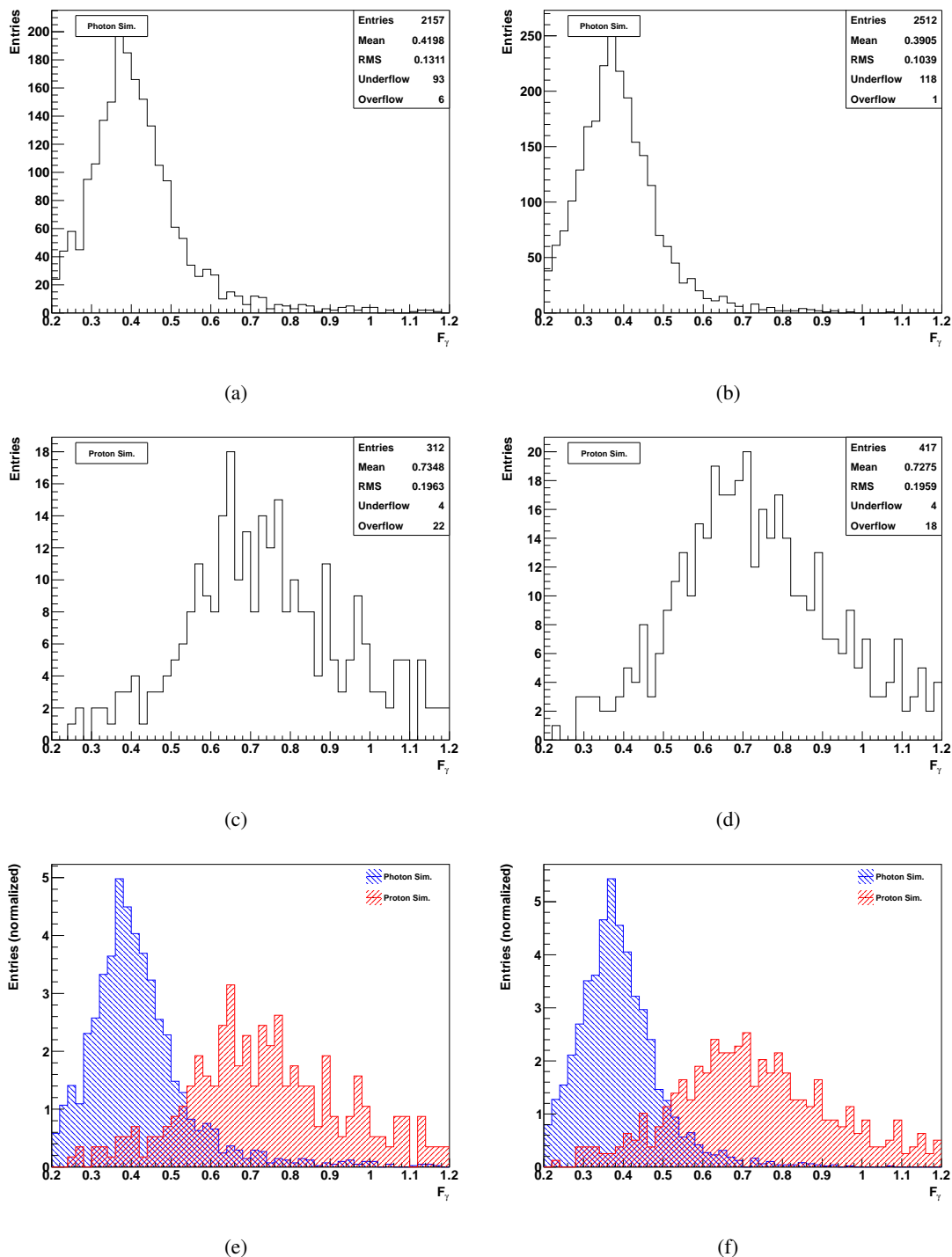


Figure 2.2.7: A comparison between the F_γ distributions with and without the new trigger algorithms. On the left (Figs. (a), (c) and (e)) only T1, T2 and TOT trigger are included. On the right (Figs. (b), (d) and (f)), all available trigger algorithms including MoPS and TOTd are used.

Simulations: TdSimQII03, $18.0 \leq \log_{10}(E [\text{eV}]) < 18.5$.

2.2.5 Event Selection

In order to have a set of only well measured EAS to perform the analysis on, a certain sequence of event selection criteria has been applied before calculating F_γ . This cut logic has been introduced and discussed in detail in [SM10].

FD Preselection:

1. FD telescope has to have worked properly at the time the event was detected and the geometry reconstruction includes at least 1 SD station
2. event must have reconstructed hybrid energy
3. in case more than one FD telescope allow a shower reconstruction the “best eye”, is selected i.e. the eye with the smallest relative uncertainty on X_{max}

Geometry cuts:

4. $0 \text{ m} < \text{distance from the hottest station (FD)}^2 \text{ to the shower axis} < 1500 \text{ m}$
5. SD-FD time difference $< 200 \text{ ns}$
6. χ^2/Ndf of SDP-fit < 7 with $\chi^2 > 0$ and $0 < \text{Ndf} < 4$
7. χ^2/Ndf of the time fit of the FD event < 8 with $\chi^2 > 0$ and $\text{Ndf} > 0$
8. only showers with zenith angle $\theta < 60^\circ$
9. angular track length of the FD event $> 15^\circ$

Profile cuts:

10. X_{max} in field of view (FoV) of the FD telescope
11. $\Delta E/E$ measured by the FD < 0.2
12. fraction of Cherenkov light < 0.5
13. χ^2/Ndf of the Gaisser-Hillas fit < 2.5
14. holes in the measured longitudinal shower profile must be less than 20% of the whole measured profile

SD Preselection:

15. time period is not marked as "bad period"³
16. SD event has at least one triggered station

Additional cut for F_γ :

17. photon-optimized LDF fit succeeds

In the analysis presented in this thesis, this cut sequence replaces the one which was previously applied on F_γ in [NM15]. Most of the cuts applied here were also included in the cut sequence from [NM15], except cut #9 and #14. In [NM15] the "hottest" FD eye – the one with the highest calorimetric energy – was used instead of the best eye and there were no restrictions on the χ^2 and the Ndf of the SDP- and the time fit itself like in cut #6 and #7. The upper limit on the χ^2/Ndf was 1.9 instead of 2.5 (cut #13). Additional cuts which are not applied here were used in [NM15] to optimize the quality of the events for the needs of the analysis presented there.

To get a feeling of how many events are ruled out by each of those cuts, the number of surviving events has been calculated after dropping always one cut out of the sequence. In Fig. 2.2.8 the percentage gain in statistics for each dropped cut is displayed. The numbers shown on the horizontal axis correspond to the cut numbers from the enumeration above. This event selection sequence is applied on each event before calculating the value of F_γ . As can be seen in Fig. 2.2.8, the cuts, which rules out the most events are the cut on the angular track length of the shower axis observed by the FD (cut #9) and the requirement for X_{max} to be in the field of view of the respective FD telescope. It is important for the analysis with F_γ to have a good reconstruction of the shower axis as well as a good reconstruction of X_{max} , since X_{max} shall be used as a complementary observable to F_γ to identify photon events. Hence, at this point these cuts were not considered to be relaxed in favor of high statistics. The cut on highly inclined showers (cut #8) which rejects about 7.5% of the events is also necessary to avoid a bias due to

²The hottest station in terms of the FD event is the SD station, from which the timing and position information is used to help reconstructing the shower axis in hybrid events. It is not necessarily the station with the largest signal, which is referred to as the hottest station of the SD event.

³Time periods, in which the event reconstruction is considered to be not trustworthy due to erroneous calibration of the FD telescopes, wrong GPS information or other known problems with the detector are marked as "bad periods" and stored in a database that they can be excluded in later analysis.

the earth's curvature and large travel distances through the atmosphere and should at this point not be relaxed either.

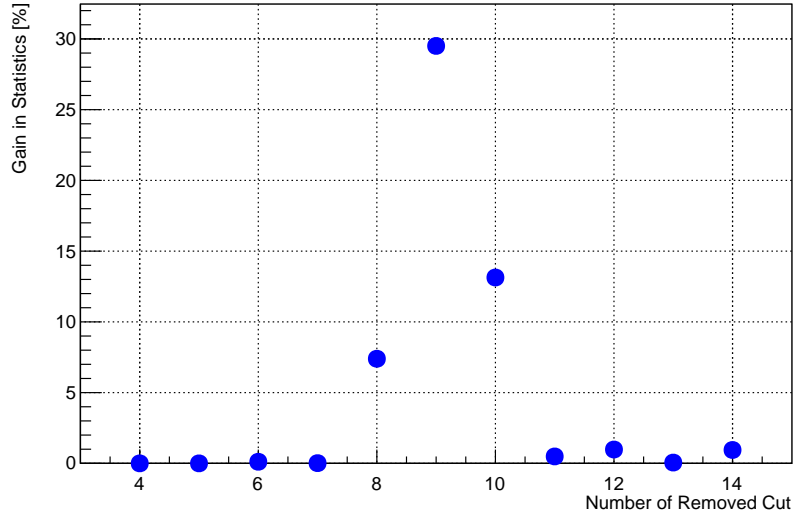


Figure 2.2.8: The percentage gain of statistics by dropping always one cut out of the list from above. The numbers on the x-axis correspond to the cut numbers in the list. Beginning with cut # 4 and ending with cut # 14 all geometry and profile cuts are analyzed here. Notice, the quality cut on the error of F_γ has not been implemented here and the shower simulations used are photon showers with an ideal array configuration.

Simulations: IdSimQII04, $18.0 \leq \log_{10}(E [\text{eV}]) < 18.5$.

2.3 Robustness Checks

To obtain a full understanding of F_γ , it is necessary to study the behavior of the observable in extreme cases and at the limits of its applicability. Especially when searching for photon candidates it is crucial to know about the weaknesses and limits of an observable to avoid artificially created candidates due to unknown systematic uncertainties.

2.3.1 Events With Few Triggered Stations

Since the photon-optimized LDF (Eq. (2.5)) has only one free parameter $S_{1000\gamma}$ it is technically possible to fit this function to a single data point and therefore apply the F_γ analysis on hybrid events with a single triggered SD station. Whether the value of F_γ is still reliable in events with only one or two triggered stations has been checked using different approaches. The simulated

events in Fig. 2.3.1 have been classified by their number of triggered stations. The candle plots illustrate the shapes of the F_γ distributions in each bin as described in the caption of Fig. 2.3.1. As one can see, the mean value of F_γ remains to a large extent unchanged independently of the number of triggered stations used for the LDF fit in the considered range. The small trend to higher F_γ values with more triggered stations in the case of proton events is caused by upward fluctuating signals in SD stations which are more distant to the shower core. Those would lead to a flatter LDF and therefore a larger F_γ value on average. Nevertheless, the trend stays well within the range of the event-to-event fluctuations. This shows that the mean value of F_γ is still reliable at events with only one or two triggered SD stations.

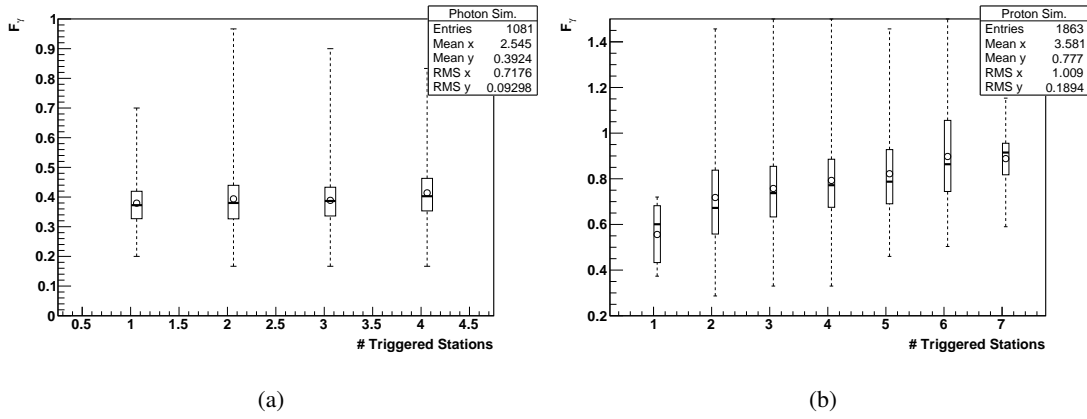


Figure 2.3.1: The dependence of F_γ on the number of triggered stations used in the LDF fit for (a) simulated photon events and (b) simulated proton events in a 5km range around the shower core. The candle plots show the minimum and the maximum values of the distributions in each bin by the limits of the dashed lines. The white bar marks the lower and the upper quartile (the 25% and 75% quantile) and the median is marked by the intercepting line in each bar. The circles show the position of the mean value for each distribution.

Simulations: IdSimQII04, $18.0 \leq \log_{10}(E [\text{eV}]) < 18.5$.

Another crosscheck to confirm the consistency of F_γ and the photon-optimized fit has been done by using an artificial dense SD array with a spacing of 433 m between neighboring tanks. F_γ has been calculated using all stations available in the 433 m array and subsequently restricting the number of stations entering the photon-optimized fit to the contents of a 750 m and a 1500 m array. This study has been done in the energy bin $18.0 \leq \log_{10}(E [\text{eV}]) < 18.5$ (see Fig. 2.3.2(a), 2.3.3(a) and 2.3.4(a)) and in the energy bin $18.5 \leq \log_{10}(E [\text{eV}]) < 19.0$ (see Fig. 2.3.2(b), 2.3.3(b) and 2.3.4(b)). Since this issue is purely SD related, $S_{1000\gamma}$ is the only

affected quantity and the relative change in $S_{1000\gamma}$ is the same as for F_γ . In Fig. 2.3.2, the overlays of the $S_{1000\gamma}$ distributions are shown for all three array geometries. As one can see, the shape of the distributions stays the same, when stations are removed from the 433 m array. That the average of $S_{1000\gamma}$ is very robust against restricting the number of stations can also be confirmed when looking at the individual changes of $S_{1000\gamma}$ (Fig. 2.3.3). When directly comparing the 433 m array to the 1500 m array, the relative changes of the $S_{1000\gamma}$ values are almost perfectly symmetric around zero, while the mean deviation for a single event is in the order of 20%. In Fig. 2.3.4, the deviations of $S_{1000\gamma}$ are grouped by the number of triggered stations in the 1500 m array. The distributions in each bin seem to follow no global trend depending on the number of stations. Since the average $S_{1000\gamma}$ does not change significantly as shown by those plots, it can be stated, that F_γ can be reconstructed from the 1500 m array without introducing a strong bias compared to a denser array geometry. This result also confirms that F_γ is, to a large extent, unbiased by the number of triggered stations entering the LDF fit and has consistent value even at events with a low number of triggered stations.

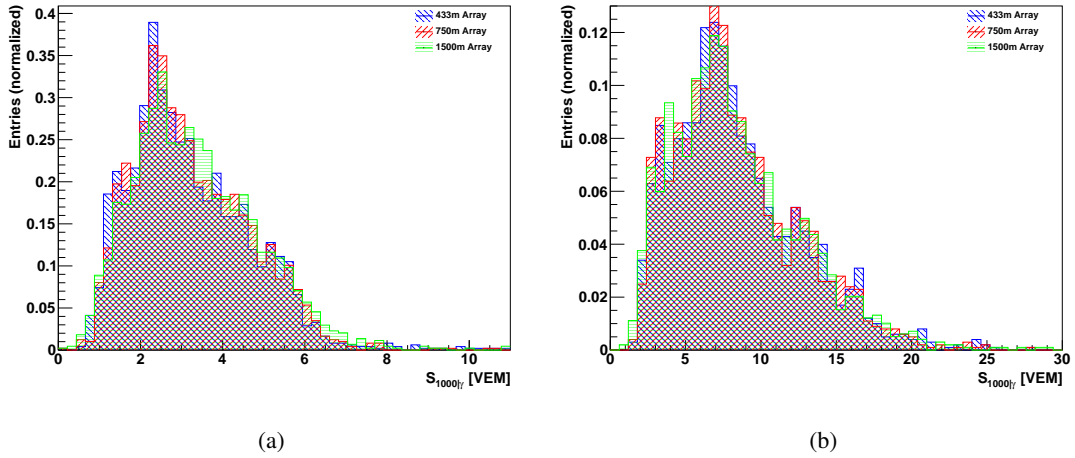


Figure 2.3.2: Result of the photon-optimized fit for simulated photons (distributions of $S_{1000\gamma}$) using different array geometries.

Simulations: IdSimQII04, (a) $18.0 \leq \log_{10}(E [\text{eV}]) < 18.5$, (b) $18.5 \leq \log_{10}(E [\text{eV}]) < 19.0$.

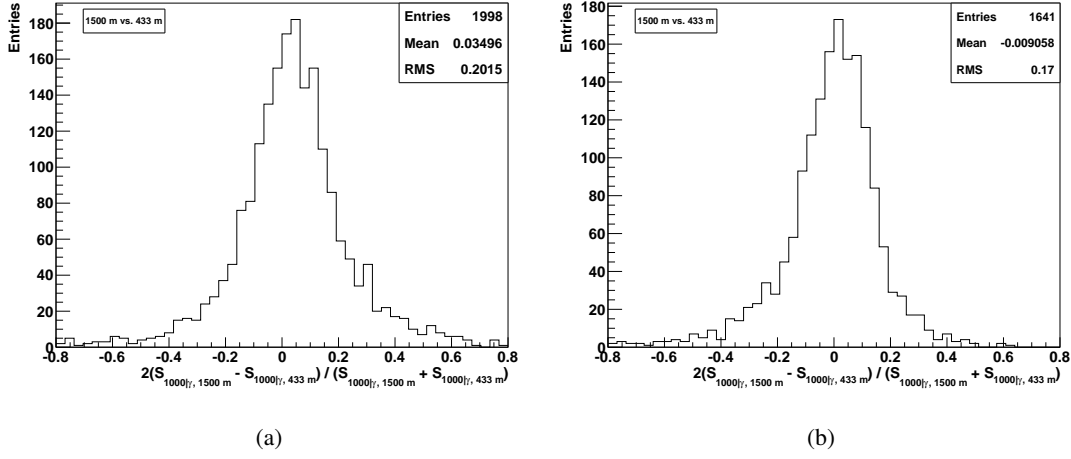


Figure 2.3.3: Event-by-event comparison of the results of the photon-optimized fit for the 433 m and 1500 m arrays for simulated photon events.

Simulations: IdSimQII04, (a) $18.0 \leq \log_{10}(E [\text{eV}]) < 18.5$, (b) $18.5 \leq \log_{10}(E [\text{eV}]) < 19.0$.

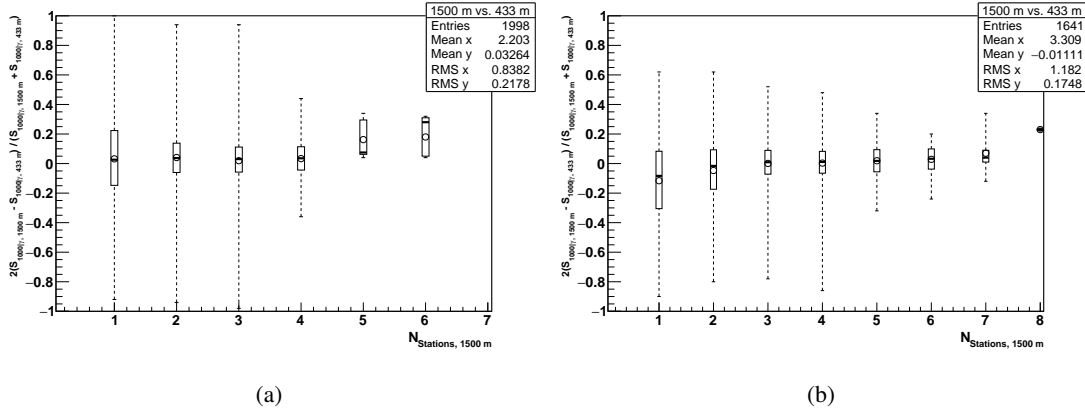


Figure 2.3.4: Event-by-event comparison of the results of the photon-optimized fit for the 433 m and 1500 m arrays for simulated photon events. The difference in $S_{1000\gamma}$ for both detector geometries as a function of the number of triggered stations entering the fit in the 1500 m array. A description of the marker notation of the candle-plots can be found in the caption of Fig. 2.3.1.

Simulations: IdSimQII04, (a) $18.0 \leq \log_{10}(E [\text{eV}]) < 18.5$, (b) $18.5 \leq \log_{10}(E [\text{eV}]) < 19.0$.

Since the convergence of the photon-optimized fit is a necessary condition for the derivation of F_γ (see Sec. 2.2.5), the relative frequency of failed LDF fits has also been analyzed with respect to the number of station entering the fit. From Fig. 2.3.5 one can conclude that the events with few triggered stations are fitted well throughout the simulation sample since no fit failed which had less than five triggered stations entering the fit. For events with a higher number of stations also no correlation could be observed between the relative frequency of failed fits and the number of stations. Though, it is not yet clear what the technical reasons are for the failure of the fitting procedure.

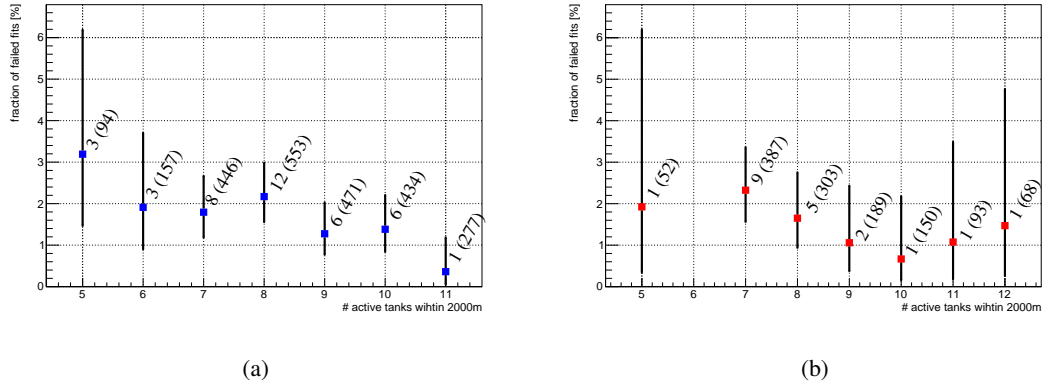


Figure 2.3.5: Number of Failed Fits as function of the number of triggered stations for (a) simulated photon events and (b) simulated proton events. The numbers above each point give the actual number of failed fits and the number in parenthesis is the total amount of events in the corresponding bin. The error bars show the upper and lower limits of the Clopper-Pearson interval⁴ at a confidence level of 68%.
Simulations: IdSimQII04, $18.0 \leq \log_{10}(E [\text{eV}]) < 18.5$.

2.3.2 Application of the β Parameterization Above 10 EeV

The photon-optimized LDF (Eq. (2.5)) relies on a parameterization of the exponent $\beta = \beta(E, \theta)$ (Eq. (2.6)) as a function of energy and zenith angle. Since the parameterization has been done using primary photons up to 10 EeV it is not clear to which extent it is still valid at higher

⁴The Clopper-Pearson (CP) confidence interval, also called "exact binomial", was defined in 1934 by C. Clopper and E. S. Pearson [CC34]. It is derived by inversion of the binomial distribution. Having a sample of size N and assuming the frequency of positive results in a binary stochastic experiment to be k , the upper and lower bounds p_u and p_l of the CP interval at a confidence level α are derived by finding the binomial distributions with mean values p_u and p_l such that the $(1 - \frac{\alpha}{2})$ -quantile of the distribution with mean value p_l equals the $\frac{\alpha}{2}$ -quantile of the distribution with mean value p_u equals k .

energies. Since the Pierre Auger Observatory measures primary energies up to ~ 100 EeV it is necessary to check whether the β parameterization can be safely extrapolated to higher energies or has to be extended to a wider energy range. In the following plots (Figs. 2.3.6 and 2.3.7), the parametrization is applied to simulated events with primary energies above 10 EeV to check if there is a significant bias. In the energy range $19.5 \leq \log_{10}(E [\text{eV}]) < 19.6$ the mean shift of β is about 5% towards smaller values compared to a free fit of the LDF for photon simulations. The discrepancy between the parametrized and the free β in the case of proton simulations in Figs. 2.3.7(c) and 2.3.7(d) is expected because the parametrization is optimized for primary photons. The impact on the F_γ value for photons can be seen in Fig. 2.3.6, where F_γ is compared to $F_{\gamma, \text{free}\beta}$ which is obtained from an unconstrained fit of the LDF. By increasing the energy by 0.6 in $\log(E)$, the difference between F_γ and $F_{\gamma, \text{free}\beta}$ does not increase. These results show, that the β -parametrization used here can also be applied at energies up to $10^{19.6}$ eV. Whether the parametrization is still valid at even higher energies has not been tested yet. But since there barely are any measured events above that energy, there is currently no need to apply F_γ to even higher energies.

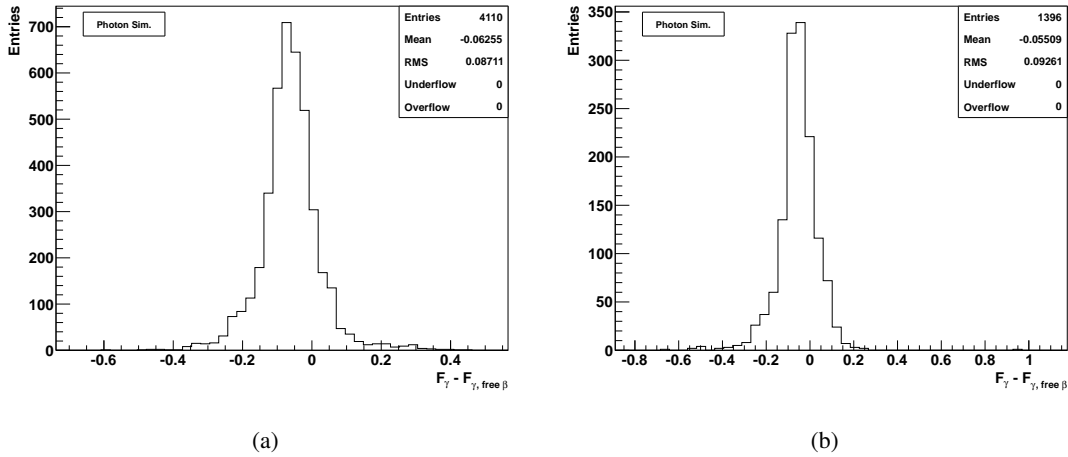


Figure 2.3.6: Application of the β parametrization to simulated photon events with primary energies above 10 EeV.

Difference between the F_γ obtained from an unconstrained fit of the LDF and the value obtained by applying the β -parametrization (Eq. (2.6)) on simulated photon events.

Simulations: IdSimQII04, (a) $18.9 \leq \log_{10}(E_\gamma [\text{eV}]) < 19.0$, (b) $19.5 \leq \log_{10}(E_\gamma [\text{eV}]) < 19.6$.

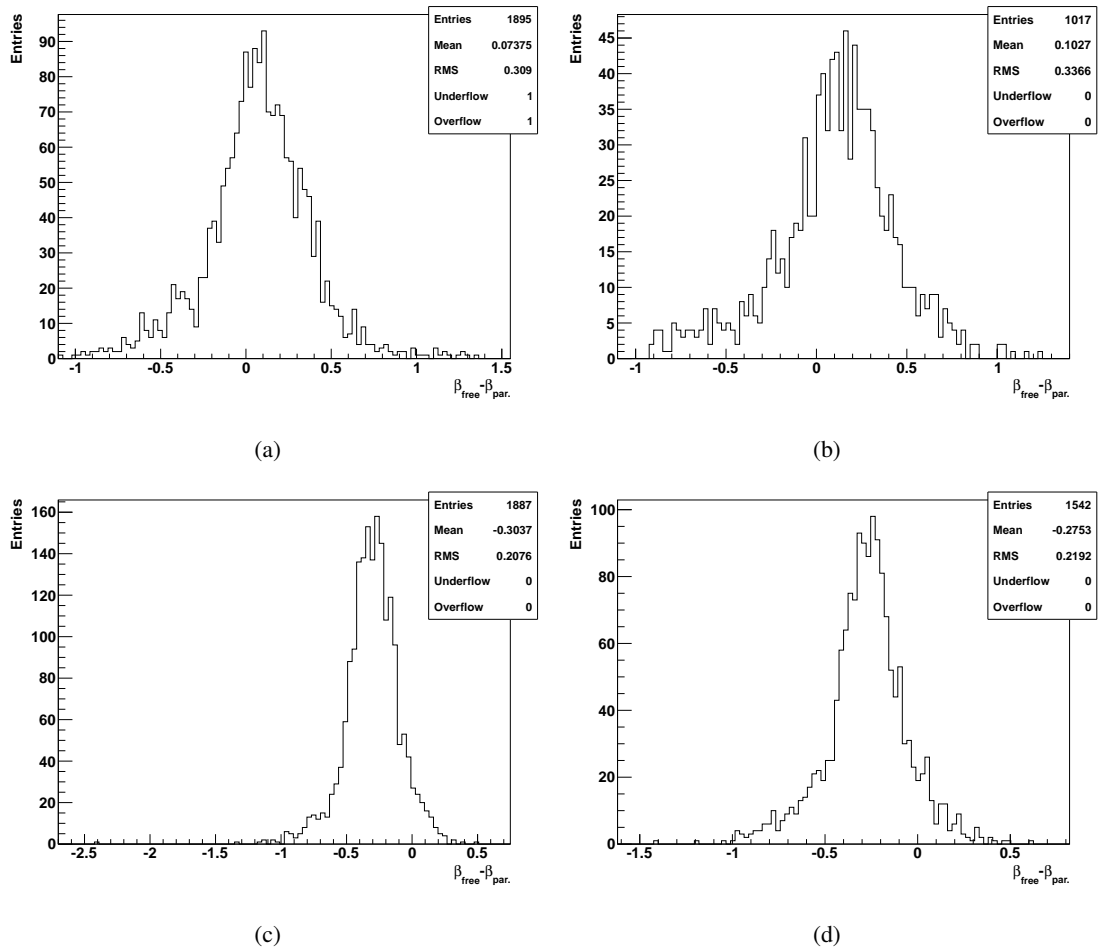


Figure 2.3.7: Application of the β parametrization to simulated photon events with primary energies above 10 EeV.

Difference between the β obtained from an unconstrained fit of the LDF and the value obtained from the parametrization (Eq. (2.6)).

Simulations: IdSimQII04, (a) Photon, $18.9 \leq \log_{10}(E [\text{eV}]) < 19.0$, (b) Photon, $19.5 \leq \log_{10}(E [\text{eV}]) < 19.6$, (c) Proton, $18.9 \leq \log_{10}(E [\text{eV}]) < 19.0$, (d) Proton, $19.5 \leq \log_{10}(E [\text{eV}]) < 19.6$.

2.4 Quality Cut Analysis

Each air shower has an individual uncertainty on F_γ (see Fig.2.1.3) depending on the measurement quality. Hence there is an opportunity to reject not well reconstructed events in order to avoid having photon candidates with large uncertainties and large fluctuations in the expected amount of photon candidates when applying the analysis to data. This has been done in the previous analysis with F_γ presented in [NM15], where a cut on the absolute error $\Delta F_\gamma < 0.35$ and at the same time on the relative uncertainty $\Delta F_\gamma / F_\gamma < 0.7$ has been applied. Since this cut has been chosen to be very strict in order to cull only the best measured events, it shall be discussed in this section if this cut can be relaxed to gain more statistics. Since in the task of photon-hadron discrimination especially those events with a small F_γ value are of interest, it has been found that there is no need to cut on the absolute error of F_γ which would affect particularly events with a high F_γ . This can be concluded when looking at the correlation between F_γ and ΔF_γ in Fig. 2.4.1.

The possibility of a quality cut on the relative error of F_γ has been analyzed in Figs. 2.4.2 and 2.4.3. The dependence of the merit factor on the cut value on $\Delta F_\gamma / F_\gamma$ shows that the cut value should not be chosen to be less than 0.5. Below this value, the merit factor is strongly influenced by event-to-event fluctuations in the lowest energy bin as one can see in Fig. 2.4.2. Above 0.5, the merit factor stays at an approximately constant level. Already at this value the photon efficiency in this energy bin is 80%. Since the uncertainties decrease at higher energies one could also consider to make an energy dependent cut on $\Delta F_\gamma / F_\gamma$. In the energy bin $18.9 \leq \log_{10}(E [\text{eV}]) < 19.0$, for example, one could achieve the same photon efficiency of 80% when

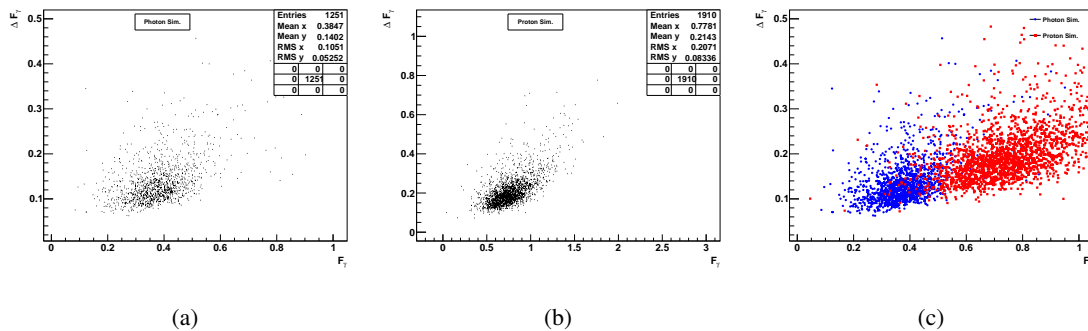


Figure 2.4.1: The correlation between F_γ and ΔF_γ for (a) simulated photon events (b) simulated proton events and (c) the overlay of both (photon in blue, proton in red).

Simulations: IdSimQII04, $18.0 \leq \log_{10}(E [\text{eV}]) < 18.5$.

requiring the relative uncertainty to be $\Delta F_\gamma / F_\gamma \lesssim 0.25$. For the contents of this thesis, a constant cut value at $\Delta F_\gamma / F_\gamma < 0.5$ has been chosen as the optimal value for an energy independent cut above 1 EeV.

To get an impression of the events in the F_γ distribution which are affected by the $\Delta F_\gamma / F_\gamma$ -cut, the number of events in each bin of the F_γ distributions with the cut have been subtracted by the number of events in the same bin of the distribution without the cut (Fig. 2.4.3). The figure shows, that events on the tails of the distributions are relatively more affected by the cut than those close to the mean. This behavior is expected since the events with larger uncertainties which are ruled out by the cut are more likely to fluctuate far from the mean value. Considering the mean of the F_γ distribution for photons to be at ~ 0.4 the cut subtracts an approximately constant amount of photon events with a large relative uncertainty throughout the F_γ spectrum. In the case of protons, the left tail is more affected by the cut than the right tail. This is caused by the larger width of the proton F_γ distribution leading to softer cut on the absolute error on the right tail than on the left since the cut affects the relative uncertainty. This effect additionally reduces the probability of having protons with a large uncertainty identified as photon candidates because those are the ones with downward fluctuating F_γ values.

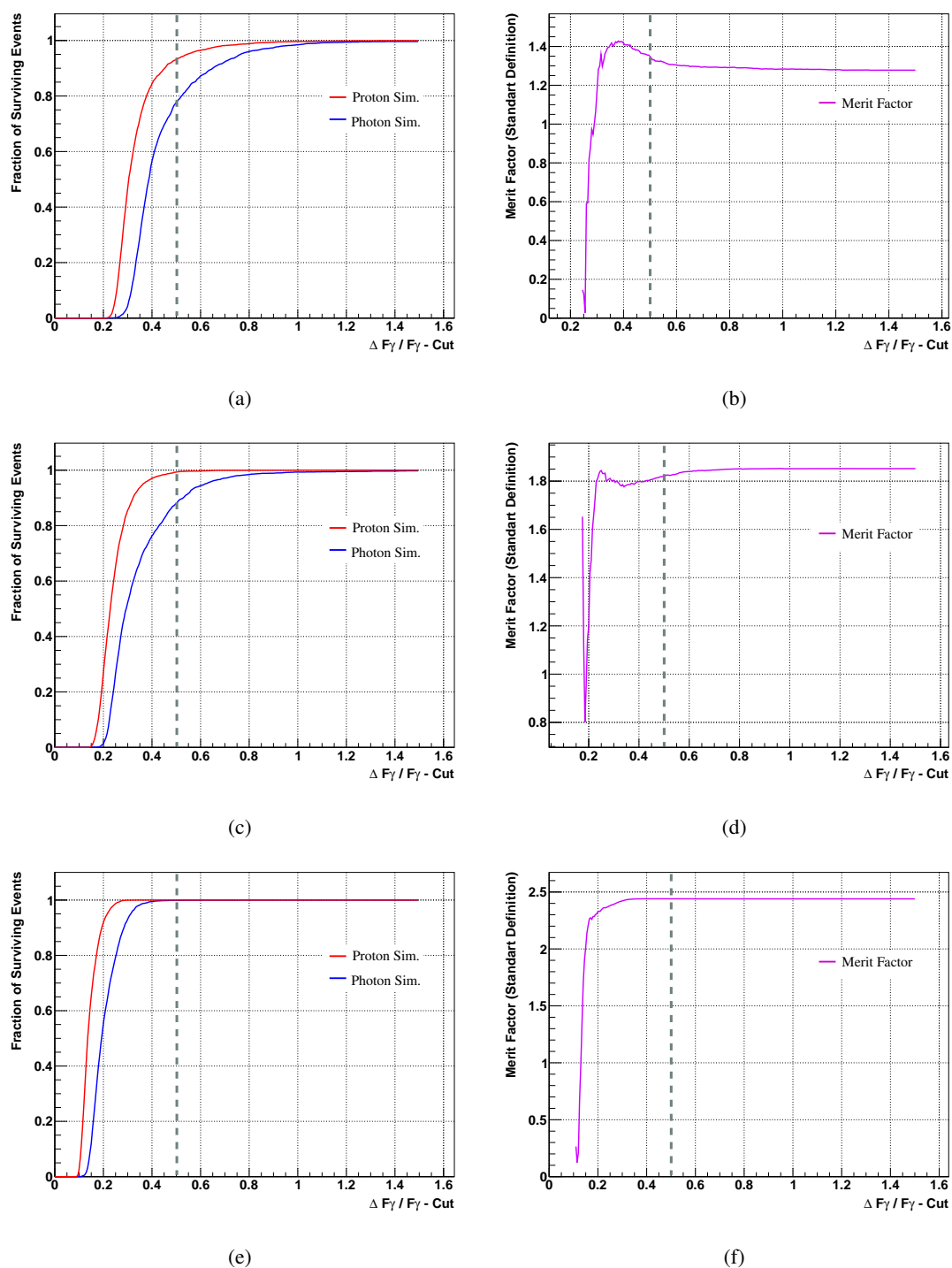


Figure 2.4.2: In (a) and (b), the behavior of simulated proton and photon events under variation of the cut value on the relative error of F_γ is shown for the energy bin $18.0 \leq \log_{10}(E [\text{eV}]) < 18.1$. (a) shows the number of events which survive the cut at the given value, where the blue line denotes photon simulations and the red line proton simulations. (b) shows the corresponding behavior of the merit factor. Figures (c) and (d) provide the same information for the energy range $18.4 \leq \log_{10}(E [\text{eV}]) < 18.5$ as well as figures (e) and (f) for the energy range $18.9 \leq \log_{10}(E [\text{eV}]) < 19.0$. The dashed line marks the proposed cut value at $\Delta F_\gamma / F_\gamma = 0.5$.

Simulations: IdSimQII04.

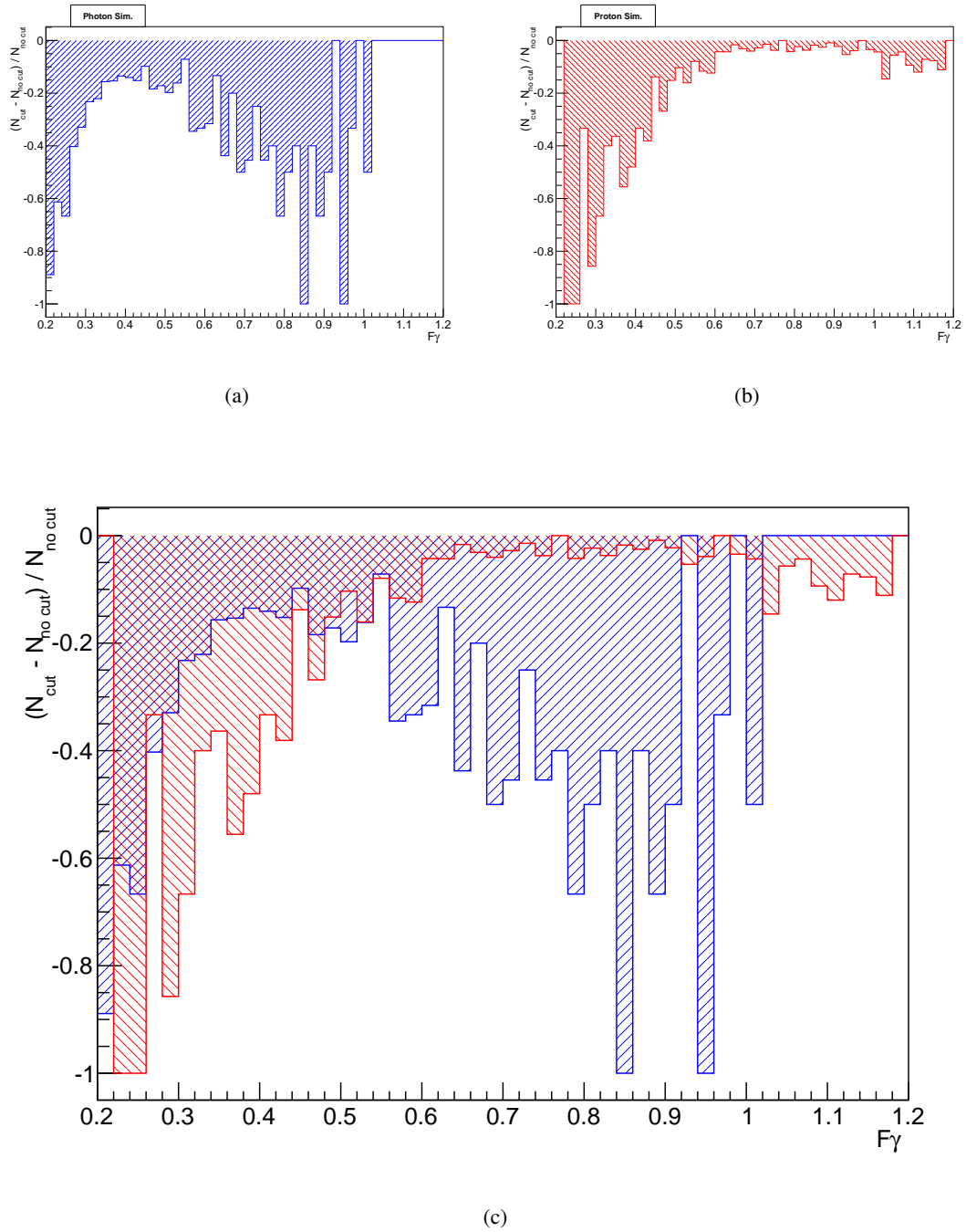


Figure 2.4.3: The bin-wise difference (normalized) of the F_γ distributions with and without a cut on the relative F_γ error at 0.5 for (a) photon events, (b) proton events and (c) the overlay of both. Simulations: IdSimQII04, $18.0 \leq \log_{10}(E [\text{eV}]) < 18.5$.

3 Studies of the Observable S_b

3.1 Definition of S_b

Another observable for the discrimination between primary photons and hadrons in the data taken at the Pierre Auger Observatory is S_b . This observable will be used together with X_{max} in the upcoming Auger papers about diffuse and directional search for UHE photons. Therefore, it shall be analyzed in this thesis with respect to possible systematic uncertainties. S_b has been introduced first in [RG09, RG10] and is defined by a weighted sum over the signal S_i of each triggered SD station in an event:

$$S_b = \sum_i S_i \times \left(\frac{R_i}{R_0} \right)^b, \quad (3.1)$$

where the weight is given by the distance R_i of the i -th station to the shower core divided by a reference distance $R_0 = 1000m$. The geometrical reconstruction of the shower needed for S_b is taken from the FD. Hence, S_b also relies on hybrid data. The exponent b can be adjusted depending on the specific analysis which S_b is applied to in order to optimize the sensitivity of S_b and is usually chosen to be $b = 3$ [KD13] or $b = 4$ [SM13]. In the studies presented in the context of this thesis, b has been chosen to be $b = 4$ because this value maximizes the separation power of S_b between photon and proton events as stated in [SM13]. The limiting distance from the shower core up to which the sum over the stations is calculated is set to 3000 m for $E_{FD} < 4 \text{ EeV}$ and 4000 m for $E_{FD} \geq 4 \text{ EeV}$. The reason why S_b is a useful observable for the task of separating between primary photons and hadrons is, similar to F_γ , its sensitivity to the lateral shower profile. Showers with a steep profile, like photon showers, deposit a large fraction of their signal close to the axis and therefore will have a smaller S_b than showers with a flatter profile since the distance to the axis enters S_b as a weighting factor in the power of four. In Fig. 3.1.1 the separation power of S_b between photons and protons is shown and in Tab. 2 the separation power in terms of the η and ρ_{50} is compiled for 10 energy bins between 1 EeV and 10 EeV. The corresponding plots of the S_b distributions can be found in the appendix (Fig. 5.0.3).

The observable S_b is highly sensitive to the geometry of the SD since for example a denser array would just contribute more terms to the sum of S_b leading to systematically higher value. To obtain a reliable observable out of S_b it is crucial to only compare the S_b value of events with

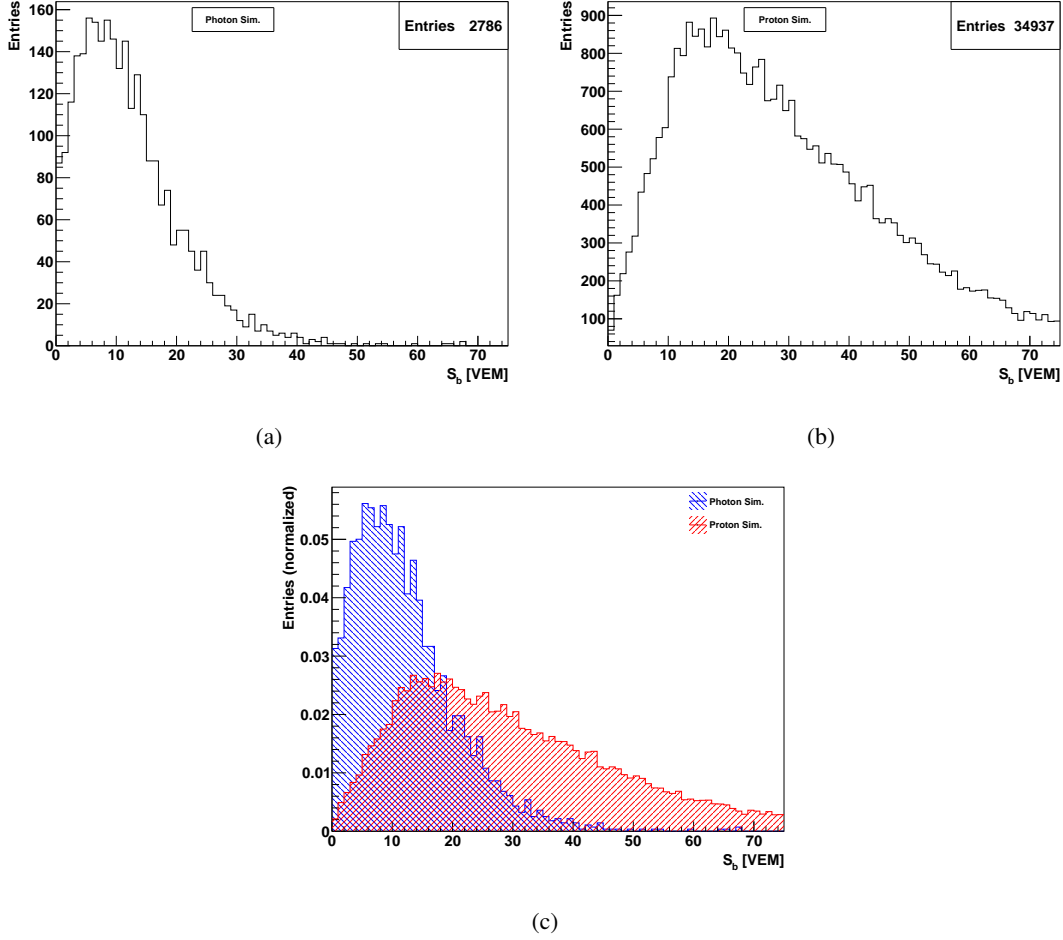


Figure 3.1.1: The distributions of S_b for (a) simulated photon and (b) proton induced air showers. In (c) the overlay of both distributions is shown.

Simulations: TdSimQII04, $18.0 \leq \log_{10}(E [\text{eV}]) < 18.5$.

an equivalent SD geometry. Since the real array is not infinite but has many edges and borders, especially during the construction phase until end of 2008, as well as “black tanks” – tanks which are rejected due to being non-active or malfunctioning – there are some events expected to have a systematically lower S_b because part of the signal is missing. In order to reject such events, there is also a condition on S_b to have at least 4 active stations on the the surrounding hexagon of the hottest station of the SD event – the station with the largest signal –, called the “first crown” (TankOnCrown-Cut). The preselection cuts are the same as applied on F_γ (see Sec. 2.2.5)).

Energy Bin	η	ρ_{50}
$18.0 \leq \log_{10}(E [\text{eV}]) < 18.1$	1.06	93.30
$18.1 \leq \log_{10}(E [\text{eV}]) < 18.2$	1.12	95.95
$18.2 \leq \log_{10}(E [\text{eV}]) < 18.3$	1.12	97.67
$18.3 \leq \log_{10}(E [\text{eV}]) < 18.4$	1.27	97.67
$18.4 \leq \log_{10}(E [\text{eV}]) < 18.5$	1.28	98.29
$18.5 \leq \log_{10}(E [\text{eV}]) < 18.6$	1.42	99.26
$18.6 \leq \log_{10}(E [\text{eV}]) < 18.7$	1.47	99.64
$18.7 \leq \log_{10}(E [\text{eV}]) < 18.8$	1.46	99.74
$18.8 \leq \log_{10}(E [\text{eV}]) < 18.9$	1.58	99.90
$18.9 \leq \log_{10}(E [\text{eV}]) < 19.0$	1.74	99.89

Table 2: The separation power of S_b in terms of the merit factor η as defined in Eq. (2.7) and the background reduction ρ_{50} at a signal efficiency of 50% for 10 energy bins between 1 EeV and 10 EeV. Simulations: IdSimQII04.

3.2 Impact of Holes in the SD Array on the Analysis with S_b

Unlike F_γ , S_b is sensitive to holes⁵ in the detector array because it is calculated by just summing up the signal of each station rather than fitting the LDF. Hence, a missing station close to the shower axis would lead to a smaller value of S_b than it would have without the hole. This effect can artificially create photon candidates from the hadronic background. Therefore it is necessary to find an efficient way to identify such events which could have an artificially small S_b caused by the array geometry and exclude them from the analysis while at the same time keeping as many well-measured events in the data as possible. To obtain an impression of how many events there are with an improper detector geometry, the time dependent simulations TdSimQII04 have been used. The number of holes for each event has been compiled in a histogram (Fig. 3.2.2) considering showers with a zenith angle up to 60° and holes up to a distance of 3 km from the shower core as well as a time dependent detector configuration.

⁵In this analysis, a "hole" in the SD array is defined as a position where the real detector array lacks a station compared to an ideal, perfectly hexagonal array with a spacing of 1500 m between neighboring stations and no borders. Missing stations, edges of the SD array and black stations are equally treated as holes. The black stations were identified and rejected using the T2Life-files, in which for each station the time periods are stored in which it was not working. Examples for positions considered as holes can be found in the plots of the shower footprints e.g. in Figs. 3.2.4, 3.2.5 and 3.3.2 and in the appendix (Figs. 5.0.4 to 5.0.9).

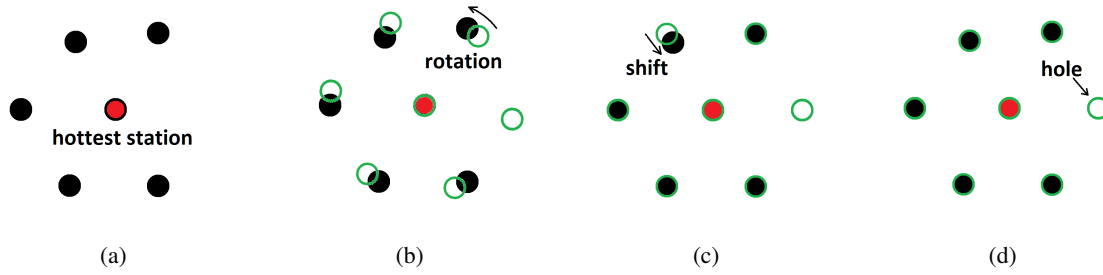


Figure 3.2.1: The procedure to construct an ideal array locally around the hottest station. (a) An example for an (imperfect) array configuration around the hottest station. with only 5 stations on the first crown and a slightly displaced station (the upper left one). (b) An ideal array has been constructed with an, in general arbitrary, angle relative to the existing array such that its central station coincides with the hottest station. (c) The constructed ideal array has been rotated by the average angular displacement of all stations on the first crown. (d) Last, stations of the ideal array which are displaced by < 300 m relative to a station from the real array have been shifted to fit the position of the real array. Now every station in the ideal array which does not coincide with any station of the real array is considered a hole. Note, that in the real application, not just the stations around the hottest stations are fitted but all stations within a square of $14 \text{ km} \times 14 \text{ km}$.

The number of holes has been obtained by constructing an ideal hexagonal array with a spacing of 1500 m in the x - y -plane and shifting the origin to the position of the hottest SD station. Next, the rotation angle has been calculated by averaging over all available stations on the first crown. To make the fit complete, each station of the ideal array has been checked to coincide with any station of the real SD array within a radius of 300 m and if so, shifted to that position. Each station of the artificial ideal array which could not be fitted to a real station is considered one hole in the real detector array. For an illustration of the fitting procedure see Fig. 3.2.1. This way not only black tanks are counted as holes but also non-existing stations e.g. outside the detector plane. This procedure to derive the number of holes in a certain radius around the shower core is not influenced by twin- and triplet-stations⁶ or test stations build in between the hexagonal grid. Such stations are simply ignored by this procedure since the fit algorithm just "tests whether there is any station where one should be".

Without a cut on the SD geometry, the fraction of events with at least one hole is 31.3% as the maximum number of holes go up to 23 as is shown in Fig. 3.2.2. The cases with only one or two

⁶Twin stations and triplet stations are additional, independent SD stations which are build very close to each other (spacing in the order of ~ 10 m) to analyze the signal fluctuations in an individual tank where the particle flux is approximately constant.

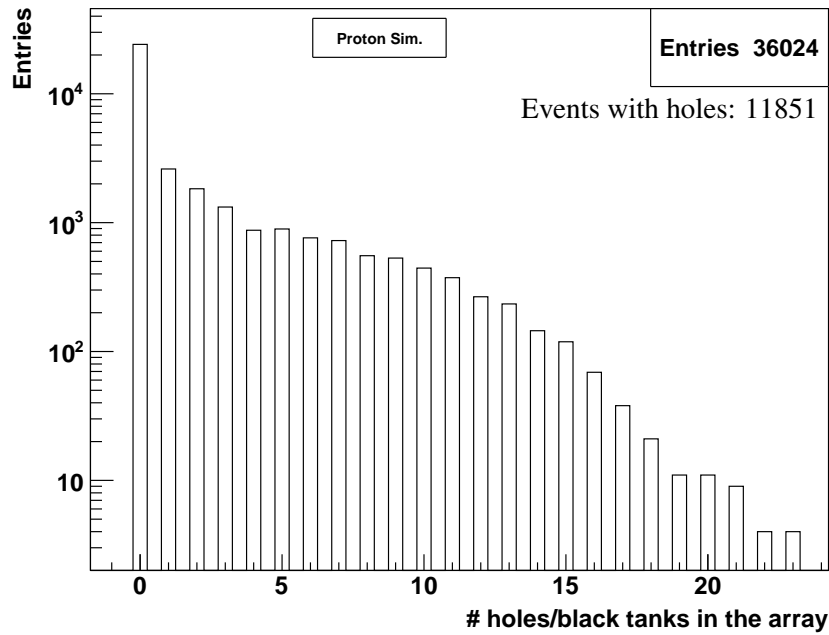


Figure 3.2.2: Number of holes within a 3 km radius from the shower core for each event which passed all preselection and geometry cuts (see Sec. 2.2.5).

Simulations: proton, TdSimQII04, $18.0 \leq \log_{10}(E [\text{eV}]) < 18.5$.

holes can mostly be traced back to single black stations in the array. A larger number of holes is more likely to appear around the outer border of the SD or on the edges of larger areas without stations in between during the construction phase. The TankOnCrown-Cut reduces the number of events with holes by about 9.1% as shown in Fig. 3.2.3.

The fraction of events with holes is reduced to 28.7% as well as the maximum number of holes is reduced to 19. Since events with up to two holes can not be affected by this cut at all, the cut mostly rejects events with a large number of holes. In Fig. 3.2.4 an example for a shower footprint is given where the holes most likely give a bias to S_b despite the application of the cut. One of the holes is very close to the shower axis and within a distance where other stations in this event are triggered. Therefore, if there would have been a working station at this position, it would have most probably given a significant contribution to S_b . Hence, this event is likely to be biased by the detector geometry. Due to its low S_b value, this event could therefore be misjudged as a photon candidate. But since there are still five out of six active stations on the crown, this event still passes the event selection and is used for the analysis. Additional examples of such cases are given in the appendix (Figs. 5.0.4 to 5.0.9). In Fig. 3.2.5 the extreme case with 19 holes from Fig. 3.2.3 is shown which also makes it through the cut and therefore

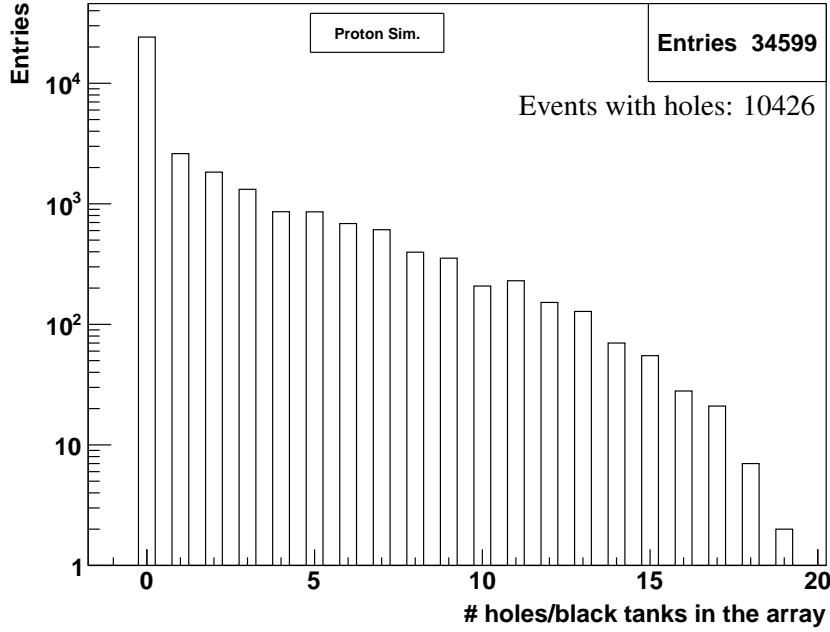


Figure 3.2.3: Number of holes within a 3 km radius from the shower core for each event. Here, only events are considered which pass all preselection and geometry cuts (see Sec. 2.2.5), have $S_b > 0$ and pass the TankOnCrown-Cut.

Simulations: proton, TdSimQII04, $18.0 \leq \log_{10}(E [\text{eV}]) < 18.5$.

could fake a photon candidate as well due to a systematically low S_b value. Although the cut rejects a majority of events which are biased by this effect, there can obviously be still events which are heavily influenced since only four out of six stations on the crown are required to exist and work properly or in the case of very inclined showers, where a large fraction of the potential signal is not necessarily deposited close to the hottest station like the one in Fig. 3.2.5. Such inclined events at the border of the SD array are the reasons for most of the many-holes events in Fig. 3.2.3. To completely avoid this border effect, one would have to place a stricter cut on the SD configuration and take into account only events which are in a safe distance to any border or area with incomplete SD grid for the analysis with S_b .

Now, having an impression of the relative frequency and the qualitative impact of holes on the analysis with S_b , the impact of this effect shall be quantified in terms of the separation power of S_b between primary photons and hadrons. Keeping in mind ρ_{50} as a convenient measure for the separation power for this purpose, the background protons which have a smaller S_b value than the median q_{50} of the photon distribution are considered photon candidates. The number of those photon candidates within a sample of simulated proton events has been calculated for the

distributions with and without holes and compared to each other in Fig. 3.2.6.

As one would expect, the distribution of the events with holes is shifted towards lower S_b values compared to the one without holes. The events with holes have a notable larger relative contribution to the number of photon candidates (19.3%) than the events without holes (8.1%) which make up a total of 11.5% photon candidates in the whole sample. This shows that there is a certain bias introduced to the analysis caused by the holes in the SD array. The result also suggests that there is probably a systematical time dependency on S_b since the geometry of the SD was much more inhomogeneous during the first years of construction than it is today. In large areas of the SD, the detector array was not fully constructed and therefore, the probability for an event to contain holes should have been significantly larger back then. In Figs. 3.2.7 and 3.2.8, the difference in the number of holes and the distributions of S_b between the 10,000 latest (Nov. 20th, 2011 to Dec. 30th, 2013 UTC) and 10,000 earliest (Nov. 1st, 2005 to Jul. 7th, 2008 UTC) events show that this time dependency can actually be observed in time dependent simulations although the difference in the number of holes is just of the order of 10% which lead to $\sim 3\%$ more background candidates in the early array than in the late array.

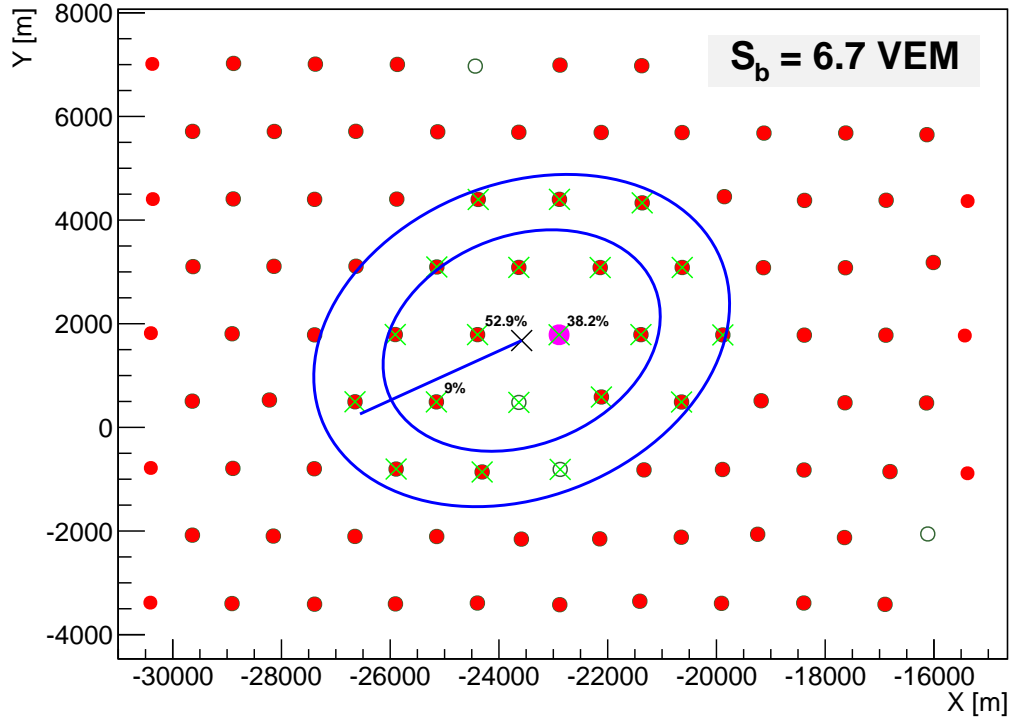


Figure 3.2.4: The configuration of the SD event for an event with two holes from Fig. 3.2.3 which passes the cut on the number of stations on the first crown.

The red dots mark the positions of the existing and active SD tanks. The big dots in magenta mark the position of the hottest station (SD) for each event. The green circles are the tank positions of an ideal array without holes or borders which has been locally constructed around the shower footprint on the ground. The green crosses mark the stations which are inside a 3000 m radius from the shower axis and therefore used for the calculation of S_b in this energy bin ($18.0 \leq \log_{10}(E [\text{eV}]) < 18.5$). For better visualization, the 2000 m and 3000 m radii around the axis are drawn as the blue ellipses and the shower core on ground is marked by the black cross. The blue line which radiates from the shower core on ground is the projection of the shower axis on the x-y-plane up to a distance of 5 km from the core. The percentage numbers nearby the station points give the relative contributions to S_b (shown in the upper right corner) for each station with signal.

Simulations: proton, TdSimQII04; rec. energy [MC energy]: $(2.2 \pm 0.3) \text{ EeV}$ [1.89 EeV]; zenith angle: $41.0^\circ \pm 1.1^\circ$.

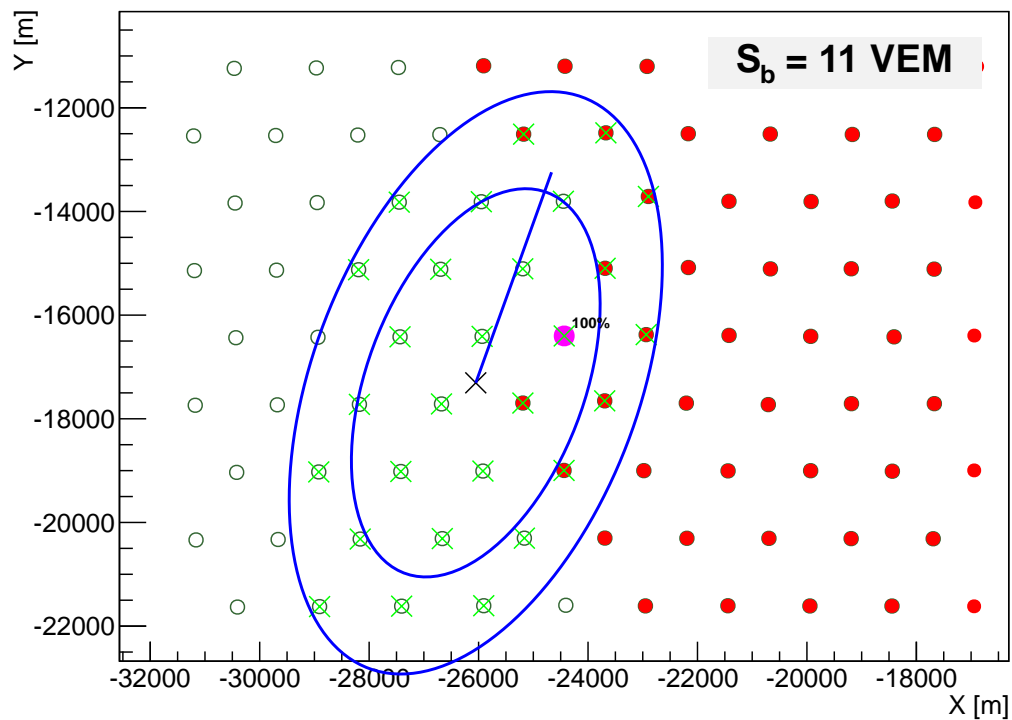


Figure 3.2.5: The configuration of the SD event for the event with 19 holes from Fig. 3.2.3 which passes the cut on the number of stations on the first crown. The different markers and visualization tools used in this picture are explained in Fig. 3.2.4.

Simulations: proton, TdSimQII04; rec. energy [MC energy]: $(1.79 \pm 0.13) \text{ EeV}$ [1.961 EeV]; zenith angle: $59.4^\circ \pm 1.0^\circ$.

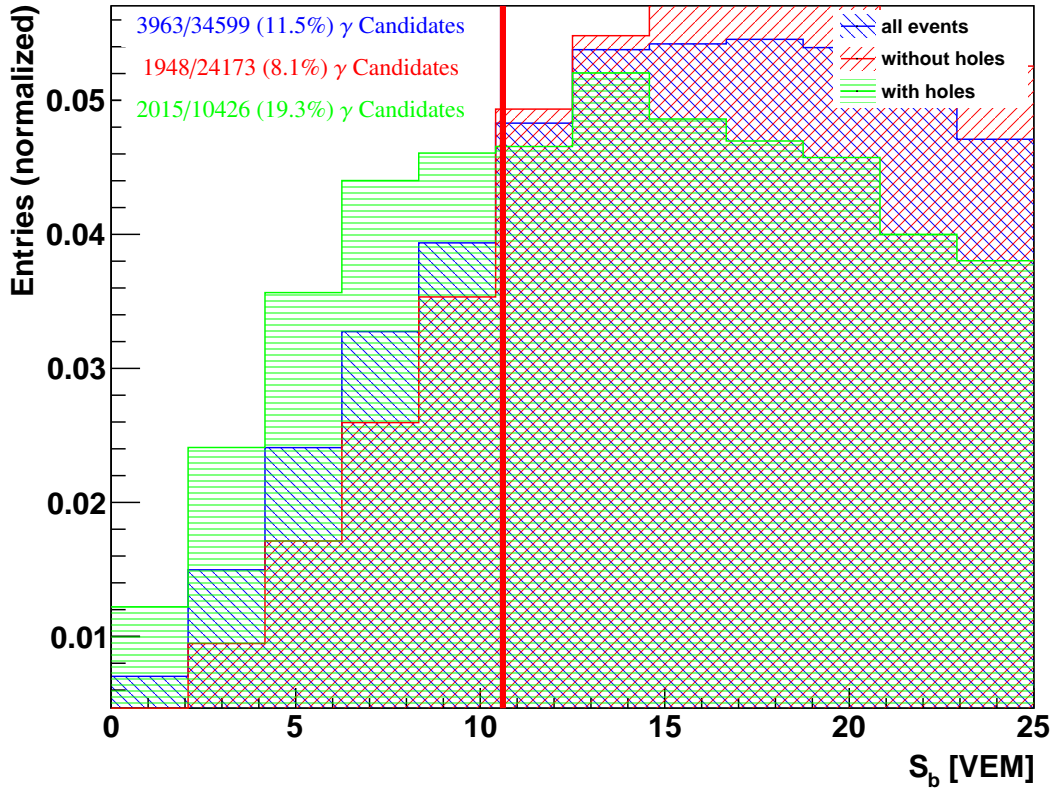
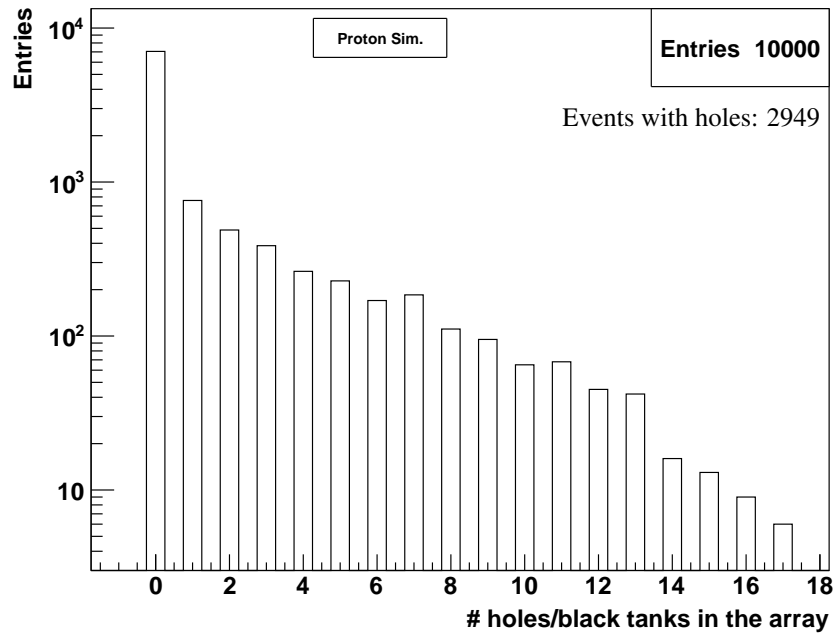
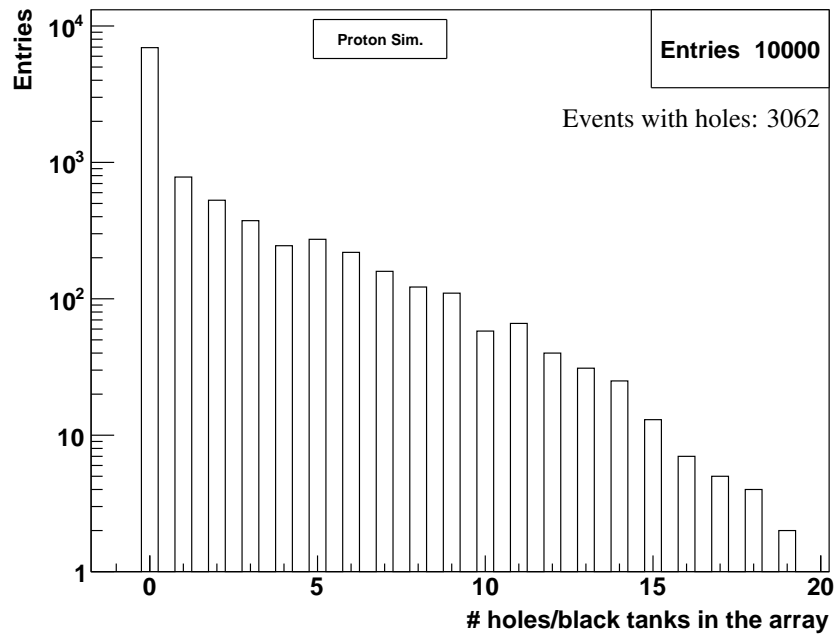


Figure 3.2.6: The left tail of the normalized S_b distribution for simulated proton events is shown comparing the cases where all events (blue), only events without holes (red) and only events with holes (green) are considered. The vertical line marks the 50% quantile $q_{50} = 10.6$ of the S_b distribution for a sample of simulated photon events. The numbers given in the overlay plot are the number of photon candidates, over the total number of events in the distribution. Only events are shown which pass all cuts given in Sec. 2.2.5, have $S_b > 0$ and pass the TankOnCrown-Cut.

Simulations: proton, TdSimQII04; Energy: $18.0 \leq \log_{10}(E [\text{eV}]) < 18.5$.



(a)



(b)

Figure 3.2.7: Number of holes within a 3 km radius from the shower core for each event. Here, only events are considered which pass all preselection and geometry cuts (see Sec. 2.2.5), have $S_b > 0$ and pass the TankOnCrown-Cut. (a) 10,000 latest events. (b) 10,000 earliest.

Simulations: proton, TdSimQII04, $18.0 \leq \log_{10}(E [\text{eV}]) < 18.5$

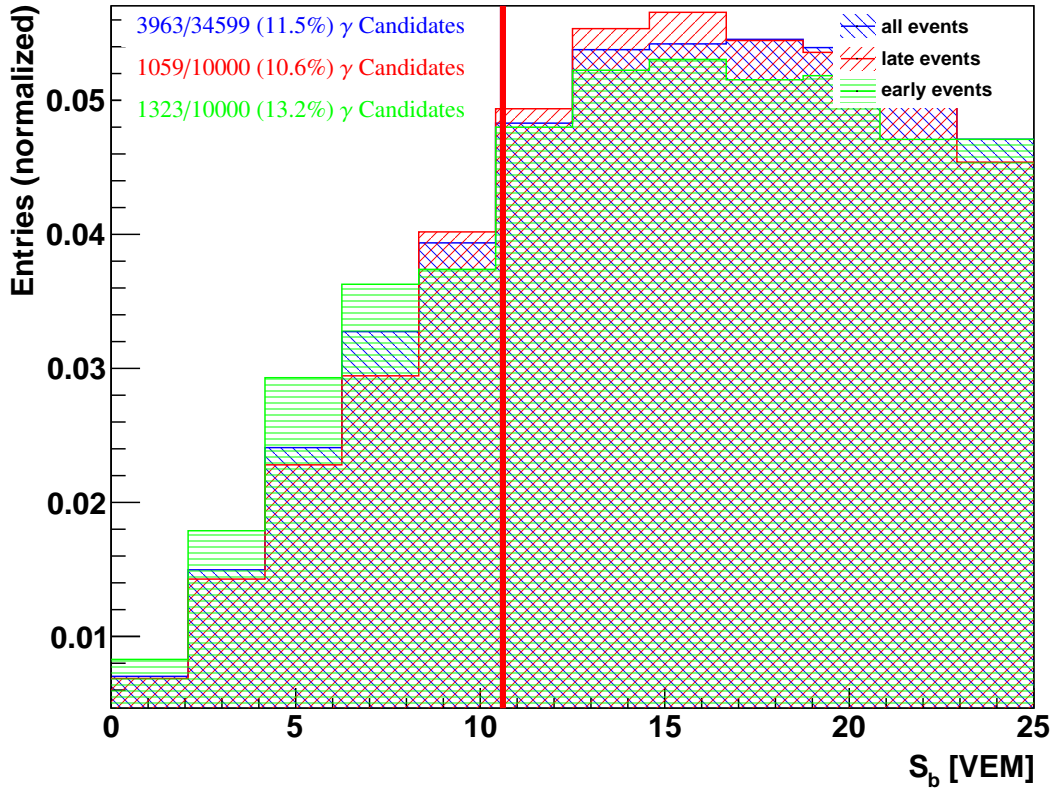


Figure 3.2.8: The left tail of the normalized S_b distribution for simulated proton events is shown comparing the cases where all events (blue), the 10,000 latest events (red) and the 10,000 earliest events (green) are considered. The vertical line marks the 50% quantile $q_{50} = 10.4$ of the S_b distribution for a sample of simulated photon events. The numbers given in the overlay plot are the numbers of photon candidates, over the total number of events in the distribution. Only events are shown which pass all cuts given in Sec. 2.2.5, have $S_b > 0$ and pass the TankOnCrown-Cut.

Simulations: proton, TdSimQII04, $18.0 \leq \log_{10}(E [\text{eV}]) < 18.5$.

3.3 Alternative Definition of the S_b -Cut

In previous studies with S_b [SM11, SM13], another cut has been applied to reject events with many holes. The cut required at least four active and properly working SD stations within a 2000 m radius from the shower axis (TankOn2000-Cut) instead of the first crown. The distribution of holes after application of this cut is shown in Fig.3.3.1 which should be compared to Fig. 3.2.3.

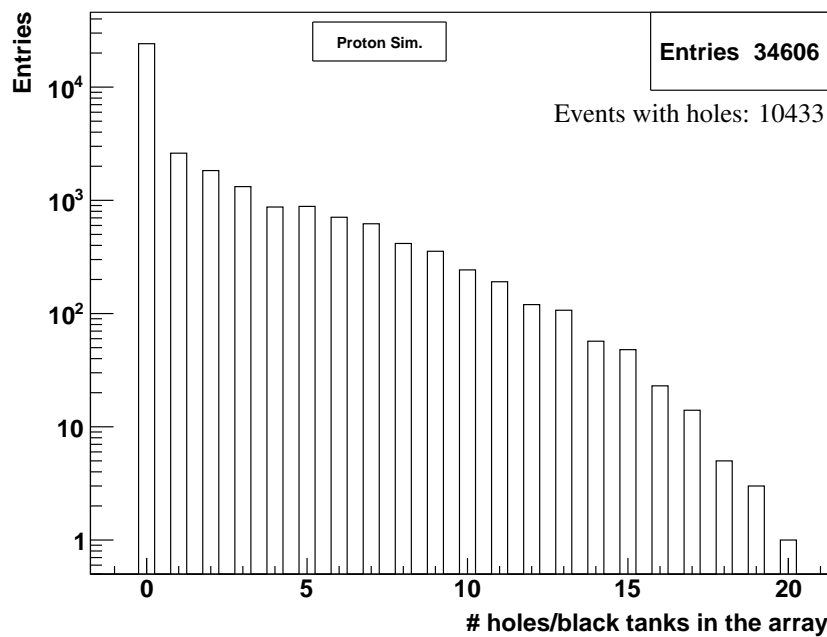


Figure 3.3.1: Number of holes within a 3 km radius from the shower core for each event. Here, only events are considered which pass all preselection and geometry cuts (see Sec. 2.2.5), have $S_b > 0$ and pass the TankOn2000-Cut.

Simulations: proton, TdSimQII04, $18.0 \leq \log_{10}(E [\text{eV}]) < 18.5$.

The TankOn2000-Cut rejects slightly more events with holes than the TankOnCrown-Cut despite the fact that the same number of active stations is required within a larger area. The change of the cut definition did not significantly change the expected number of photon candidates (11.5% vs. 11.0%) as can be seen when comparing Fig. 3.2.6 and Fig. 3.3.3 nor does it change the overall impact of the holes on S_b . That means, that the currently used definition of the cut is not a stricter condition on S_b than the previous one. This behavior can be understood by comparing for example the shower footprints of the events with the most holes for the

TankOnCrown-Cut (Fig. 3.2.5) and the TankOn2000-Cut (Fig. 3.3.2). Both events would have been rejected by the respectively other cut. The problem, both cut definitions have in common is, that the events at the border of the SD can not be identified by either of them. While the TankOn2000-Cut at least requires the border of the array to be within a 2000 km radius from the shower axis, the TankOnCrown-Cut just needs four active stations around the one with the most signal independently of the distance of this station from the shower axis. Another problem of the TankOn2000-Cut is the fact, that for the more inclined showers, the hottest station is not necessarily the one which is closest to the axis since particle flux also strongly depends on the shower age. Hence, it can occur, that there are stations outside the critical 2000 m radius which have a larger contribution to S_b than station which are closer to the axis because the shower was younger (in terms of shower age) and had a higher particle density when it passed those stations. In conclusion, it can be stated, that both the TankOnCrown-Cut as well as the TankOn2000-Cut have some loopholes which prevent events with biased S_b values to be filtered out of the data set leading to an overall bias in the number of expected photon candidates and also to time dependent effects due to the evolution of the SD over the years.

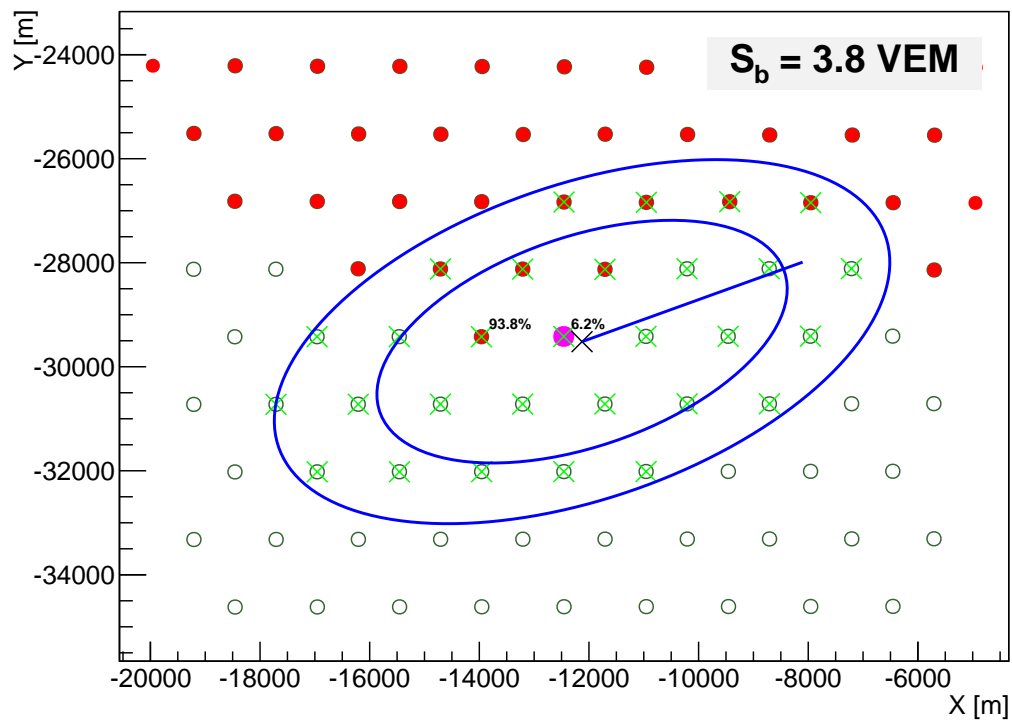


Figure 3.3.2: The configuration of the SD event for the event with 20 holes from Fig. 3.3.1 which passes the TankOn2000-Cut. The different markers and visualization tools used in this picture are explained in Fig. 3.2.4.

Simulations: proton, TdSimQII04; rec. energy [MC energy]: (1.19 ± 0.10) EeV [1.31 EeV]; zenith angle: $59.7^\circ \pm 0.9^\circ$.

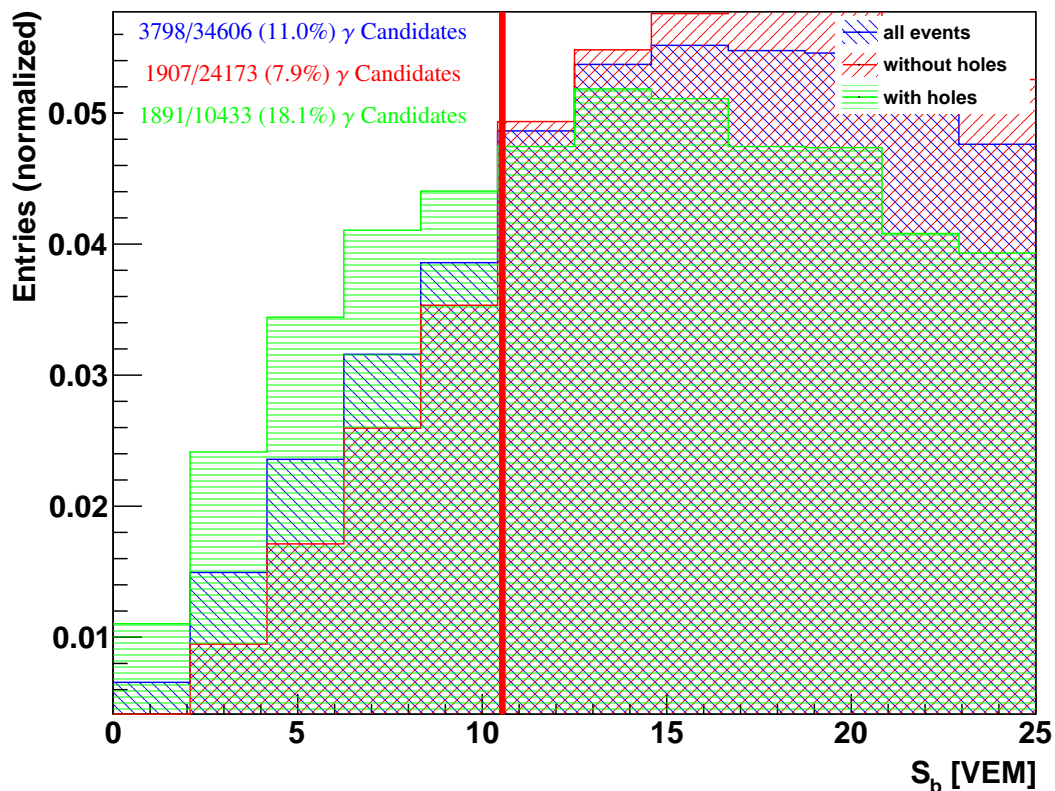


Figure 3.3.3: The left tail of the normalized S_b distribution for simulated proton events is shown comparing the cases where all events (blue), only events without holes (red) and only events with holes (green) are considered. The vertical line marks the 50% quantile $q_{50} = 10.5$ of the S_b distribution for a sample of simulated photon events. The numbers given in the overlay plot are the number of photon candidates, over the total number of events in the distribution. Only events are shown which pass all cuts given in Sec. 2.2.5, have $S_b > 0$ and pass the TankOn2000-Cut.

Simulations: proton, TdSimQII04, $18.0 \leq \log_{10}(E [\text{eV}]) < 18.5$.

4 Conclusions

4.1 Summary of Results

In order to discriminate photon primaries among the cosmic ray flux at ultra high energies, one needs a set of complementary observables to obtain a high separation power. Due to large event-to-event fluctuations of each observable, only statistical statements can be made about the abundance of photons. This is done by comparing the observed air showers to simulations without photons and checking for significant deviations in the region where one would expect photon candidates. The Pierre Auger Observatory offers the possibility of hybrid measurements – simultaneous measurements with the SD and the FD. The kind of data taken from both detector types complements each other quite well in terms of photon-hadron discrimination. A useful FD observable for this task is X_{max} , which has been studied well in the past. In this thesis two observables, F_γ and S_b , which are related to the SD measurements were closely investigated relating their systematic uncertainties, changing of the detector with time and possible limits of applicability. Further on, a possible quality cut on F_γ has been analyzed and an optimum cut-value at $\Delta F_\gamma / F_\gamma < 0.5$ has been proposed. In terms of F_γ , the procedure to derive the observable, which was introduced in [NM15] has been revised in order to increase the statistics. It has been ascertained, that the SD stations with a saturated HG can be included in the analysis by recovering the signal from the LG. Next, the systematic impact of a cut on the distance of SD stations to the shower has been analyzed. It turned out that there is no significant bias introduced by such a cut. The final value of this cut has to be chosen reasonable to avoid long computation times. The revised version of the energy calibration formula of the SD published at the ICRC 2015 as well the new trigger algorithms MoPS and ToTd have been tested in the context of the F_γ analysis and proven also to not introduce any bias. It turned out, that the error on F_γ is reduced when using the new triggers. Next, F_γ has been tested for its systematical uncertainties. It was found, that the small bias introduced to F_γ at events with few triggered stations stays far within the event-to-event fluctuations which means that F_γ is very robust under restriction of the number of SD stations used for the LDF fit and has consistent values even at events with a single triggered SD station. The parametrization of the exponent β used for the constrained LDF fit which was used here, has been derived from simulations between 10^{18} eV and 10^{19} eV. Here, the parametrization has been checked for its validity beyond this energy range. At $10^{19.5}$ eV, the fit becomes worse about 1% compared to $10^{19.0}$ eV.

In terms of S_b , the impact of borders and holes in the SD array has been checked in total as well as at an event-to-event basis. It has turned out that a critical amount of holes near the shower axis can cause an artificially low S_b value which imitates photon candidates. Due to the frequent occurrence of holes and missing tanks throughout the history of the SD, this effect is not negligible. The cuts which are currently applied and have been applied on S_b in the past are not enough to get rid of this effect.

4.2 Prospects

Since the systematic of F_γ has now been studied and understood in detail, it can be combined with X_{max} in a multivariate analysis and applied on data. If the new trigger systems MoPS and ToTd shall be included in the analysis, the new triggering probability should then be taken into account in the LDF fit. A further step which can be taken in future to improve the analysis with F_γ is the extension of the photon-optimized LDF fit to higher energies depending on the energy range covered by the data. To improve the analysis with S_b , a future prospect would be the revision of the local SD geometry cut to reduce the influence of bad measured S_b values due to an incomplete detector configuration in the vicinity of the shower core. One possibility for such a cut could be the requirement of the shower core to be inside a properly working triangle of SD stations. Further investigations in terms of cut efficiency might suggest the inclusion of the lateral trigger probability (LTP) function [SM10] and the arrival direction in the cut, to require only stations to exist, from which a contribution to S_b can be expected. In addition to this, a way to estimate the statistical uncertainty on the individual S_b value should be derived to be able to make a statement about the significance of the S_b value for each photon candidate. If this is done, one could also think of a quality cut on S_b similar to the one applied on F_γ .

Although S_b and F_γ use similar kind of information from an air shower, the lateral profile, one observable can be used to crosscheck the results of the other one. This approach will be followed in the upcoming Auger Collaboration paper about diffuse search for UHE photons using hybrid data from the Pierre Auger Observatory. S_b will be used in combination with X_{max} as the prime observables. If there are photon candidates in the data, their significance of being candidates will be crosschecked with F_γ and its corresponding statistical uncertainty. A compilation of the observable F_γ is going to be published in a short author list paper in the near future independently of the analysis of diffuse UHE photon search. The basic procedure behind the F_γ analysis, the

introduction of a constrained LDF fit, is not only a useful tool for the identification of photons, but could in principle also be of use in the task of identifying the mass composition of UHECR. The investigation of an F_γ -like observable for this task could also be a topic for future analysis.

5 Appendix

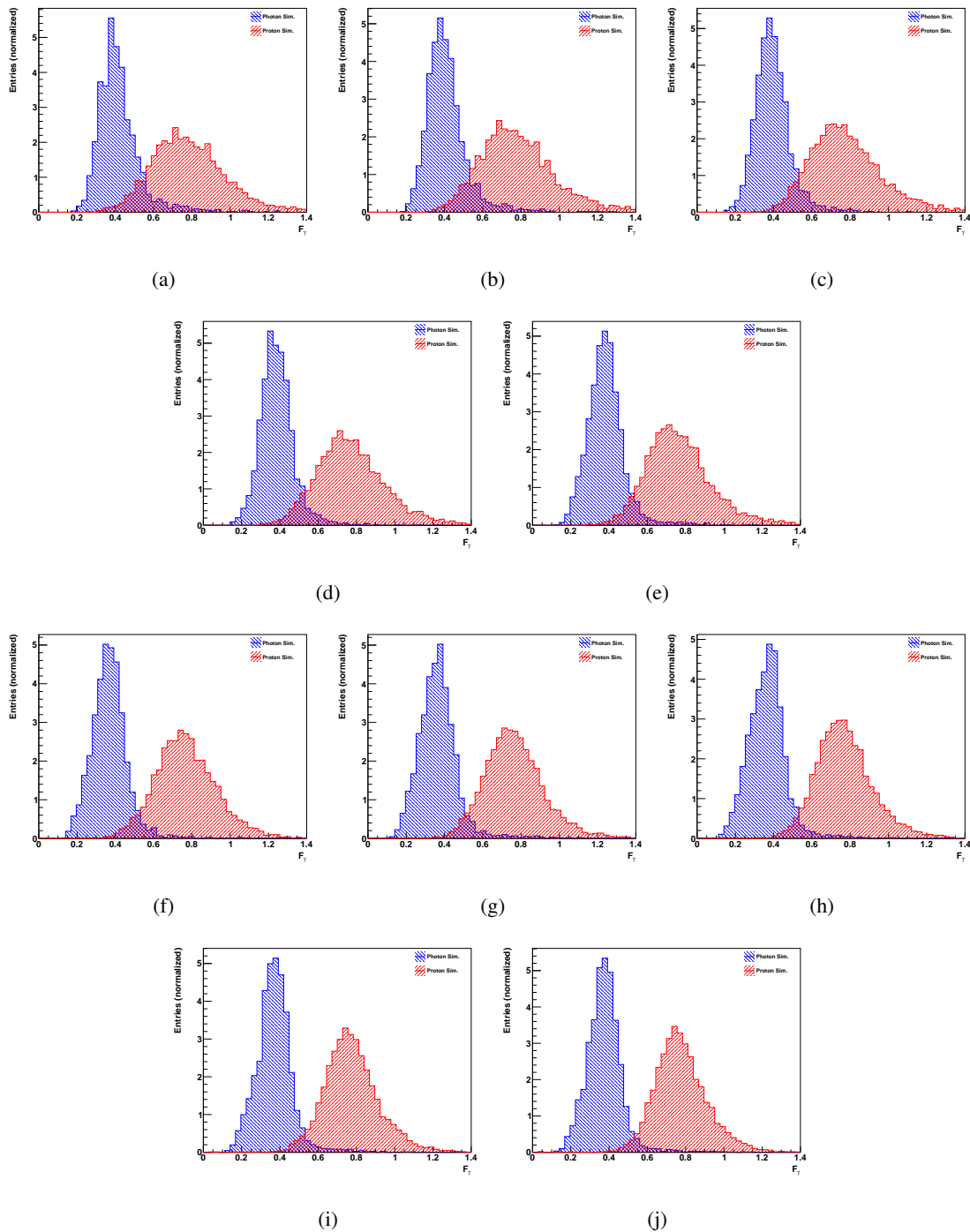


Figure 5.0.1: The overlays of the F_γ distributions of simulated photon and proton events in the energy bins

- (a) $18.0 \leq \log_{10}(E [\text{eV}]) < 18.1$, (b) $18.1 \leq \log_{10}(E [\text{eV}]) < 18.2$,
(c) $18.2 \leq \log_{10}(E [\text{eV}]) < 18.3$, (d) $18.3 \leq \log_{10}(E [\text{eV}]) < 18.4$,
(e) $18.4 \leq \log_{10}(E [\text{eV}]) < 18.5$, (f) $18.5 \leq \log_{10}(E [\text{eV}]) < 18.6$,
(g) $18.6 \leq \log_{10}(E [\text{eV}]) < 18.7$, (h) $18.7 \leq \log_{10}(E [\text{eV}]) < 18.8$,
(i) $18.8 \leq \log_{10}(E [\text{eV}]) < 18.9$, (j) $18.9 \leq \log_{10}(E [\text{eV}]) < 19.0$.
Simulations: IdSimQII04.

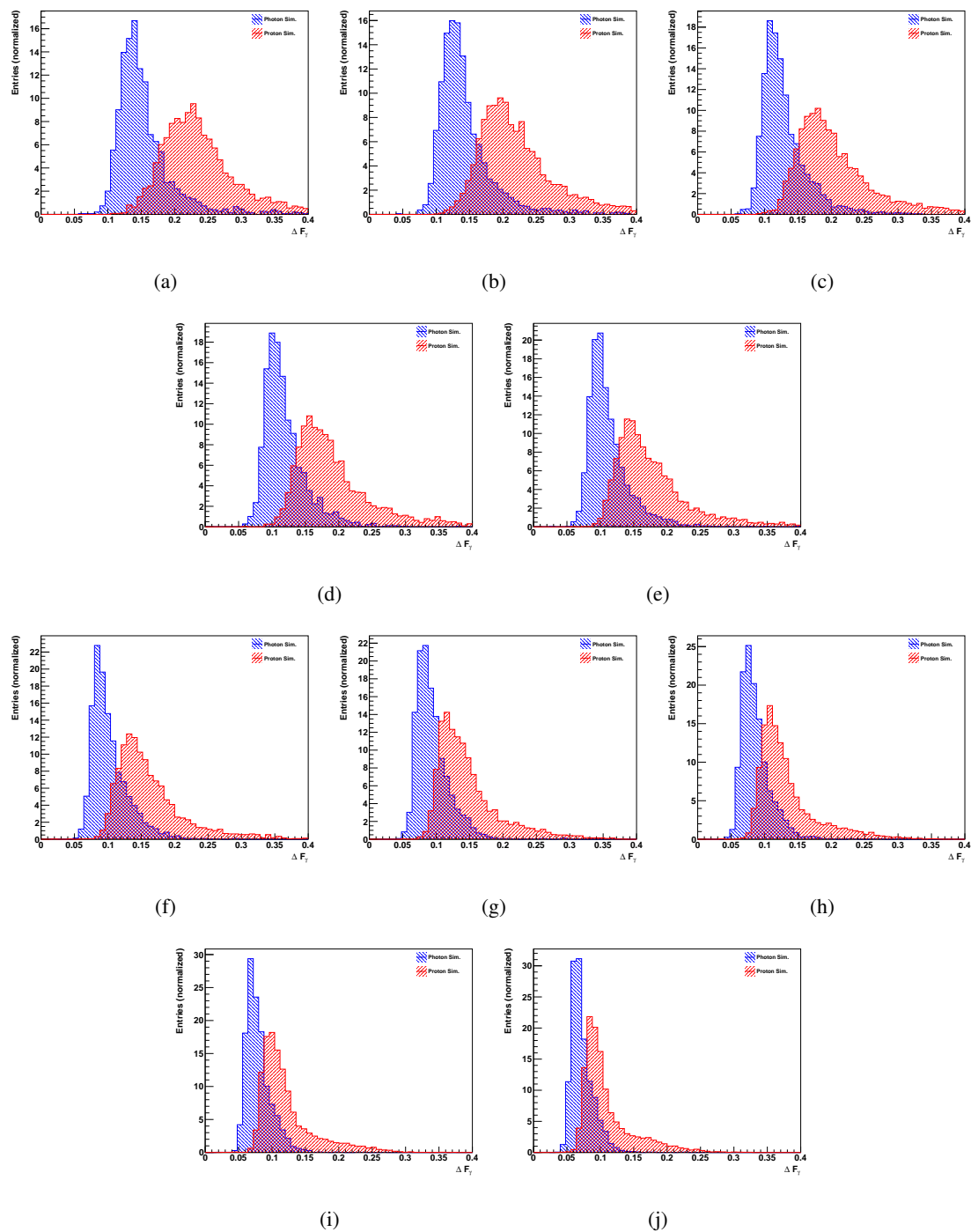


Figure 5.0.2: The overlays of the F_γ error distributions of simulated photon and proton events in the energy bins

- (a) $18.0 \leq \log_{10}(E [\text{eV}]) < 18.1$, (b) $18.1 \leq \log_{10}(E [\text{eV}]) < 18.2$,
(c) $18.2 \leq \log_{10}(E [\text{eV}]) < 18.3$, (d) $18.3 \leq \log_{10}(E [\text{eV}]) < 18.4$,
(e) $18.4 \leq \log_{10}(E [\text{eV}]) < 18.5$, (f) $18.5 \leq \log_{10}(E [\text{eV}]) < 18.6$,
(g) $18.6 \leq \log_{10}(E [\text{eV}]) < 18.7$, (h) $18.7 \leq \log_{10}(E [\text{eV}]) < 18.8$,
(i) $18.8 \leq \log_{10}(E [\text{eV}]) < 18.9$, (j) $18.9 \leq \log_{10}(E [\text{eV}]) < 19.0$.

Simulations: IdSimQII04.

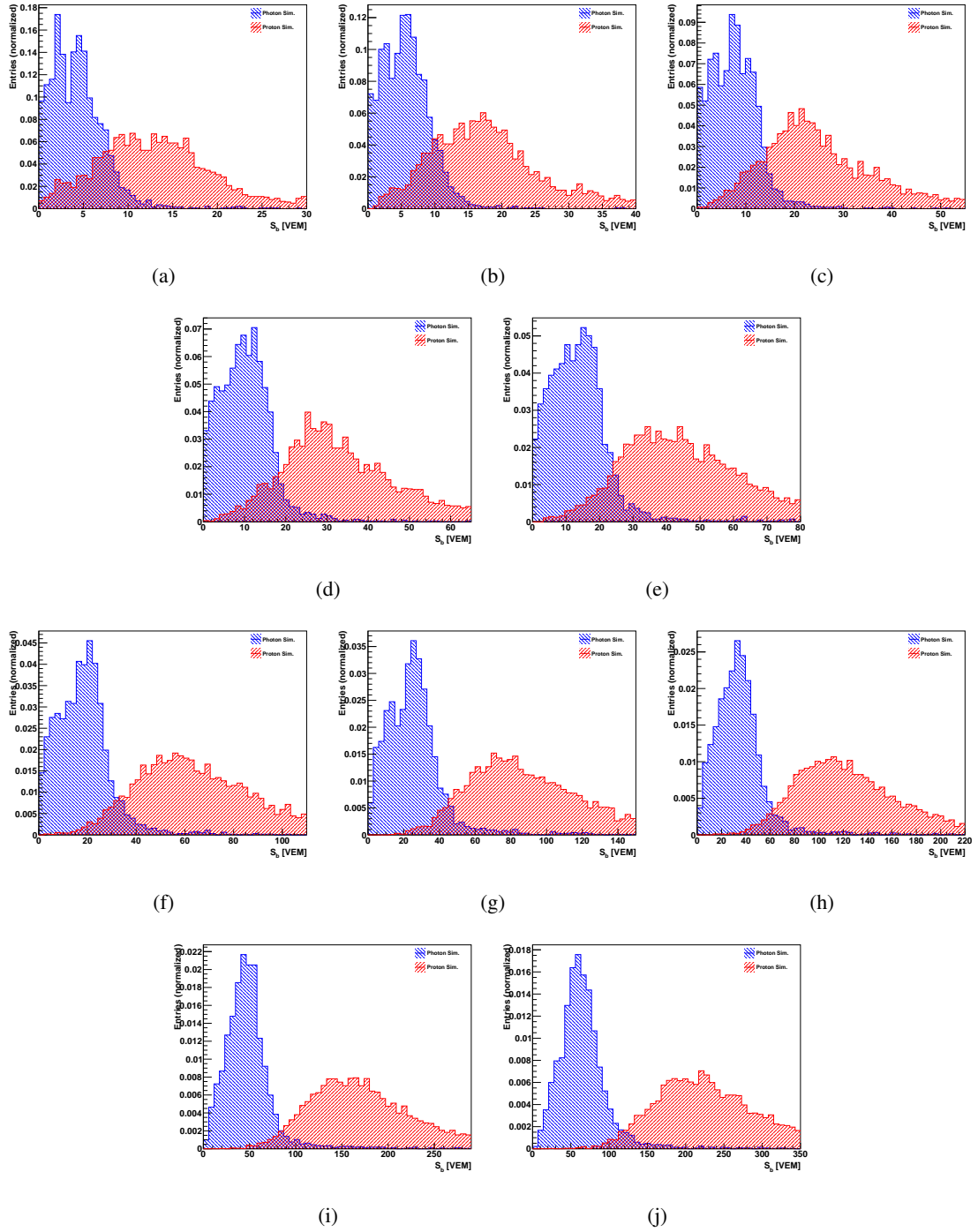


Figure 5.0.3: The overlays of the S_b distributions of simulated photon and proton events in the energy bins

- (a) $18.0 \leq \log_{10}(E [\text{eV}]) < 18.1$, (b) $18.1 \leq \log_{10}(E [\text{eV}]) < 18.2$,
(c) $18.2 \leq \log_{10}(E [\text{eV}]) < 18.3$, (d) $18.3 \leq \log_{10}(E [\text{eV}]) < 18.4$,
(e) $18.4 \leq \log_{10}(E [\text{eV}]) < 18.5$, (f) $18.5 \leq \log_{10}(E [\text{eV}]) < 18.6$,
(g) $18.6 \leq \log_{10}(E [\text{eV}]) < 18.7$, (h) $18.7 \leq \log_{10}(E [\text{eV}]) < 18.8$,
(i) $18.8 \leq \log_{10}(E [\text{eV}]) < 18.9$, (j) $18.9 \leq \log_{10}(E [\text{eV}]) < 19.0$.
Simulations: IdSimQII04.

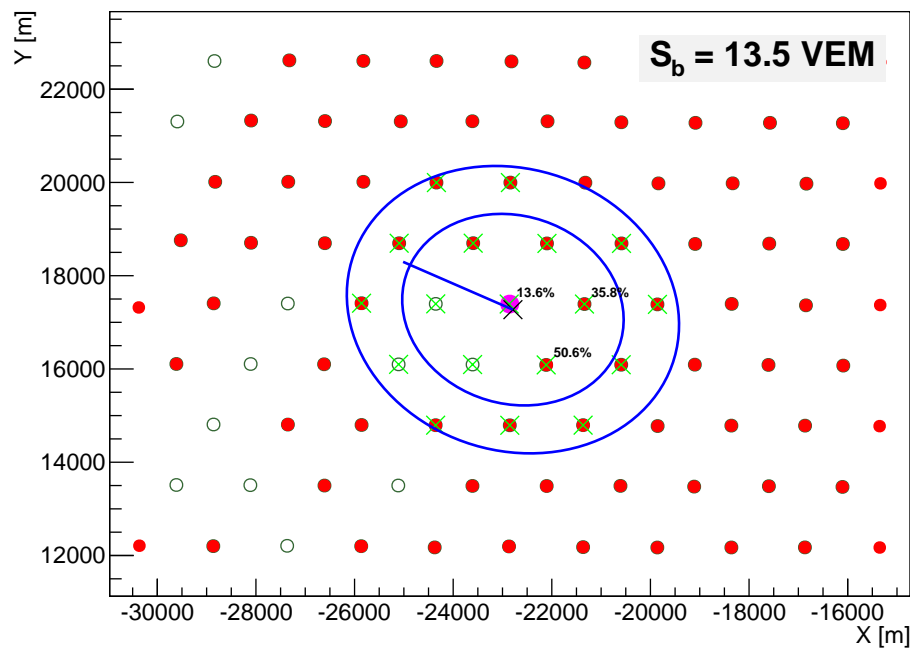


Figure 5.0.4: Simulations: proton, TdSimQII04; rec. energy [MC energy]: rec. energy: [MC energy] (1.38 ± 0.12) EeV [1.546 EeV]; zenith angle: $29.1^\circ \pm 0.3^\circ$.

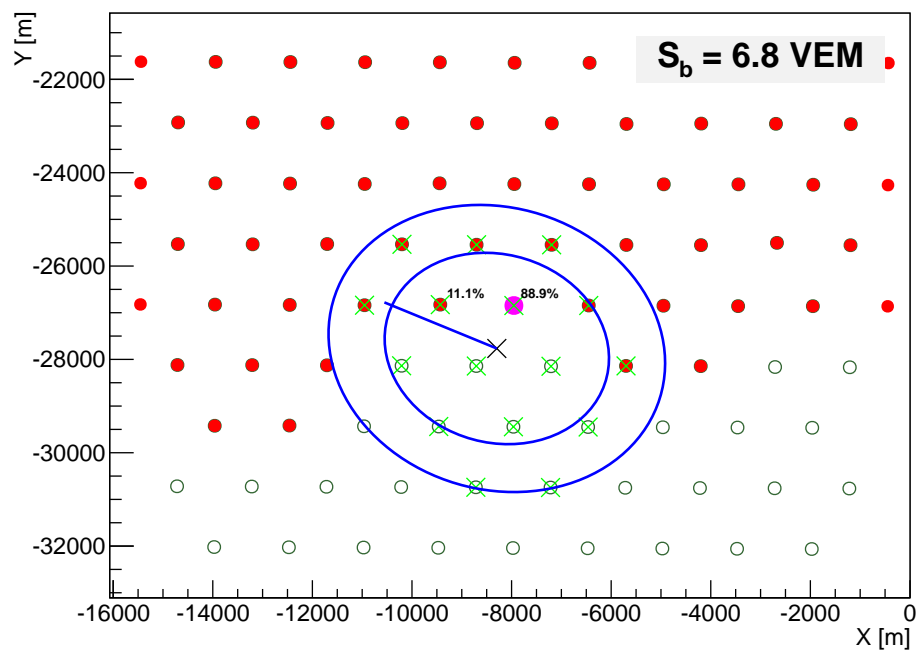


Figure 5.0.5: Simulations: proton, TdSimQII04; rec. energy [MC energy]: rec. energy: [MC energy] (1.77 ± 0.11) EeV [2.065 EeV]; zenith angle: $42.6^\circ \pm 0.3^\circ$.

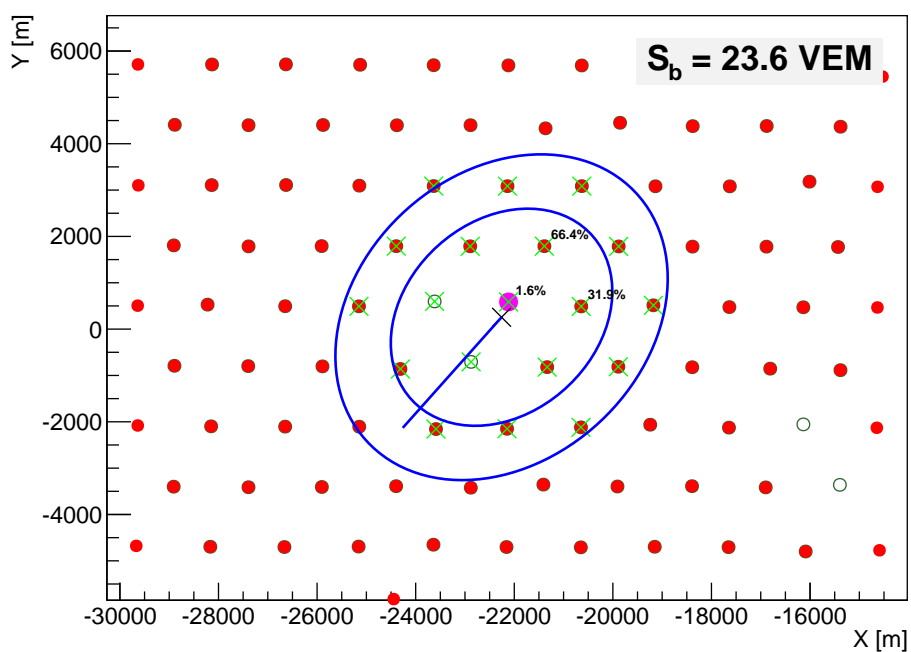


Figure 5.0.6: Simulations: proton, TdSimQII04; rec. energy [MC energy]: rec. energy: [MC energy] (1.81 ± 0.22) EeV [1.869 EeV]; zenith angle: $38.4^\circ \pm 1.1^\circ$.

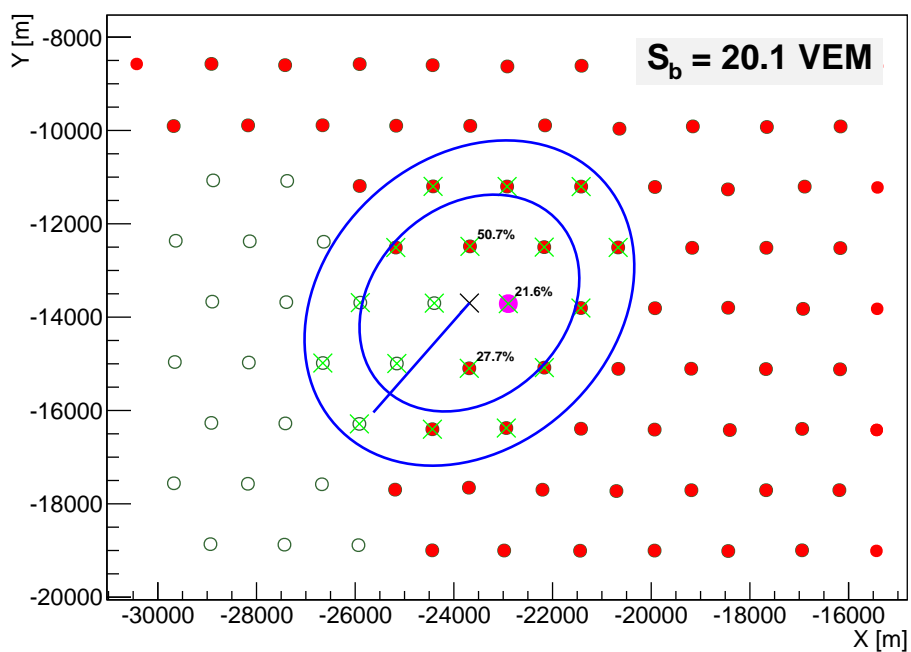


Figure 5.0.7: Simulations: proton, TdSimQII04; rec. energy [MC energy]: rec. energy: [MC energy] (1.78 ± 0.13) EeV [1.869 EeV]; zenith angle: $37.3^\circ \pm 0.5^\circ$.

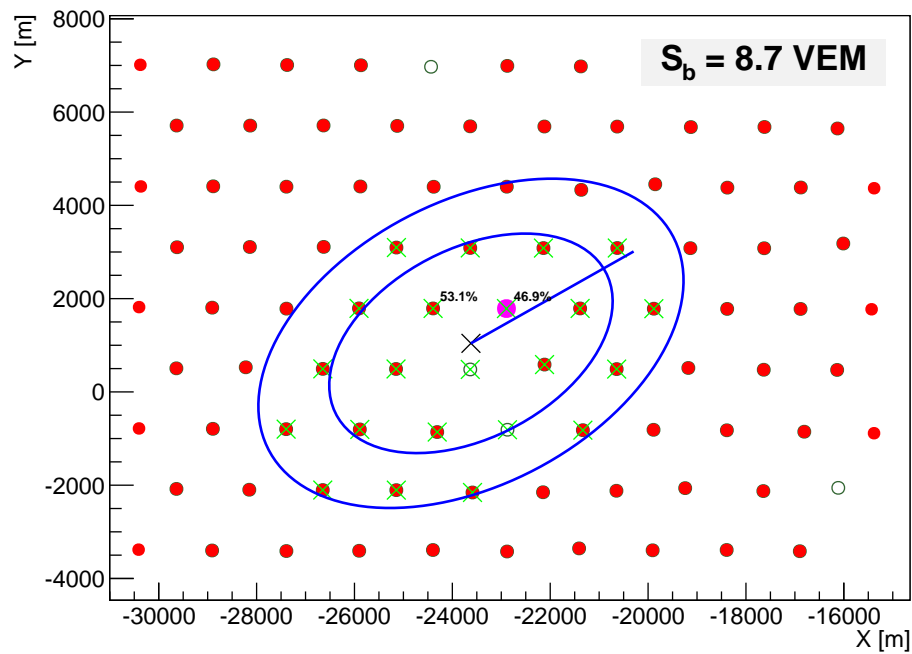


Figure 5.0.8: Simulations: proton, TdSimQII04; rec. energy [MC energy]: rec. energy: [MC energy] (1.87 ± 0.17) EeV [2.029 EeV]; zenith angle: $39.9^\circ \pm 0.9^\circ$.

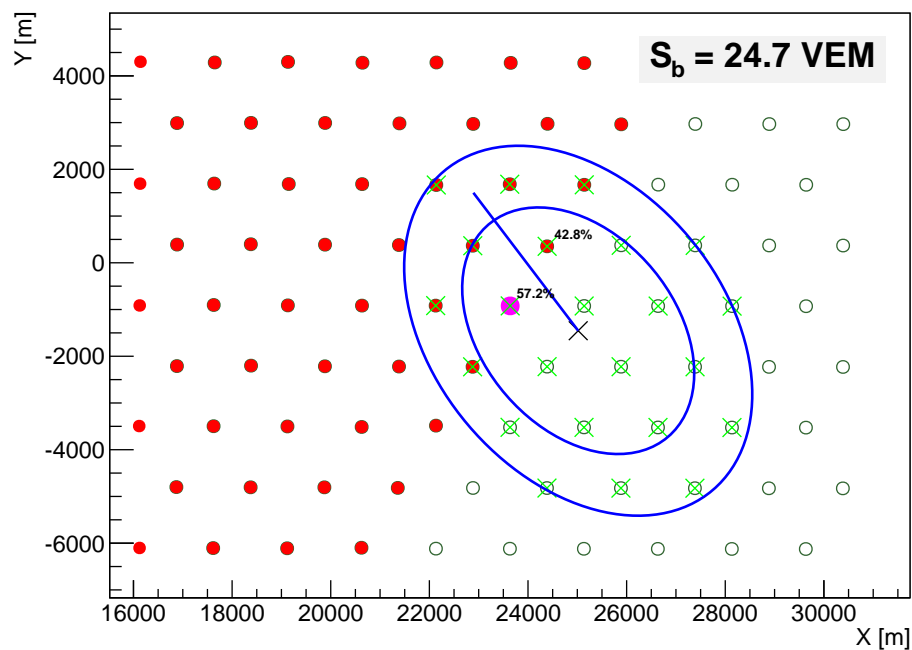


Figure 5.0.9: Simulations: proton, TdSimQII04; rec. energy [MC energy]: rec. energy: [MC energy] (2.24 ± 0.13) EeV [2.645 EeV]; zenith angle: $46.8^\circ \pm 0.2^\circ$.

References

- [AA15a] ALEXANDER AAB ET AL. (PIERRE AUGER COLLABORATION), *The Pierre Auger Cosmic Ray Observatory*, Nuclear Instruments and Methods in Physics Research A **798** (2015) 172-213.
- [AA15b] ALEXANDER AAB ET AL. (PIERRE AUGER COLLABORATION), *The Pierre Auger Observatory Upgrade "Auger Prime"*, arXiv:1604.03637v1, 2015.
- [AJ10a] J. ABRAHAM ET AL. FOR THE PIERRE AUGER COLLABORATION, *Trigger and Aperture of the surface detector array of the Pierre Auger Observatory*, Nuclear Instruments and Methods in Physics Research A **613** (2010), pp. 29-39.
- [AJ10b] J. ABRAHAM ET AL. FOR THE PIERRE AUGER COLLABORATION, *The Fluorescence Detector of the Pierre Auger Observatory*, Nuclear Instruments and Methods in Physics Research A **620** (2010), pp. 227-251.
- [AI08] I. ALLEKOTTE ET AL. FOR THE PIERRE AUGER COLLABORATION, *The Surface Detector System of the Pierre Auger Observatories*, Nuclear Instruments and Methods in Physics Research A **586** (2008), pp. 409-420.
- [AJ08] J. ALLEN ET AL., *The Pierre Auger Observatory offline software*, Journal of Physics:Conference Series, Volume **119**, Part 3.
- [AM02] M. AMBROSIO ET AL. *The camera of the Pierre Auger Observatory Fluorescence Detector*, Nuclear Instruments and Methods in Physics Research A **478** (2002), pp. 125-129.
- [AI15] I. ANTICHEVA ET AL., *ROOT - A C++ Framework for Petabyte Data Storage, Statistical Analysis and Visualization*, Computer Physics Communications Volume **180**, Issue 12, December 2009.
- [AS07] S. ARGIRÒ ET AL., *The Offline Software Framework of the Pierre Auger Observatory*, Nuclear Instruments and Methods in Physics Research A **580** (2007) pp. 1485-1496.
- [AM12] M. AVE FOR THE AIRFLY COLLABORATION, *Precise measurement of the absolute fluorescence yield of the 337 nm band in atmospheric gases*, Astroparticle Physics Vol. **42** (2012), pp. 90-102.

- [AM07] M. AVE FOR THE AIRFLY COLLABORATION, *Measurement of the pressure dependence of air fluorescence emission induced by electrons*, *Astroparticle Physics*, Volume **28**, Issue 1 (2007), pp. 41-57.
- [BP00] PIJUSHPANI BHATTACHARJEE AND GÜNTER SIGL, *Origin and Propagation of Extremely High Energy Cosmic Rays*, *Physics Reports*, **327**, (2000), pp 109-247.
- [BV08] VENESSA CIRKEL-BARTELT, *History of Astroparticle Physics and its Components*, *Living Reviews in Relativity*, **11**, 2 (2008).
- [BJ12] J. BERINGER FOR THE PARTICLE DATA GROUP, *Review of Particle Physics*, *Physical Review D* **86** (2012), p. 010001, and the 2013 partial update for the 2014 edition.
- [BC15] C. BLEVE ET AL. FOR THE PIERRE AUGER COLLABORATION, *Update of the neutrino and photon limits from the Pierre Auger Observatory*, *Proceedings of the 34th International Cosmic Ray Conference (ICRC 2015)*, The Hague, The Netherlands, 2015.
- [CC34] C. CLOPPER AND E. S. PEARSON, *The use of confidence or fiducial limits illustrated in the case of the binomial*, *Biometrika* **26**, pp. 404-413, 1934.
- [CJ06] Photo Credit and Copyright: Jean-Charles Cuillandre (CFHT) and Giovanni Anselmi (Coelum Astronomia), *Hawaiian Starlight*, 2006.
- [FA05] A. FERRARI ET AL., *A multi-particle transport code*, CERN-2005-010, CERN, Geneva, 2005.
- [GT77] T.K. GAISSER AND A.M. HILLAS, *Reliability of the Method of Constant Intensity Cuts for Reconstructing the Average Development of Vertical Showers*. *Proceedings of the 15th International Cosmic Ray Conference (ICRC 1977)*, Plavdiv, Bulgaria, 1977.
- [GP10] P.K.F. GRIEDER, *Extensive Air Showers*, Springer-Verlag Berlin, Heidelberg (2010).
- [GC96] C. GRUPEN, *Particle Detectors*, Cambridge University Press, Cambridge (1996).
- [GC05] C. GRUPEN, *Astroparticle Physics*, Springer-Verlag Berlin, Heidelberg, (2005).
- [HF94] F. HALZEN ET AL., *The highest energy cosmic ray*, *Astroparticle Physics* **3** (1995), pp 151-156.

- [HF98] F. HALZEN, *Lectures on Neutrino Astronomy: Theory and Experiment*, arXiv:astro-ph/9810368v1, 1998.
- [KK58] K. KAMATA AND J. NISHIMURA, *The lateral and the Angular Structure Functions of Electron Showers*, Progress of Theoretical Physics Supplements **6** (1958), pp. 93-155.
- [KD01] D. KAZANAS AND A. NICOLAIDIS, *Cosmic Ray "Knee": A Herald of New Physics?*, Proceedings of the 27th International Cosmic Ray Conference (ICRC 2001), Hamburg, Germany, 2001.
- [KB04] B. G. KEILHAUER, *Investigation of Atmospheric Effects on the Development of Extensive Air Showers and their Detection with the Pierre Auger Observatory*, Ph.D. thesis, University of Karlsruhe (TH) and Forschungszentrum Karlsruhe, Germany, 2004.
- [KK16] K. KOTERA AND J. SILK, *Ultrahigh-Energy Cosmic Rays and Black Hole Mergers*, The Astrophysical Journal Letters, Volume **823**, Number 2.
- [KJ80] J. KRAUS, *A Strange Radiation from Above* Cosmic Search: Issue **5**, Vol. 2, No. 1, Winter 1980.
- [KD07] D. KUEMPEL ET AL. *Geometry reconstruction of fluorescence detectors revisited*, Proceedings of the 30th International Cosmic Ray Conference (ICRC 2007), Mérida, Mexico, 2007.
- [KD13] D. KUEMPEL FOR THE PIERRE AUGER COLLABORATION, *Directional search for ultra-high energy photons with the Pierre Auger Observatory*, Proceedings of the 33rd International Cosmic Ray Conference (ICRC 2013), Rio de Janeiro, Brazil, 2013.
- [MH11] H. MATHES ET AL. FOR THE PIERRE AUGER COLLABORATION, *The HEAT telescopes of the Pierre Auger Observatory Status and First Data*, Proceedings of the 32nd International Cosmic Ray Conference (ICRC 2011), Beijing, China, 2011.
- [MI98] Photo Credit: ESA/ISO, ISOCAM Team, I. F. Mirabel and O. Laurent (CEA/DSM/DAPNIA), et al., 1998, adopted from apod.nasa.gov/apod/ap981204.html (10th July 2015)
- [MK08] K. MURASE, S. INOUE AND S. NAGATAKI, *Cosmic Rays Above the Second Knee from Cluster of Galaxies and Associated High-Energy Neutrino Emission*, The Astrophysical Journal **689** (2008), L105.

- [NASA] Photo Credit: X-ray (NASA/CXC/M. Karovska et al.); Radio 21-cm image (NRAO/VLA/Schiminovich. et al.), Radio continuum image (NRAO/VLA/J. Condon et al.); Optical (Digitized Sky Survey, U. K. Schmidt Image/STScI), 2002, adopted from apod.nasa.gov/apod/ap020812.html (10th July 2015)
- [NW85] W. R. NELSON ET AL., *The EGS4 Code System*, SLAC-R-265, SLAC, Stanford, USA, 1985.
- [NM15] M. NIECHCIOL, *A New Window to the Universe? Searching for Ultra-High-Energy Photons at the Pierre Auger Observatory*, Ph.D. thesis, University of Siegen, Germany, 2015.
- [NRAO] Photo Credit: image curtesy of NRAO/AUI.
- [OS11] S. OSTAPCHENKO, *Monte Carlo treatment of hadronic interactions in enhanced Pomeron scheme: QGSJET-II model*, Physical Review D **83** (2011), p. 014018.
- [PD03] D. PERKINS, *Particle Astrophysics*, Oxford University Press, 2003.
- [PR11] R. PESCE FOR THE PIERRE AUGER COLLABORATION, *Energy calibration of data recorded with the surface detectors of the Pierre Auger Observatory: an update*, Proceedings of the 32nd International Cosmic Ray Conference (ICRC 2011), Beijing, China, 2011.
- [RM04] M. RISSE ET AL., *Primary Particle Type of the Most Energetic Fly's Eye Air Shower*, Astroparticle Physics **21** (2004), pp. 479-490.
- [RG09] G. ROS ET AL., *A new surface parameter for composition studies at high energies*, Proceedings of the 31th International Cosmic Ray Conference (ICRC 2009), Łódź, Poland, 2009.
- [RG10] G. ROS ET AL., *S_b for photon-hadron discrimination*, internal note GAP-2010-052, 2010.
- [RR15] R. RUFFINI, G. V. VERESHCHAGIN AND S.-S. XUE, *Cosmic absorption of ultra high energy particles*, arXiv:1503.07749v1 [astro-ph.HE].
- [SH01] H. SALAZAR ET AL. FOR THE PIERRE AUGER COLLABORATION, *Surface Detector Calibration for the Auger Observatory*, Proceedings of the 27th International Cosmic Ray Conference (ICRC 2001), Hamburg, Germany, 2001.

-
- [SM10] M. SETTIMO, *Hybrid detection of Ultra High Energy Cosmic Rays with the Pierre Auger Observatory*, Ph.D. thesis, University of Salento and INFN, Italy, 2010.
- [SM11] M. Settimo for the Pierre Auger Collaboration, *An update on a search for ultra-high energy photons using the Pierre Auger Observatory*, Proceedings of the 32nd International Cosmic Ray Conference (ICRC 2011), Beijing, China, 2011.
- [SM13] M. SETTIMO ET AL. FOR THE PIERRE AUGER COLLABORATION, *Search for Ultra High Energy Photons with the Pierre Auger Observatory*, Proceedings of the International Conference on the Structure and the Interaction of the Photon (Photon 2013), Paris, France, 2013.
- [UM08] M. UNGER ET AL., *Reconstruction of Longitudinal Profiles of Ultra-High Energy Cosmic Ray Showers from Fluorescence and Cherenkov Light Measurements*, Nuclear Instruments and Methods in Physics Research A **588** (2008), pp. 433-441.
- [VI15] I. VALIÑO FOR THE PIERRE AUGER COLLABORATION, *The flux of ultra-high energy cosmic rays after ten years of operation of the Pierre Auger Observatory*, Proceedings of the 34th International Cosmic Ray Conference (ICRC 2015), The Hauge, The Netherlands, 2015.
- [VD13] D. VEBERIČ FOR THE PIERRE AUGER COLLABORATION, *Estimation of Signal in Saturated Stations of Pierre Auger Surface Detector*, Proceedings of the 33rd International Cosmic Ray Conference (ICRC 2013), Rio de Janeiro, Brazil.

Erklärung

Hiermit erkläre ich, dass ich die vorliegende Master-Arbeit selbständig verfasst und keine anderen als die angegebenen Quellen und Hilfsmittel benutzt, sowie Zitate und Ergebnisse Anderer kenntlich gemacht habe.

(Ort) (Datum)

(Unterschrift)